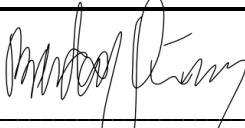




Faculty of Science and Technology

MASTER'S THESIS

| | |
|--------------------------------------------------------------------------------------------------------------------------------------------------------------------|-----------------------------------------------------------------------------------------------------------------------------|
| Study program/ Specialization: Marine and Offshore Technology | Spring semester, 2019 Open / Restricted access |
| Writer: Brendan Quinn 243917 |  _____ (Writer's signature) |
| Faculty supervisor: Dr. Charlotte Obhrai | |
| Thesis title: Validation of the High Order Spectral (HOS) Method for Extreme and Breaking Waves and Coupling of the HOS-Numerical Wave Tank Model with OpenFOAM | |
| Credits (ECTS): 30 | |
| Key words: High Order Spectral Method HOS-NWT Extreme Waves Breaking Waves OpenFOAM | Pages: <u>106</u> + enclosure/Appendix: <u>20</u> total: <u>126</u> Stavanger, 14/06/2019 Date/year |

Abstract:

The objective of this study was to investigate the abilities of the open-source potential flow solver HOS-NWT with regard to extreme wave events and deep-water wave breaking. In addition to this, significant effort was focused on coupling the HOS-NWT software and the computational fluid dynamics software (CFD) OpenFOAM, in an attempt to visualize expected breaking events. Model tests of sea-surfaces with very steep irregular waves were performed in a wave tank at the MARINTEK Ocean Laboratory in Trondheim, Norway. The HOS-NWT model was utilized to recreate a fully non-linear simulation of one of these model tests, which was calibrated at the location of the 12th Wave Gauge in a series of 23 gauges. This calibration point, and the area immediately surrounding it, was the location where the analyses in this study were performed.

The data from the aforementioned model test was used to validate the HOS-NWT model for extreme waves. The results showed that, on average, there was a 14.42% error between the wave heights that were measured experimentally and those that were simulated in HOS-NWT. After investigating as to why such a level of error was sustained, it was found that for increasing levels of individual wave steepness, the accuracy of the HOS-NWT model decayed.

One of the main objectives of this study was to link the HOS-NWT model with an appropriate breaking onset criterion to identify instances of deep-water breaking waves. In total, 8 breaking wave events were known to have been present at different times during experimentation, as a result of high-speed video clips provided by MARINTEK. Four separate criteria were investigated to determine which was most effective in identifying the 8 events captured on video. Ultimately, the Limiting Slope Breaking Criterion [Longuet-Higgins & Smith 1983], which is related to a limiting angle of wave inclination, was selected. This criterion was able to identify the events observed on video at the proper locations and times.

The coupling of HOS-NWT and OpenFOAM proved to be successful; the outputs of HOS-NWT were perfectly replicated within different OpenFOAM simulations. However, the visualization of the breaking processes of the identified breaking waves was unsuccessful. It was determined that the absence of the breaking processes was related to different assumptions of the HOS-NWT software, the employed $k-\omega$ SST Turbulence Model, among other factors.

Future work utilizing an updated version of the HOS-NWT model would likely improve the accuracy of the HOS-NWT model and consequently, the OpenFOAM simulations. Improvements to the HOS-NWT model, which have yet to be publicly released, include appropriate energy dissipation models, which increase the robustness of HOS-NWT in terms of being able to model breaking wave events [Seiffert et al. 2017].

Acknowledgements:

First and foremost I would like to thank my parents for all the love and support that they have shown me throughout my academic career. I have spent two incredible years at the University of Stavanger, and none of it would have been possible without them.

I would also like to express my gratitude to those who supported me throughout the completion of this project. Specifically, I would like to thank my coordinating supervisor Professor Charlotte Obhrai for her feedback, insight, and expertise on the topic of study.

Additionally, I would like to thank Jithin Jose for his guidance and understanding of the models utilized in this research, as well as Gunnar Lian who has provided several sources of data, without which this study would not have been possible.

Table of Contents

| | |
|-------------------------------------------------------------------|------|
| ABSTRACT | II |
| <i>LIST OF FIGURES</i> | V |
| <i>LIST OF TABLES</i> | VII |
| <i>NOMENCLATURE</i> | VIII |
| <i>ABBREVIATIONS</i> | X |
| 2. INTRODUCTION | 1 |
| 3. BACKGROUND & THEORY | 4 |
| 3.1 <i>HOS METHOD</i> | 4 |
| 3.1.1 Boundary Conditions..... | 4 |
| 3.2 <i>EXPERIMENTAL DATA</i> | 10 |
| 3.3 <i>BREAKING ONSET CRITERIA</i> | 12 |
| 3.3.1 Geometric Breaking Criteria..... | 13 |
| 3.3.2 Kinematic Breaking Criteria..... | 15 |
| 3.3.3 Dynamic Breaking Criteria..... | 16 |
| 3.4 <i>OPENFOAM</i> | 18 |
| 3.4.1 Turbulence Models..... | 20 |
| 3.4.1.1 RANS Turbulence Models..... | 20 |
| 3.4.1.1.1 <i>k-ω SST Turbulence Model</i> | 21 |
| 3.4.2 Volume of Fluid Method..... | 24 |
| 3.4.3 Waves2Foam..... | 25 |
| 3.5 <i>GRID2GRID</i> | 27 |
| 4. METHODOLOGY | 29 |
| 4.1 <i>HOS-NWT</i> | 29 |
| 4.1.1 Benchmarking..... | 29 |
| 4.1.2 HOS-NWT Setup..... | 31 |
| 4.2 <i>WAVE BREAKING CRITERIA</i> | 36 |
| 4.3 <i>OPENFOAM</i> | 37 |
| 4.3.1 Computational Mesh..... | 38 |
| 4.3.2 Relaxation Zones..... | 40 |
| 4.3.3 Boundary Conditions..... | 41 |
| 5. RESULTS & DISCUSSION | 43 |
| 5.1 <i>HOS-NWT OUTPUT</i> | 43 |
| 5.2 <i>EXTREME WAVE VALIDATION</i> | 49 |
| 5.3 <i>BREAKING WAVE IDENTIFICATION</i> | 54 |
| 5.3.1 Stokes Limiting Steepness Criterion..... | 55 |
| 5.3.2 Geometric Ratio Criterion..... | 58 |
| 5.3.3 Dynamic/Kinematic Criterion..... | 62 |
| 5.3.4 Limiting Slope Criterion..... | 69 |
| 5.3.4 Breaking Criteria Selection..... | 76 |
| 5.4 <i>OPENFOAM</i> | 76 |
| 5.4.1 Event7..... | 80 |
| 6. CONCLUSION | 85 |
| 7. REFERENCES | 88 |
| 8. APPENDICES | 96 |
| APPENDIX A..... | 96 |
| APPENDIX B..... | 104 |
| APPENDIX C..... | 106 |

List of Figures

| | |
|--------------------------------------------------------------------------------------------------------------------------------------------------------------------------------------------------------------------------------------------------------------------|----|
| FIGURE 1: WAVE GAUGE APPARATUS USED FOR TESTING IN THE MARINTEK OCEAN LABORATORY.. | 11 |
| FIGURE 2: MEASUREMENTS MADE OVER AN ARBITRARY WINDOW IN TIME USING THE SET UP IN FIGURE 1..... | 12 |
| FIGURE 3: SKETCH OF THE VARIATION OF $\alpha_R(\chi_R)$ FOR BOTH INLET AND OUTLET RELAXATION ZONES AS WELL AS A GENERAL OVERVIEW OF HOW A COMMON COMPUTATIONAL DOMAIN IS CONSTRUCTED USING THE WAVES2FOAM TOOLBOX [JACOBSEN ET AL. 2012]..... | 27 |
| FIGURE 4: REGULAR WAVE BENCHMARK RESULT SHOWING VERY CLOSE AGREEMENT BETWEEN THE EXPERIMENTAL DATA AND THE HOS-NWT OUTPUT | 30 |
| FIGURE 5: 2D IRREGULAR WAVE BENCHMARK RESULT SHOWING VERY CLOSE AGREEMENT BETWEEN THE EXPERIMENTAL DATA AND THE HOS-NWT OUTPUT | 31 |
| FIGURE 6: REPRESENTATION OF THE INPUT FILE UTILIZED FRO RUNNING THE HOS-NWT MODEL THROUGHOUT THE COURSE OF THIS STUDY | 32 |
| FIGURE 7: COMPARISON BETWEEN THE FREQUENCY CONTENT OF THE WAVES AT THE WAVE3 GAUGE AND THE JONSWAP SPECTRUM DEFINING THE SEA-STATE | 34 |
| FIGURE 8: 2D SCHEMATIC SHOWING THE ORIENTATION OF THE SINGLE-HINGED WAVE MAKER USED FOR WAVE GENERATION, WHERE THE WATER DEPTH IS 6 M AND THE ROTATION AXIS DISTANCE FROM THE STILL WATER SURFACE IS 4.98 M | 35 |
| FIGURE 9: SINGLE COMPUTATIONAL CELL WITH EACH OF ITS DIMENSIONS LABELED FOR THE X, Y, AND Z DIRECTIONS..... | 39 |
| FIGURE 10: FULL COMPUTATIONAL MESH, HAVING DIMENSIONS OF 15M×0.1M×7M, IN THE X, Y, AND Z DIRECTIONS, CONSTRUCTED USING THE COMPUTATIONAL CELLS ILLUSTRATED IN FIGURE 9..... | 40 |
| FIGURE 11: SURFACE ELEVATIONS FROM THE HOS-NWT MODEL AND THE EXPERIMENTAL MEASUREMENTS AT THE WAVE3 GAUGE/PROJECTED WAVE MAKER LOCATION FOR THE INITIAL 50 SECONDS OF THE SIMULATION..... | 44 |
| FIGURE 12: SURFACE ELEVATIONS FROM THE HOS-NWT MODEL AND THE EXPERIMENTAL MEASUREMENTS BY WAVE GAUGE 12 AT MARINTEK FOR THE INITIAL 50 SECONDS OF THE SIMULATION | 45 |
| FIGURE 13: SURFACE ELEVATIONS FROM THE HOS-NWT MODEL AND THE EXPERIMENTAL MEASUREMENTS AT THE WAVE3 GAUGE/PROJECTED WAVE MAKER LOCATION FOR THE TIME FRAME OF 910-970S SECONDS | 46 |
| FIGURE 14: SURFACE ELEVATIONS FROM THE HOS-NWT MODEL AND THE EXPERIMENTAL MEASUREMENTS AT WAVE GAUGE 12 FOR THE TIME FRAME OF 910-970 SECONDS..... | 47 |
| FIGURE 15: PLOT DEPICTING THE RELATION OF THE INDIVIDUAL WAVE STEEPNESS (AK) OF EXTREME WAVE EVENTS AND THE ERROR CALCULATED BETWEEN THE EXPERIMENTAL DATA AND THE HOS-NWT SIMULATION RESULTS FOR MODEL RUN WITH STEEPNESS $\epsilon_c = 13.46\%$ | 51 |
| FIGURE 16: PLOT DEPICTING THE RELATION OF THE INDIVIDUAL WAVE STEEPNESS (AK) OF EXTREME WAVE EVENTS AND THE ERROR CALCULATED BETWEEN THE EXPERIMENTAL DATA AND THE HOS-NWT SIMULATION RESULTS FOR MODEL RUN WITH STEEPNESS $\epsilon_c = 11.64\%$ | 54 |

| | |
|------------------------------------------------------------------------------------------------------------------------------------------------------------------------------------------------------------------------------------------------------------------------|----|
| FIGURE 17: BREAKING EVENT (EVENT4) WHERE ONSET OCCURRED DURING EXPERIMENTATION AT WAVE GAUGE 8, AND BREAKING CONTINUED PAST WAVE GAUGE 12, THE STOKES LIMITING STEEPNESS CRITERIA RECOGNIZED IT AT WAVE GAUGE 18 | 58 |
| FIGURE 18: BREAKING EVENTS MEASURED BY BOTH THE STOKES LIMITING STEEPNESS CRITERION AND THE GEOMETRIC RATIO BREAKING CRITERION AS WELL AS THE BREAKING EVENTS OBSERVED ON VIDEO STARTING FROM 180 s INTO THE SIMULATION AND ENDING AT 1300 s..... | 61 |
| FIGURE 19: REALIZATIONS OF THE DYNAMIC/KINEMATIC BREAKING ONSET CRITERION OVER THE LENGTH OF THE SIMULATION AT WAVE GAUGE 12 | 62 |
| FIGURE 20: COMPARISON OF THE TIME STAMPS OF BREAKING EVENTS MEASURED BY THE LIMITING STEEPNESS, GEOMETRIC RATIO, AND DYNAMIC/KINEMATIC BREAKING ONSET CRITERIA WITH WHAT WAS OBSERVED ON VIDEO | 64 |
| FIGURE 21: EXPERIMENTAL DATA SHOWING THE BREAKING WAVE EVENT MEASURED BY THE DYNAMIC/KINEMATIC, GEOMETRIC RATIO, AND STOKES LIMITING STEEPNESS BREAKING CRITERIA AT 891.3 s AT THE 12 TH WAVE GAUGE | 66 |
| FIGURE 22: ZOOMED IN REPRESENTATION OF THE RESULTING DYNAMIC BREAKING CRITERION RATIO OVER TIME, WITH SPECIAL ATTENTION GIVEN TO THE TIME WINDOW FROM 700-1300 s | 67 |
| FIGURE 23: EXPERIMENTAL DATA SHOWING THE BREAKING WAVE EVENT MEASURED BY THE STOKES LIMITING STEEPNESS AND GEOMETRIC RATIO BREAKING CRITERIA, BUT NOT BY THE DYNAMIC/KINEMATIC HYBRID-BREAKING ONSET CRITERION AT 406 s AT THE 12 TH WAVE GAUGE..... | 69 |
| FIGURE 24: COMPARISON OF THE TIME STAMPS OF BREAKING EVENTS MEASURED BY THE ALL OF THE STUDIED BREAKING CRITERIA WITH WHAT WAS OBSERVED ON VIDEO | 72 |
| FIGURE 25: BREAKING WAVE EVENTS FOUND FROM VIDEO OBSERVATIONS AND THE WAVE GAUGES THAT MEASURED WHEN THE LIMITING SLOPE BREAKING CRITERION WAS FULFILLED | 73 |
| FIGURE 26: PROGRESSION OF EVENT2 AT 259.8 s SHOWING BREAKING ONSET AT WAVE GAUGE 6 AND BREAKING PROCESS CONTINUING PAST WAVE GAUGE 12 AND ENDING AT WAVE GAUGE 20..... | 74 |
| FIGURE 27: PROGRESSION OF EVENT7 AT 857.9 s SHOWING BREAKING ONSET AT WAVE GAUGE 12 AND BREAKING PROCESS CONTINUING PAST WAVE GAUGE 23 | 75 |
| FIGURE 28: COMPARISON OF THE SURFACE ELEVATIONS OF THE OPENFOAM SIMULATION AND THE OUTPUT FROM THE HOS-NWT MODEL AT THE 1 ST WAVE GAUGE FOR THE TIME INVOLVING EVENT1 | 77 |
| FIGURE 29: COMPARISON OF THE SURFACE ELEVATIONS OF THE OPENFOAM SIMULATION, THE OUTPUT FROM THE HOS-NWT MODEL, AND MEASUREMENTS MADE DURING MODEL TESTING AT THE 12 TH WAVE GAUGE FOR THE TIME INVOLVING THE WAVE CREST OF EVENT7 | 78 |
| FIGURE 30: SUB-PLOTS OF SURFACE ELEVATIONS GENERATED BY THE OPENFOAM SIMULATION FOR EVENT7 | 81 |
| FIGURE 31: SCALE EMPLOYED FOR THE VISUALIZATION OF THE PARTICLE VELOCITIES, IN THE DIRECTION OF WAVE PROPAGATION, OF BOTH THE AIR AND WATER PHASES FOR EVENT7 IN FIGURE 32; UNITS ARE IN M/S | 82 |
| FIGURE 32: SUB-PLOTS OF PARTICLE VELOCITIES OF BOTH THE AIR AND WATER PHASES, IN THE DIRECTION OF WAVE PROPAGATION, GENERATED BY THE OPENFOAM SIMULATION FOR EVENT7..... | 83 |

List of Tables

| | |
|-------------------------------------------------------------------------------------------------------------------------------------------------------------------------------------------------------------------------------------------------------------------------------------|----|
| TABLE 1: LIST OF COEFFICIENTS NECESSARY FOR THE COMPLETION OF THE $K-\omega$ SST MODEL'S GOVERNING EQUATIONS | 23 |
| TABLE 2: CALCULATED SIGNIFICANT WAVE HEIGHTS BASED ON MEASUREMENTS BY THE MARINTEK WAVE GAUGES AND RESULTS FROM THE HOS-NWT SIMULATION | 48 |
| TABLE 3: TIME STAMPS OF LARGE WAVE EVENTS HAVING WAVE HEIGHTS AT LEAST 1.5 TIMES THAT OF THE SIGNIFICANT WAVE HEIGHT OF THE EXPERIMENTAL DATA AT THE 12 TH WAVE GAUGE; THE HIGHLIGHTED EVENT REPRESENTS THE ONLY TRUE ROGUE EVENT WITHIN THE DATA..... | 50 |
| TABLE 4: TIME STAMPS OF LARGE WAVE EVENTS HAVING WAVE HEIGHTS AT LEAST 1.5 TIMES THAT OF THE SIGNIFICANT WAVE HEIGHT OF THE EXPERIMENTAL DATA AT THE 12 TH WAVE GAUGE FOR THE MODEL RUN WITH LOWER STEEPNESS | 53 |
| TABLE 5: TIME STAMPS FOR BREAKING WAVE EVENTS THAT WERE CAPTURED ON VIDEO FOR THE MODEL RUN WITH A HIGHER LEVEL OF STEEPNESS $\epsilon_c = 13.46\%$ | 55 |
| TABLE 6: TIME STAMPS OF WAVE BREAKING EVENTS FROM VIDEO CLIPS WITH GREEN HIGHLIGHTS SHOWING INSTANCES WHERE THE STOKES LIMITING STEEPNESS BREAKING CRITERION ALIGNED WITH THE EVENTS IN TABLE 5 AND RED HIGHLIGHTS SHOWING FALSE POSITIVE REALIZATIONS OF THE CRITERION..... | 56 |
| TABLE 7: TIME STAMPS OF WAVE BREAKING EVENTS FROM VIDEO CLIPS WITH GREEN HIGHLIGHTS SHOWING INSTANCES WHERE THE GEOMETRIC RATIO BREAKING CRITERION ALIGNED WITH THE EVENTS IN TABLE 5 AND RED HIGHLIGHTS SHOWING FALSE POSITIVE REALIZATIONS OF THE CRITERION..... | 59 |
| TABLE 8: TIME STAMPS OF WAVE BREAKING EVENTS FROM VIDEO CLIPS WITH GREEN HIGHLIGHTS SHOWING INSTANCES WHERE THE DYNAMIC/KINEMATIC BREAKING CRITERION ALIGNED WITH THE EVENTS IN TABLE 5 AND RED HIGHLIGHTS SHOWING FALSE POSITIVE REALIZATIONS OF THE CRITERION | 63 |
| TABLE 9: TIME STAMPS OF WAVE BREAKING EVENTS FROM VIDEO CLIPS WITH GREEN HIGHLIGHTS SHOWING INSTANCES WHERE THE LIMITING SLOPE BREAKING CRITERION ALIGNED WITH THE EVENTS IN TABLE 5 AND RED HIGHLIGHTS SHOWING FALSE POSITIVE REALIZATIONS OF THE CRITERION | 70 |
| TABLE 10: ERRORS BETWEEN THE WAVE CRESTS FROM THE HOS-NWT MODEL OUTPUT AND EXPERIMENTAL DATA, AT WAVE GAUGE 12, FOR THE BREAKING EVENTS IDENTIFIED BY THE LIMITING SLOPE BREAKING CRITERION | 79 |

Nomenclature

GREEK SYMBOLS

| | |
|---------------------------|------------------------------------------------------------------------------|
| α_R | RELAXATION ZONE SPATIAL WEIGHTING FACTOR [JACOBSEN ET AL. 2012] |
| β^* | K - ω SST CLOSURE COEFFICIENT |
| β_1 | K - ω SST CLOSURE COEFFICIENT |
| β_2 | K - ω SST CLOSURE COEFFICIENT |
| γ | SURFACE TRACKING PARAMETER FOR VOLUME OF FLUID METHOD [JACOBSEN ET AL. 2012] |
| δ_1 | K - ω SST CLOSURE COEFFICIENT |
| δ_2 | K - ω SST CLOSURE COEFFICIENT |
| ∇ | HORIZONTAL GRADIENT OPERATOR |
| ∇_v | VERTICAL GRADIENT OPERATOR |
| ϵ | INDIVIDUAL WAVE STEEPNESS [STOKES 1880] [MICHELL 1893] |
| ϵ_c | COLLECTIVE WAVE STEEPNESS OF SEA-SURFACE PROCESS [BONNEFOY ET AL. 2010] |
| η | FREE-SURFACE ELEVATION |
| κ | HEAT CONDUCTIVITY |
| κ_γ | SURFACE CURVATURE |
| μ | DYNAMIC VISCOSITY OF A FLUID |
| μ_t | DYNAMIC EDDY VISCOSITY |
| ρ | DENSITY |
| σ_{k1} | K - ω SST CLOSURE COEFFICIENT |
| σ_{k2} | K - ω SST CLOSURE COEFFICIENT |
| $\sigma_{\omega 1}$ | K - ω SST CLOSURE COEFFICIENT |
| $\sigma_{\omega 2}$ | K - ω SST CLOSURE COEFFICIENT |
| σ_T | SURFACE TENSION COEFFICIENT |
| τ | REYNOLDS STRESS TENSOR |
| ϕ | VELOCITY POTENTIAL |
| $\tilde{\phi}$ | FREE-SURFACE VELOCITY POTENTIAL |
| ϕ_{add} | ADDITIONAL WAVEMAKER VELOCITY POTENTIAL |
| χ_R | RELAXATION ZONE SPATIAL WEIGHTING FACTOR [JACOBSEN ET AL. 2012] |
| ω | CHARACTERISTIC FREQUENCY OF TURBULENCE |

LATIN SYMBOLS

| | | |
|----------------------|-------|-----------------------------------------------------------------|
| A_m | | MODAL COEFFICIENT FOR ϕ |
| a | | WAVE AMPLITUDE |
| a_1 | | k - ω SST CLOSURE COEFFICIENT |
| B_x | | DYNAMIC BREAKING ONSET CRITERION RATIO [BARTHELEMY ET AL. 2018] |
| B_m^η | | MODAL COEFFICIENT FOR η |
| $B_m^{\tilde{\phi}}$ | | MODAL COEFFICIENT FOR $\tilde{\phi}$ |
| c | | INDIVIDUAL WAVE PHASE SPEED |
| C | | INDIVIDUAL WAVE PHASE SPEED |
| C_x | | WAVE CREST VELOCITY IN THE DIRECTION OF WAVE PROPAGATION |
| $CD_{k\omega}$ | | k - ω SST CLOSURE COEFFICIENT |
| E | | LOCAL ENERGY DENSITY |
| f_v | | VERTICAL GEOMETRY OF WAVEMAKER |
| F_1 | | k - ω SST BLENDING FACTOR |
| F_2 | | k - ω SST BLENDING FACTOR |
| F_x | | ENERGY FLUX IN THE DIRECTION OF WAVE PROPAGATION |
| F_x, F_y, F_z | | NAVIER STOKES BODY FORCES IN X, Y, AND Z DIRECTIONS |
| g | | GRAVITY |
| h | | WATER DEPTH |
| H | | WAVE HEIGHT |
| H_s | | SIGNIFICANT WAVE HEIGHT |
| $H[\eta]$ | | PARTIAL HILBERT TRANSFORM OF SURFACE ELEVATION |
| I | | TURBULENCE INTENSITY |
| M | | HOS-NWT NON-LINEARITY ORDER |
| k | | WAVE NUMBER |
| k | | TURBULENT KINETIC ENERGY PER UNIT MASS |
| k_m | | MODAL WAVE NUMBERS |
| p | | PRESSURE |
| p^* | | PRESSURE IN ADDITION TO HYDROSTATIC |
| \mathcal{P}_k | | PRODUCTION TERM FOR k - ω SST TURBULENCE MODEL |
| R | | FIRST DERIVATIVE OF SURFACE ELEVATION |
| S | | SLOPE OF WAVE INCLINATION |
| S | | STRAIN RATE TENSOR |

| | | |
|----------------|-------|--------------------------------------------------------------|
| t | | TIME |
| T | | WAVE PERIOD |
| T | | TEMPERATURE |
| T_p | | PEAK WAVE PERIOD |
| u | | FLUID VELOCITY IN X-DIRECTION |
| \mathbf{u} | | FLUID VELOCITY IN X, Y, AND Z DIRECTIONS |
| \mathbf{u}_r | | RELATIVE VELOCITY OF A FLUID |
| U | | WATER PARTICLE VELOCITY |
| U_x | | WATER PARTICLE VELOCITY IN THE DIRECTION OF WAVE PROPAGATION |
| v | | FLUID VELOCITY IN Y-DIRECTION |
| w | | FLUID VELOCITY IN Z-DIRECTION |
| W | | VERTICAL VELOCITY AT THE FREE SURFACE |
| x, y, z | | CARTESIAN COORDINATES FOR X, Y, AND Z DIRECTIONS |
| \mathbf{x} | | CARTESIAN COORDINATE FOR X, Y, AND Z DIRECTIONS |
| X | | WAVEMAKER MOTION |
| \tilde{X} | | ORIENTATION OF WAVEMAKER PADDLE |

Abbreviations

| | | |
|----------|-------|------------------------------------------------|
| BEM | | BOUNDARY ELEMENT METHOD |
| CFD | | COMPUTATIONAL FLUID DYNAMICS |
| ECN/CNRS | | ECOLE CENTRALE NANTES, LHEEA LAB |
| DES | | DETACHED EDDY SIMULATION |
| FDM | | FINITE DIFFERENCE METHOD |
| FFT | | FAST FOURIER TRANSFORM |
| HOS | | HIGH ORDER SPECTRAL METHOD |
| HOS-NWT | | HIGH ORDER SPECTRAL NUMERICAL WAVE TANK |
| LES | | LARGE EDDY SIMULATION |
| RANS | | REYNOLDS AVERAGED NAVIER STOKES |
| SST | | SHEAR STRESS TRANSPORT |
| SWENSE | | SPECTRAL WAVE EXPLICIT NAVIER STOKES EQUATIONS |
| VOF | | VOLUME OF FLUID METHOD |
| VTK | | VISUALIZATION TOOLKIT |

2. Introduction:

A clear understanding and appreciation for waves, and the loads associated with them, is of the utmost importance in the context of ocean engineering and offshore technology. With the continuing trend of climate change, as well as the tendency of more energy resources (oil, gas, wind, etc.) being harnessed in deeper waters, the likelihood of offshore structures and/or vessels encountering large waves is increasing. Extreme wave events, such as the occurrence of “Rogue”, “Giant”, or “Freak” waves [Kharif & Pelinovsky 2003] are dangerous events that, if unaccounted for, could lead to catastrophic failures of an offshore installation, the capsizing of a vessel, or possible loss of life from events such as these [Kjeldsen & Myrhaug 1980]. Rogue waves themselves are considered to be waves that possess wave heights two times larger than that of the significant wave height characterizing the sea-state that they appear in [Kharif & Pelinovsky 2003]. Specifically, rogue waves have been measured to reach wave heights of nearly 26 m in significant wave conditions of only 12 m, as was the case for the “New Year’s Wave” at the Draupner jacket platform in the North Sea on the 1st of January 1995 [Haver & Anderson 2000] [Haver 2004] [Kharif & Pelinovsky 2003]. The nonlinear growth and behaviors existing within wave events such as these cannot accurately be described by commonplace linear numerical methods.

Due to the shortfalls associated with different linear numerical methods, several efforts have been made to develop different fully non-linear potential flow solvers, which are dedicated to the accurate description of wave environments where realizations of extreme/rogue wave events can occur [Ducrozet et al. 2007]. Three of the more popular fully non-linear potential flow solving schemes are the Boundary Element Method (BEM), the high-order Finite Difference Method (FDM), and the High Order Spectral (HOS) method.

The BEM solves fully non-linear potential flow equations, at the boundaries of a defined domain, and can be applied to both 2D and 3D scenarios for regular and irregular wave fields [Grilli et al. 2001]. The advantage of solving the non-linear equations at the boundaries is that reflective and/or absorbing boundary conditions

[Grilli et al. 2001] can be applied within the model, which in turn reduces the number of unknowns within the governing equations [Ducrozet et al. 2017]. Currently, the limitations associated with this method are due to the high computational effort needed when applying the BEM to large-scale and long-term computations [Fochesato et al. 2007].

The FDM has been applied to fluid domains in the form of the OceanWave3D model, as outlined in Paulsen et al. [2014]. This model is primarily geared towards wave-wave, wave-bottom, and wave-structure interactions and has been capable of generating efficient and accurate solutions in both 2D and 3D scenarios [Bingham & Zhang 2007][Engsig-Karup et al. 2009][Ducrozet et al. 2012]. Research from Ducrozet et al. [2012] has made a comparison of the capabilities of the OceanWave3D FDM and the HOS method. The conclusions of the study showed that for waves with a higher order of non-linearity, the HOS method was found to be more efficient and accurate, whereas, the OceanWave3D FDM would be more efficient for lower order finite difference schemes when a lower degree of accuracy is necessary. Research also showed that the length of the simulation factors into the overall efficiency of the OceanWave3D FDM versus the HOS method. It was found that the longer the simulation, the less efficient the FDM becomes in comparison.

The HOS method is a pseudo-spectral method that solves the governing non-linear potential flow equations solely on the free surface of the waves. It does this by partially solving the equations in physical space and partially within spectral space through the utilization of Fourier Transforms. Some of the advantages associated with this method are its capabilities for efficiently determining accurate solutions of wave environments at the free surface, [Dommermuth & Yue 1987] [West et al. 1987] and its applicability to regular and irregular waves in 2D and 3D wave fields over long periods of time and areas on the scale of multiple square kilometers [Ducrozet et al. 2016]. However, it is limited in its current state to having constant water depth throughout the model, whereas the BEM and FDM have the capability to handle complex bottom topographies [Grilli et al. 2001] [Ducrozet et al. 2012].

Many utilizations of the HOS method, in the form of different models, have been extensively studied, including research related to nonlinear wave-wave interactions that include atmospheric forcings [Dommermuth & Yue 1988], interactions between long and short waves [Zhang et al. 1993], the use of the method with the inclusion of submerged floating bodies [Liu et al. 1992] [Zhu 2000], and finite depth and depth varying studies [Liu & Yue 1998], among others

Two open-source models that utilize the HOS method have been developed to solve for the propagation of nonlinear wave fields in the open ocean (HOS-ocean) [Ducrozet et al. 2016] and/or in numerically generated wave tanks (HOS-NWT) [Ducrozet et al. 2012]. HOS-ocean & HOS-NWT were developed at Ecole Centrale Nantes, LHEEA Lab (ECN/CNRS).

It is important to note that the FDM, BEM and HOS methods are fully non-linear potential flow models; because of the potential flow assumptions that are inherently made whilst utilizing any of these methods, viscous effects are neglected, the fluid in the model is presumed to be incompressible, and irrotationality is assumed. Nested within these assumptions is the inability for the FDM, BEM or the HOS method to account for breaking waves [Seiffert et al. 2017]. Efforts are being made to identify a “breaking onset criteria” [Seiffert et al. 2017] [Barthelemy et al. 2018][Grilli et al. 2001][Grilli et al. 1989][Saket et al. 2015] and applying it to predict when and where breaking wave events may occur within a large spatial domain over a long period of time.

In this study, the open-source HOS-NWT model will be used to numerically recreate a 3D model test, performed at MARINTEK, an ocean laboratory research center located in Trondheim, Norway. The data from this test will firstly be utilized to validate the HOS model under extreme waves in deep water on a flat seabed. Secondly, efforts will be undertaken to find whether the HOS-NWT model, linked with an appropriate breaking onset criterion, can identify breaking wave conditions in deep water. Lastly, work will be done to couple the HOS-NWT software to the CFD software OpenFOAM in an attempt to simulate breaking wave events, identified using an appropriate breaking onset criterion.

3. Background & Theory:

3.1 HOS Method:

The HOS method itself was first developed in the late 1980s by two different sources, West et al. [1987] and Dommermuth & Yue [1987], around the same time. In the HOS method, the differential equations describing surface waves are solved using a pseudo-spectral approach for different orders of nonlinearity. In pseudo-spectral methods, problems are partially solved in both physical and spectral space; projection between each domain is performed using Fourier Transforms. A major advantage of the method is its low CPU cost, enhanced through the application of Fast Fourier Transforms (FFTs). FFTs enable the use of a large number of wave harmonics, realistically describing an ocean wave field. Multiple validations of this method have been conducted to assess the accuracy and the stability of the HOS method [Ducrozet et al. 2012] [Bonnetfoy et al. 2010]. The results of these validations show that authentic simulations of 3D focused extreme events are possible, and that because of the models' capability of dealing with complex 3D sea states, such as these, show that the HOS method has the ability to reproduce any experiment in a rectangular fluid domain, with the exception of breaking waves [Ducrozet et al. 2012][Ducrozet et al. 2016].

As mentioned in the Introduction, HOS-ocean and HOS-NWT are efficient High-Order Spectral codes developed to solve for the propagation of nonlinear wave fields for both 2D and 3D cases. Both codes are open-source HOS models developed at Ecole Centrale Nantes, LHEEA Lab (ECN/CNRS), but the focus of this study primarily revolves around the use of the HOS-NWT code. Each code was developed and redistributed under the terms of the GNU General Public License as published by the Free Software Foundation.

3.1.1 Boundary Conditions:

The use of a rectangular fluid domain when using the HOS method makes way for the use of a Cartesian coordinate system. The origin of this coordinate system, within the HOS-NWT model, is oriented at one of the corners of the

considered fluid domain. Dimensions of the domain, in both the x and y directions, can be defined based on whether a 2D or 3D case is of interest (in a 2D case the y-direction would be omitted). A z direction, positively oriented upward, can be used to measure the free surface of waves propagating in the domain, where the location of $z=0$ is at the mean free surface.

As previously mentioned, within potential flow solvers, assumptions are made which make the flow within the model incompressible, inviscid, and irrotational. Under these assumptions, the continuity equation reduces to the Laplace equation, represented in Equation 1, where ϕ is the velocity potential, and ∇ is the horizontal gradient operator.

$$\nabla^2 \phi + \frac{\partial^2 \phi}{\partial z^2} = 0 \quad [1]$$

Upon the definition of the Laplace Equation, it is necessary for boundary conditions to be set for the domain of interest. In wave mechanics, it is necessary to define two boundary conditions at the free surface, known as the kinematic and dynamic free surface boundary conditions, shown in Equations 2 and 3, respectively. In addition to these, another boundary condition must be defined at the seafloor recognized as the bottom boundary condition, illustrated in Equation 4, where h is the depth of the seafloor. For simplicity sake, the expansion of each of the boundary conditions and their respective parameters are done for a 2 dimensional case in the x and z directions. Within the HOS-NWT code, the free surface boundary conditions were developed following the methodology of Zakharov [1968]. To adhere to this methodology, the use of appropriate surface quantities for free surface elevation, η , and free surface velocity potential, $\tilde{\phi}(x, z = \eta(x, t), t)$, are present within the code [Ducrozet et al. 2016]. Both the kinematic and dynamic free surface boundary conditions contain the parameter W from the Zakharov methodology, which represents the vertical velocity at the free surface: $W(x, t) = \frac{\partial \phi}{\partial z}(x, z, t)$, where $z = \eta(x, t) \Rightarrow$ commonly referred to as the Dirichlet problem.

$$\frac{\partial \eta}{\partial t} = (1 + |\nabla \eta|^2)W - \nabla \tilde{\phi} \nabla \eta \quad [2]$$

$$\frac{\partial \tilde{\phi}}{\partial t} = -g\eta - \frac{1}{2}|\nabla \tilde{\phi}|^2 + \frac{1}{2}(1 + |\nabla \eta|^2)W^2 \quad [3]$$

Within the HOS-NWT code, W is evaluated based upon the HOS scheme of West et al. [1987] [Ducrozet et al. 2016].

$$\frac{\partial \phi}{\partial z}(x, z, t) = 0; z = -h \quad [4]$$

Upon the evaluation of the vertical velocity, W , a 4th order Runge-Kutta scheme allows for the time integration and computation of η and $\tilde{\phi}$ by advancing Equations 2 and 3 further in time with adaptive step sizes [Cash & Karp 1990]. The step sizes are chosen to adhere to a particular tolerance set by the specified Runge-Kutta scheme, for accurate computation of the model. The tolerance value choice depends primarily on the order of nonlinearity in the wave field as well as the overall duration of the simulation.

Another set of boundary conditions are applied within the HOS-NWT model, that create completely reflective lateral boundaries, as to mirror the properties of a physical wave tank [Ducrozet et al. 2016].

In order to tap into the advantages associated with the HOS method's minimal computational effort, Equations 2 and 3 must be defined within the spectral domain along with the velocity potential ϕ . Once in the spectral domain, FFTs are selected to enable the use of a large number of wave harmonics, in order to realistically describe the ocean wave field. The spectral form of the velocity potential, free surface velocity potential, and surface elevation are depicted in Equations 5, 6, and 7, respectively, where A_m , $B_m^{\tilde{\phi}}$, and B_m^η are the modal coefficients for each respective case and where $k_m = m\Delta k_x = m\frac{2\pi}{L_x}$ is representative of the wavenumbers.

$$\phi(x, z, t) = \sum_m A_m(t) \frac{\cosh[k_m(z+h)]}{\cosh[k_m h]} \exp [ik_m x] \quad [5]$$

$$\tilde{\phi}(x, t) = \sum_m B_m^{\tilde{\phi}}(t) \exp [ik_m x] \quad [6]$$

$$\eta(x, t) = \sum_m B_m^{\eta}(t) \exp [ik_m x] \quad [7]$$

The Taylor expansion and numerical truncation of Equations 5, 6, and 7 are evaluated up to a set number of modes, equivalent to a user specified HOS order of nonlinearity, M.

The continuance of the HOS procedure, after the development of η and $\tilde{\phi}$ on the surface, leads to the evaluation of the vertical velocity $W(x, t)$. The procedure for determining $W(x, t)$ is initiated, through a series expansion of the velocity potential up to HOS order M, represented in Equation 8.

$$\phi(x, z, t) = \sum_{m=1}^M \phi^{(m)}(x, z, t) \quad [8]$$

Expanding the Taylor series around $z=0$ simplifies the Dirichlet problem by defining the velocity potential at the mean free surface, $z=0$, M number of times and not at every pertinent surface elevation, $z = \eta$; where, for the first order of M, the velocity potential at $z=0$ is equivalent to the free surface velocity potential. The collection of terms for each order of wave steepness leads to a triangular system of equations defined by Equations 9 & 10. This Taylor expansion of the simplified calculation of the Dirichlet problem sets HOS order M equal to 1 for Equation 9 and for orders greater than 1 in Equation 10.

$$\phi^{(1)}(x, z = 0, t) = \tilde{\phi}(x, t) \quad [9]$$

$$\phi^{(m)}(x, z = 0, t) = - \sum_{k=1}^{m-1} \frac{\eta^k}{k!} \frac{\partial^k \phi^{m-k}}{\partial z^k}(x, z = 0, t) \quad [10]$$

A similar series expansion for the vertical velocity $W(x, t)$ leads to another triangular system, which is solved iteratively within the model. For the purposes of this study, the value for M was set equal to 8, as to allow for fully non-linear simulations from the HOS-NWT model.

Equations 11 and 12 are representative of the free surface velocity of interest found through the summation of the values of $W^{(m)}$ over the set order of nonlinearity.

$$W(x, t) = \sum_{m=1}^M W^{(m)}(x, z, t) \quad [11]$$

$$W^{(m)}(x, t) = \sum_{k=0}^{m-1} \frac{\eta^k}{k!} \frac{\partial^{k+1} \phi^{(m-k)}}{\partial z^{k+1}}(x, z = 0, t) \quad [12]$$

With all of the building blocks in place (η , $\tilde{\phi}$, W , and M), in theory, the evaluation of an efficient and accurate solution for a wave surface profile could be conducted over a long time period for a large spatial domain.

However, for the HOS-NWT code [Ducrozet et al. 2012], an additional potential parameter must be defined in order for the model to generate waves from a wavemaker [Agnon & Bingham 1999]. This calls for the separation of the overall potential function into the free surface velocity potential, $\tilde{\phi}$, and an additional potential, ϕ_{add} , accounting for wave generation from a wavemaker shown below in Equation 13.

$$\phi = \tilde{\phi} + \phi_{add} \quad [13]$$

Due to the expansion illustrated in Equation 13, the boundary conditions shown in Equations 2 and 3 must be rewritten to include the additional term within the potential function, shown in Equations 14 and 15.

$$\frac{\partial \eta}{\partial t} = (1 + |\nabla \eta|^2)W - \nabla(\tilde{\phi} + \phi_{add})\nabla \eta + \frac{\partial \phi_{add}}{\partial z} \quad [14]$$

$$\begin{aligned} \frac{\partial \tilde{\phi}}{\partial t} = & -\eta - \frac{1}{2} |\nabla \tilde{\phi}|^2 + \frac{1}{2} (1 + |\nabla \eta|^2) W^2 - \\ & \nabla \tilde{\phi} \nabla \phi_{add} - \frac{1}{2} |\tilde{\nabla} \phi_{add}|^2 - \frac{\partial \phi_{add}}{\partial t} - \nu \frac{\partial \eta}{\partial t} \end{aligned} \quad [15]$$

The final two boundary conditions developed within the HOS-NWT code are for both the interaction of the fluid and the wavemaker and the interaction of the fluid with an absorption zone on the opposite end of the domain to the wavemaker. Firstly, the wavemaker boundary condition can be expressed as a no-flow condition, meaning that no fluid can penetrate the face of the wavemaker. The motion of the wavemaker can be defined as a function of its vertical geometry and the expression of the location of the paddle with respect to space and time. A representation of this is shown in Equation 16, where wavemaker motion, X , is expressed in terms of the vertical geometry f_v and the orientation of the paddle \tilde{X} .

$$X(y, z, t) = f_v(z) \tilde{X}(y, t) \quad [16]$$

With this in mind, a no-flow condition is developed as the partial time derivative of the wavemaker motion, expressed in Equation 17, where ∇_v is the vertical gradient in the y and z directions.

$$\frac{\partial X}{\partial t} = \frac{\partial \phi}{\partial x} - (\nabla_v X)(\nabla_v \phi) \quad [17]$$

Additionally, an absorption zone was implemented into the HOS-NWT code to account for wave reflections at the edge of the spatial domain as to ensure a correctly modeled wave field inside the test zone. The strength of the absorption coefficient as well as the location where the absorption zone begins can be set within the inputs of the HOS-NWT code.

3.2 Experimental Data:

An extensive number of 3D model tests, performed in a wave tank at the MARINTEK Ocean Laboratory, were carried out to investigate deep-water wave breaking under long crested waves. Due to the presence of long crested waves, an assumption of two-dimensionality was possible throughout the entirety of this study. The MARINTEK Ocean Laboratory is located in Trondheim, Norway and is operated by SINTEF. This study used data from one of the steeper sea-states seen in these tests to validate the HOS-NWT model under extreme wave conditions, and to apply an appropriate breaking criterion to assess whether instances of breaking could be identified. Data was provided by the MARINTEK facility in the form of paddle motions for a single and double-hinged wave maker, as well as surface elevation measurements, made during experimentation, for steep sea-states where deep water breaking was expected to occur. The HOS-NWT code is currently incapable of configuring a double-hinged wave maker; therefore the data, with respect to the single-hinged paddle, was used for this study. In the future, efforts could be made to further develop the HOS-NWT model to allow for the configuration of a double-hinged wave maker, however, this is outside the scope of the present study.

The provided surface elevation data has been used as reference data for the HOS-NWT model; the measurements were made using 23 different wave gauges with a spacing of 15cm over a total length of 3.3m. These measurements were used to show the accuracy of the output of the HOS-NWT model with respect to what was measured, and in some instances were also used to investigate the growth of events that were expected to be breaking waves. A separate wave gauge set apart from the 23 gauges, known as the WAVE3 gauge, was of particular importance for the initialization of the simulation, explained further in Section 4.1.2.

For this study, a single location of interest, located in the center of the MARINTEK wave tank, was used to identify extreme and breaking events. All physical model tests begin by calibrating the waves at the location where a particular structure will be tested. The position of the 12th Wave Gauge within the

series of 23 gauges, for this study, corresponded to the position where the calibration was being performed. Figure 1 shows the testing apparatus that was in place whilst measurements were being made in the MARINTEK Lab; Figure 2 shows an example of measurements made by each of the 23 different wave gauges over a small time window.



Figure 1: Wave Gauge Apparatus used for testing in the MARINTEK Ocean Laboratory

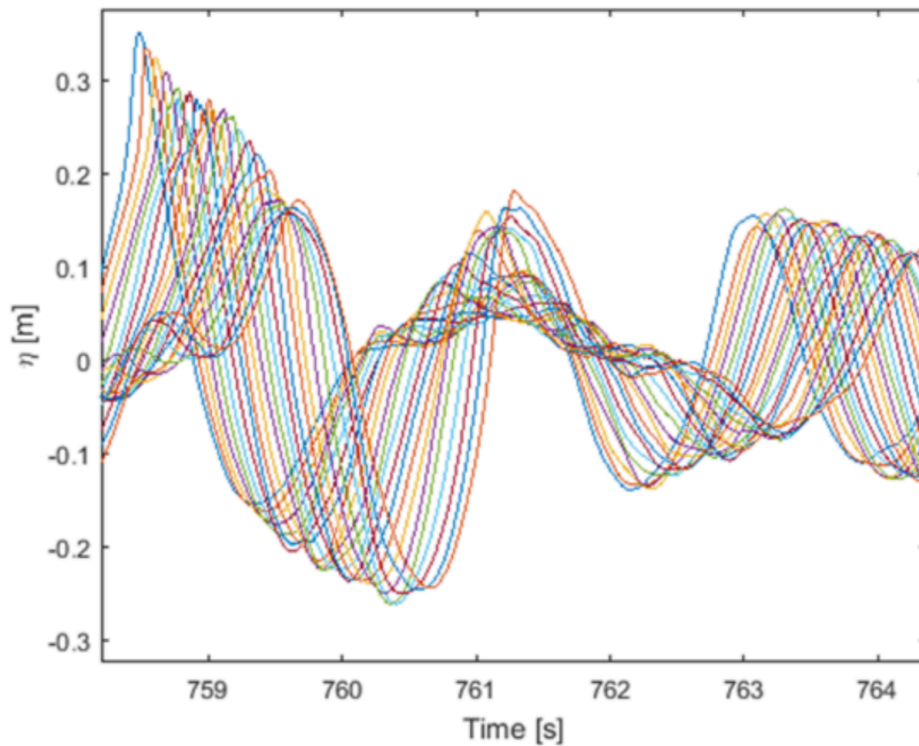


Figure 2: Measurements made over an arbitrary window in time using the set up in Figure 1

3.3 Breaking Onset Criteria:

An important aspect of this study was the identification of breaking wave events at Wave Gauge 12, over the course of the HOS-NWT simulation. As mentioned previously, the HOS-NWT model is a fully non-linear potential flow solver that adheres to the potential flow assumptions of incompressible, inviscid, and irrotational flow. These assumptions inherently disallow the formation of breaking waves within the model. Because of this fact, in the presence of large breaking waves, the HOS-NWT model produces unnatural high frequency oscillations on the free surface, which can lead to numerical instabilities [Seiffert & Ducrozet 2016]. This unrealistic behavior of a wave, which in nature would overturn, is due to the fact that the HOS model solves for a single-valued free surface, and these high frequencies develop instead of showing a broken free surface within the model [Seiffert et al. 2017].

A significant amount of research has been invested into developing a breaking onset criterion, within the HOS-NWT code, which allows for the identification of the point at which the surface of a water wave would begin to deform and become unstable [Seiffert et al. 2017].

The traditional classification of a wave-breaking onset criterion can be split into three different classes: geometric, kinematic, and dynamic [Seiffert et al. 2017]. Research by Perlin et al. [2013] has been done to identify and show the strengths and limitations of each of the classes' abilities to form an accurate breaking onset criterion.

3.3.1 Geometric Breaking Criteria:

There are a number of different selections for breaking criteria within the geometric class of wave-breaking onset; initially, a limiting steepness parameter was investigated. Findings from Babanin et al. [2011] suggest that the limiting steepness of an individual wave should be equivalent to the Stokes limiting steepness, whereas other experimental studies, such as Tian et al. [2008], concluded that the limiting steepness is lower than that of the Stokes limiting steepness and can vary depending upon the type of breaking wave that is present (i.e. spilling, plunging, etc.). Research conducted on the numerical implementation of this method [Barthelemy et al. 2018] and complementary experimental research by Saket et al. [2015] suggests that the variation in the value of the steepness during different breaking conditions make this criterion unsuitable for a robust breaking onset criterion [Seiffert et al. 2017]. The research by Seiffert et al. [2017] explains that due to the irregular nature of wave crests in an irregular wave simulation, there is a high level of complexity related to the implementation of this criterion within numerical simulations. The complexities can be associated with the matter of repeating this criterion over a large computational domain in an accurate manner. This led to a conclusion by Seiffert et al. [2017], that this criterion was less viable to introduce into different numerical models in comparison with other breaking criteria.

However, implementing such a criteria as a post-processing measure is more feasible. Instead of introducing the complexities associated with introducing the breaking criterion into the numerical simulation of HOS-NWT, the criterion can be applied to the output of the model. Three separate geometric breaking criteria, including the criterion researched by Babanin et al. [2011], were implemented in this way, each focusing on a different geometric parameter of individual irregular waves.

The aforementioned steepness criterion research by Babanin et al. [2011] stated that breaking waves were dependent upon the Stokes Limiting Steepness of individual irregular waves. In a mathematical sense, the criterion states that the steepness of a single wave cannot not exceed a limiting threshold, $\epsilon = ak < 0.443$, where each wave's amplitude, a , and wave number, k , are used to define the steepness [Stokes 1880] [Michell 1893].

In addition to the Stokes Limiting Steepness Geometric Breaking Criterion, the second criterion, known as the Geometric Ratio Criterion, was related to a geometric ratio between gravity, and both the individual irregular wave's period, T , and wave height, H , expressed in Equation 18 [Ochi & Tsai 1983]. The research from Ochi & Tsai [1983] found that if the ratio went unsatisfied, breaking was expected to occur.

$$\frac{0.02gT^2}{H} \geq 1 \quad [18]$$

The final geometric breaking condition researched as a possible post-processing measure to identify breaking waves was based upon a limiting slope of individual irregular waves [Longuet-Higgins & Fox 1977] [Longuet-Higgins & Smith 1983]. The concept behind this criterion is that there is a limiting slope of wave inclination, $S_{Max} = 0.586$, that a progressive wave can maintain before breaking develops. The slope of wave inclination was determined through the use of Equation 19 [Longuet-Higgins & Smith 1983], where R is equivalent to the first derivative of the surface elevation, and c is equivalent to the phase speed of individual irregular

waves. The individual wave number, k , and the formulation of wave phase speed, c , are expanded in Equations 20 and 21 respectively.

$$S = \frac{R}{c} \quad [19]$$

$$k = \frac{1}{g} * \frac{2\pi}{T^2} \quad [20]$$

$$c = \frac{gT}{2\pi} * (1 + k^2) * \left(\frac{H}{2}\right)^2 \quad [21]$$

A conflicting point of view, set forth in Babanin [2011], states that this limiting slope criterion is better suited as a tool to measure different properties and statistics of breaking waves in progress rather than as a predictive breaking onset criterion. This point of disagreement between the Babanin [2011] and the Longuet-Higgins & Smith [1983] studies is analyzed further in Section 5.3.4 of this report, where a comparison of all of the studied breaking criteria is made.

3.3.2 Kinematic Breaking Criteria:

The second class of wave-breaking onset criteria are related to the kinematic properties of waves. In a traditional kinematic sense, it is believed that breaking onset begins at the point where the horizontal water particle velocity at the crest of a wave exceeds the instantaneous crest velocity of the wave itself. Equation 22 shows the ratio of the particle velocity and phase speed as well as the theoretical condition when breaking is believed to occur.

$$\frac{u}{c} \geq 1 \quad [22]$$

In a theoretical sense, this condition could be applied to a numerical simulation, however studies conducted by Stansell & MacFarlane [2002] have shown that the threshold of the criteria expressed in Equation 22, can actually underestimate the amount of breaking. Stansell & MacFarlane [2002] performed experiments to investigate wave-breaking criteria dependent upon phase speed; the

results showed that for different types of breaking waves (i.e. plunging, spilling, etc.) the kinematic breaking ratio could be less than one when breaking occurs.

3.3.3 Dynamic Breaking Criteria:

The dynamic class of breaking criteria has been shown to be viable for use within numerical simulations [Seiffert et al. 2017]. The most applicable dynamic criteria for breaking waves in the HOS-NWT model, was developed by Barthelemy et al. [2018]. The foundation of this breaking criterion is based on a belief that waves cannot remain stable when experiencing an excess of local wave energy flux. The criteria, given in Equation 23, was outlined in the study by Barthelemy et al. [2018]; their research found that breaking occurred for a narrow range of $0.85 < B_x < 0.86$. The equation itself consists of three different parameters, where F_x is energy flux in the direction of wave propagation, E is the local energy density, and C_x is the crest velocity in the direction of wave propagation. In Equation 23, it is assumed that the direction of wave propagation is in the x-direction.

$$B_x = \frac{F_x/E}{C_x} \quad [23]$$

The research done by Barthelemy et al. [2018] was executed in a numerical setting, whereas, the research by Saket et al. [2015] focused on the same criterion in an experimental sense. The findings of Saket et al. [2015] agreed well with that of the numerical setting where a breaking onset threshold of $B_x = 0.84 \pm 0.016$ was found. The conclusions of Saket et al. [2015] also found that the determined threshold was robust for different wave groups and steepnesses [Seiffert et al. 2017]. Additionally, other work using BEM models [Grilli et al. 2001] utilized the same threshold as Barthelemy et al. [2018] of $0.85 < B_x < 0.86$, showing that this criterion has a good range of application between different numerical models.

The modified HOS-NWT model that accounts for breaking waves using the methodology of Barthelemy et al. [2018] has yet to be publicly released. Because of this fact, steps were taken in an effort to implement the breaking criterion manually

into the HOS-NWT model. However, it was determined that enlisting this criterion as a post-processing measure allowed for a lower level of complexity when attempting to formulate different parameters such as wave number and phase speed. The benefit of implementing the criterion in this way is that individual waves could be studied, rather than attempting to formulate each of these parameters at every location within the computational domain.

For a model run within a two dimensional domain, a simplification of the breaking criterion can be made to the dynamic condition in Equation 23; this equation can be manipulated into a kinematic breaking criterion, represented in Equation 24. This modification shows the relation between the dynamic and kinematic classes, and how this breaking criterion can be considered a kinematic breaking onset criterion as was mentioned in the previous section of this paper.

$$B_x = \frac{F_x/E}{C_x} = \frac{U_x}{C_x} > 0.86 \quad [24]$$

In theory, the parameter B_x can be calculated at every point within the domain of the HOS-NWT model, and at every time step to identify any instances of random breaking waves [Seiffert & Ducrozet 2016]. The difficulty associated with determining when the breaking threshold is experienced, within a numerical simulation, comes with the calculation of the instantaneous crest velocity C_x . The equation for this is shown in Equation 25 and the necessary parameter of the local wave number, $k(x, t)$, is shown in Equation 26, following the methodology of the research conducted by Kurina & Van Groesen [2014].

$$C_x(x, t) = \sqrt{\frac{g \tanh(k(x, t)h)}{k(x, t)}} \quad [25]$$

The expansion of the parameter for the local wave number, in Equation 26, can be calculated at every location within a 2D sample during every time step, where the function denoted by $H[\eta]$ is the partial Hilbert Transform of surface

elevation, η , with respect to x . The evaluation of the wave number, $k(x, t)$, is undertaken due to the difficulty of identifying the phase speed C_x , for an irregular wave that is not in its permanent form [Kurina & Van Groesen 2014].

$$k(x, t) = \frac{1}{\eta^2 + H^2[\eta]} \left(\eta \frac{\partial}{\partial x} H[\eta] - H[\eta] \frac{\partial}{\partial x} \eta \right) \quad [26]$$

In an effort to uncouple the calculation of the phase speed of each wave from the formulation of the wave number at every point, the locations of the crests of the irregular waves in time were identified at the locations of the wave probes in the data as to avoid the issue of determining the phase speeds of waves not in their permanent form.

Lastly, the formulation of the water particle velocity was found through the use of Equation 27.

$$U_x = \frac{\partial \phi}{\partial x} (z = \eta) \quad [27]$$

3.4 OpenFOAM

Open Field Operation And Manipulation (OpenFOAM) is a computational fluid dynamics (CFD) software that was created by Henry Weller in 1989. It was originally developed under the name “FOAM” and was released as an open-source software package as “OpenFOAM” by Henry Weller, Chris Greenshields, and Mattijs Janssens in 2004. Since then, OpenFOAM has continually been updated, with new versions being released each year [OpenFOAM Foundation 2019]. The current version of OpenFOAM released in 2018 was version 6. However, for the purposes of this study, OpenFOAM version 2.4 was employed due to its ability to be linked with the waves2Foam library outlined in Section 3.4.3.

The structure of OpenFOAM can be explained as a library containing a number of codes written in the C++ programming language. Due to its open-source nature, users have the capability to adjust and customize the codes within the library to suit their individual needs [Chai & Liew & Lee 2018]. There is a very wide

range of applicability for OpenFOAM; it has the capability of formulating accurate results for simple fluid scenarios such as incompressible and compressible fluid flows, while at the same time, accurate simulations of other highly complex scenarios, such as breaking waves and fluid-structure interactions, are also achievable [Robertson et al. 2015].

The Navier Stokes equations are used as the basis for the OpenFOAM software. In general, fluid flow can be characterized by eight different parameters. These parameters consist of: the variables that represent the velocity of a fluid in the x, y, and z directions (u, v, and w), pressure (p), temperature (T), the dynamic viscosity of a fluid (μ), heat conductivity (κ), and a fluid's density (ρ) [Khalid 2016]. For the purposes of this study, temperature and heat conductivity were considered insignificant, thus minimizing the number of equations within OpenFOAM that were critical for the proper formulation of fluid flow. These critical equations are recognized as the Continuity Equation, represented as Equation 28, and the conservation of momentum equations for a fluid domain in the x, y, and z directions (Navier-Stokes Equations), illustrated in Equations 29-31, respectively [Higuera et al. 2013].

$$\frac{\partial \rho}{\partial t} + \frac{\partial(\rho u)}{\partial x} + \frac{\partial(\rho v)}{\partial y} + \frac{\partial(\rho w)}{\partial z} = 0 \quad [28]$$

$$\rho \frac{\partial u}{\partial t} + \rho u \frac{\partial u}{\partial x} + \rho v \frac{\partial u}{\partial y} + \rho w \frac{\partial u}{\partial z} = -\frac{\partial p}{\partial x} + \mu \left[\frac{\partial^2 u}{\partial x^2} + \frac{\partial^2 u}{\partial y^2} + \frac{\partial^2 u}{\partial z^2} \right] + \rho F_x \quad [29]$$

$$\rho \frac{\partial v}{\partial t} + \rho u \frac{\partial v}{\partial x} + \rho v \frac{\partial v}{\partial y} + \rho w \frac{\partial v}{\partial z} = -\frac{\partial p}{\partial y} + \mu \left[\frac{\partial^2 v}{\partial x^2} + \frac{\partial^2 v}{\partial y^2} + \frac{\partial^2 v}{\partial z^2} \right] + \rho F_y \quad [30]$$

$$\rho \frac{\partial w}{\partial t} + \rho u \frac{\partial w}{\partial x} + \rho v \frac{\partial w}{\partial y} + \rho w \frac{\partial w}{\partial z} = -\frac{\partial p}{\partial z} + \mu \left[\frac{\partial^2 w}{\partial x^2} + \frac{\partial^2 w}{\partial y^2} + \frac{\partial^2 w}{\partial z^2} \right] + \rho F_z \quad [31]$$

In order for the OpenFOAM software to accurately formulate fluid flow, each of the unknown parameters within the above equations must be calculated at every location within a defined fluid domain. The advantage of using CFD software is that the methods employed by OpenFOAM allow for all of the necessary equations to be solved simultaneously [Khalid 2016].

Through the execution of the Navier-Stokes Equations, it is possible to find

solutions for fluid behavior when dealing with flows that are considered to be laminar. However, the capabilities of OpenFOAM also include the software's ability to employ a number of different turbulence models to allow for the simulation of turbulent flow.

3.4.1 Turbulence Models

Multiple turbulence model collections are available within the OpenFOAM software; the different collections range from Reynolds Averaged Navier Stokes models (RANS) to detached or large eddy simulations (DES) or (LES) [Robertson et al. 2015]. Within each turbulence model collection, there are a number of other more specific models that can be selected by the user, based on their needs. There is a lot of uncertainty surrounding which turbulence model is the most applicable for use in breaking wave simulations. However, the most widely studied collection of turbulence models, for this purpose, are the RANS turbulence models. Within the RANS turbulence model collection, a vast number of models have been studied for use in breaking wave simulations, for example, $k - \epsilon$ [Xie, 2013], $k - \omega$ [Chella et al., 2016], $k - \omega$ SST [Liu et al., 2018], modified $k - \omega$ and $k - \omega$ SST [Devolder et al., 2018], and Reynolds stress model [Brown et al., 2016]. A general consensus has yet to have been made as to what the best model for use in breaking wave simulations is; however, for the purposes of this study, the $k - \omega$ SST Turbulence Model was employed due to its compatibility with the version 2.4 of OpenFOAM used in this study.

3.4.1.1 RANS Turbulence Models

The models within the RANS turbulence model collection modify the governing Navier-Stokes Equations, Equations 29-31, to allow for the combined flow of both air and water, shown in Equation 32. This combined flow is paramount when attempting to run simulations involving breaking waves [Jacobsen et al. 2012]. It is important to note that in Equation 32, \mathbf{u} is representative of the velocities in the x , y , and z directions i.e. $\mathbf{u}=(u, v, w)$, ρ is density which can vary

between computational cells due to varying air/water content, p^* is pressure in addition to hydrostatic pressure, \mathbf{g} is gravitational acceleration, \mathbf{x} is representative of all three Cartesian coordinates i.e. $\mathbf{x}=(x, y, z)$, μ is the dynamic viscosity, τ is the Reynolds Stress Tensor, which is expanded in Equation 33, σ_T is the surface tension coefficient, κ_γ is the surface curvature, and γ is a surface tracking parameter that is representative of the volume of fluid method [Jacobsen et al. 2012], which is further explained in Section 3.3.2.

$$\frac{\partial \rho \mathbf{u}}{\partial t} + \nabla \rho \mathbf{u} \mathbf{u}^T = -\nabla p^* - g \mathbf{x} \nabla \rho + \nabla [\mu \nabla \mathbf{u} + \rho \tau] + \sigma_T \kappa_\gamma \nabla \gamma \quad [32]$$

$$\tau = \frac{2}{\rho} \mu_t S - \frac{2}{3} k I \quad [33]$$

The Reynolds stress tensor, illustrated in Equation 33, is a function of density ρ , the dynamic eddy viscosity μ_t , the strain rate tensor S , expanded in Equation 34, the turbulent kinetic energy per unit mass k , and the turbulence intensity I [Jacobsen et al. 2012].

$$S = \left(\frac{1}{2} (\nabla \mathbf{u} + (\nabla \mathbf{u})^T) \right) \quad [34]$$

The modified Reynolds Averaged Navier-Stokes Equations can be coupled with the Continuity Equation to allow for the description of time-averaged turbulent flows. In order to properly model different turbulent flows, more specific models within the RANS turbulence model collection must be selected.

3.4.1.1.1 k- ω SST Turbulence Model

One of the most commonly used turbulence models within the RANS turbulence model collection is the k- ω Shear Stress Transport (SST) Turbulence Model. The original k- ω SST model is based upon research by Menter [1994], and refinements have been made to the model over the last several years. These refinements have improved the accuracy of the model and made it viable for use in a

wide range of turbulent flows [Wilcox 1998] [Menter 2003] [Wilcox 2008]. In terms of this model, k represents the turbulent kinetic energy in a flow, and ω represents the characteristic frequency for the turbulence [Jacobsen et al. 2012]. The equations governing the k - ω SST turbulence model take the form of advection-diffusion equations, and are shown as Equations 35 and 36.

$$\frac{\partial k}{\partial t} + \nabla[\mathbf{u}k] = \mathcal{P}_k - \beta^* k\omega + \nabla[(\mu + \sigma_k \mu_t)\nabla k] \quad [35]$$

$$\frac{\partial \omega}{\partial t} + \nabla[\mathbf{u}\omega] = \delta S^2 - \beta\omega^2 + \nabla[(\mu + \sigma_\omega \mu_t)\nabla \omega] + 2(1 - F_1) \frac{\sigma_{\omega 2}}{\omega} \nabla k(\nabla \omega)^T \quad [36]$$

Within Equation 36, the parameter represented by F_1 , is known as a blending factor that determines the strength of the final term in the equation. The value for F_1 varies between 0 and 1 and the equation for how F_1 is formulated is outlined in Equation 37. It is important to note that when F_1 is equal to 1, the last term in Equation 36 disappears, and a full formulation of the k and ω coefficients is being conducted following a k - ω turbulence model; however, when F_1 is equal to a value less than 1, but greater than 0, the k and ω coefficients are influenced by the final term in Equation 36 which causes the formulations of k and ω to be a “blend” between a k - ω turbulence model and a k - ϵ turbulence model. Lastly, when F_1 is equal to a 0, the full formulation of the k and ω coefficients is being conducted, following a k - ϵ turbulence model [Menter et al. 2003]. Within Equation 37, the y -variable determines the distance to the nearest wall, which greatly influences the proportions of the blending between the k - ω and k - ϵ turbulence models. An additional equation used for the determination of the parameter $CD_{k\omega}$, which was necessary to formulate values for the blending factor F_1 , is represented in Equation 38.

$$F_1 = \tanh \left\{ \left\{ \min \left[\max \left(\frac{\sqrt{k}}{\beta^* \omega y}, \frac{500\mu}{y^2 \omega}, \frac{4\rho \sigma_{\omega 2} k}{CD_{k\omega} y^2} \right) \right] \right\}^4 \right\} \quad [37]$$

$$CD_{k\omega} = \max(2\rho \sigma_{\omega 2} \nabla k(\nabla \omega)^T, 10^{-10}) \quad [38]$$

The expansion of the dynamic eddy viscosity, μ_t , is represented in Equation

39. It is important to recognize in Equation 39 that the parameter S is representative of the measure of the strain rate tensor (Equation 34), and that another blending factor F_2 is present, which is expanded further in Equation 40.

$$\mu_t = \frac{a_1 k}{\max(a_1 \omega, S F_2)} \quad [39]$$

$$F_2 = \tanh\left(\max\left[\frac{2\sqrt{k}}{\beta^* \omega y}, \frac{500\mu^2}{y^2 \omega}\right]\right) \quad [40]$$

All the constants needed within the $k-\omega$ SST turbulence model are blended based on research conducted by Wilcox [1988] and Mohammadi and Pironneau [1993]. Their research relates the value for the coefficients within the $k-\omega$ SST model to a function represented in Equation 41. The coefficients ϕ_1 and ϕ_2 , within Equation 41, are placeholder terms in which multiple different coefficients can take their place. The values for the coefficients that were used in this study are shown in Table 1.

$$\phi = \phi_1 F_1 + \phi_2 (1 - F_1) \quad [41]$$

Table 1: List of coefficients necessary for the completion of the $k-\omega$ SST model's governing equations

| Coefficient | Non-Dimensional Value |
|---------------------|-----------------------|
| a_1 | 0.31 |
| δ_1 | 0.5532 |
| δ_2 | 0.4403 |
| β^* | 0.09 |
| β_1 | 0.075 |
| β_2 | 0.0828 |
| σ_{k1} | 0.85 |
| σ_{k2} | 1 |
| $\sigma_{\omega 1}$ | 0.5 |
| $\sigma_{\omega 2}$ | 0.856 |

Lastly, the expansion of the production term \mathcal{P}_k is illustrated in Equation 42.

$$\mathcal{P}_k = \min (\mu_t(\nabla \times \mathbf{u})(\nabla \times \mathbf{u})^T, 10\beta^*k\omega) \quad [42]$$

The use of the production term avoids an issue recognized in an earlier form of the $k\text{-}\omega$ SST turbulence model, where turbulent energy was unnaturally extracted from flows being modeled in the surf zone [Mayer & Madsen 2000]. Without the inclusion of this parameter, OpenFOAM would find an increased amount of turbulence in its simulations when using the $k\text{-}\omega$ SST turbulence model.

3.4.2 Volume of Fluid Method

Another important concept exercised by the OpenFOAM software is the utilization of the volume of fluid (VOF) method. This method is used, in addition to the turbulence models, as a way for OpenFOAM to model the free surface as a fluid-fluid interface [Hirt & Nichols 1981].

As previously mentioned in Section 3.4.1.1, a surface tracking parameter, γ , was included within the RANS Equations (Equation 32). The concept behind this surface tracking parameter is the essence of the VOF method. Based upon the content of individual computational cells, the value for the surface tracking parameter, γ , will change; i.e. computational cells filled entirely with air make $\gamma = 0$, cells filled entirely with water make $\gamma = 1$, and cells with a mixture of both air and water cause γ to be equivalent to values between 0 and 1 based upon the proportions of air and water, by volume percentage, in the cell [Jacobsen et al. 2012] [Rusche 2003] [Hirt & Nichols 1981].

The variation of this surface tracking parameter must be accounted for by including another governing equation for RANS turbulence models, shown in Equation 43. It is important to know that the final term on the left hand side of the equation is known as an interface compression term, which reduces smearing of the air-water interface [Berberović et al. 2009] [Brunisma 2016]. This term is only effective in cells that contain a mixture of both air and water, i.e. $0 < \gamma < 1$, and is

also dependent upon the relative velocity, \mathbf{u}_r , of the fluid in each cell.

$$\frac{\partial \gamma}{\partial t} + \nabla \gamma \mathbf{u} + \nabla \gamma \mathbf{u}_r (1 - \gamma) = 0 \quad [43]$$

By using both Equation 43 and Equation 32 as the basis for the RANS turbulence models, and subsequently the $k-\omega$ SST turbulence model, an accurate simulation can be run for multi-phase fluid interfaces, most notably at the air-water interface on the free surface. The use of the VOF method has proven its ability to accommodate simulations that are: highly distorted, have multivalued free-surfaces, or simulations with topological changes such as wave breaking and recombination [Vyzikas et al. 2013][Greaves 2004]. Without the VOF method, a dynamic mesh of computational cells, which would follow the free-surface during wave propagation, would be necessary for an accurate simulation, which is a much more complex computation [Khalid 2016].

It is also important to mention some limitations that the VOF method has; in particular, when generating wave fields with high surface tension, the efficiency of the VOF method drops, and for waves with steepnesses greater than $s = \frac{H}{L} > 0.05$, the results become less accurate [Afshar 2010] [Khalid 2016].

3.4.3 Waves2Foam

Waves2Foam is an additional library/toolbox that can be compiled within the OpenFOAM software package. The primary use of this toolbox is to generate waves in OpenFOAM, while utilizing the VOF method coupled with RANS turbulence models to accurately model both propagating and breaking waves [Jacobsen 2017] [Jacobsen et al. 2012].

When utilizing the waves2Foam toolbox, it is common to use relaxation zones for both the wave inlet and wave outlet regions of the computational domain. These zones allow for a smooth generation of waves from their initial state into fully non-linear CFD solutions at the wave inlet, while at the same time avoiding wave reflections from the boundaries of the computational domain [Jacobsen et al. 2012].

The relaxation technique that is employed by the waves2Foam toolbox is an extension of research done by Mayer et al. [1998]; the technique is exercised within waves2Foam through a relaxation function denoted in Equation 44 [Jacobsen et al. 2012].

$$\varphi = \alpha_R \varphi_{computed} + (1 - \alpha_R) \varphi_{target} \quad [44]$$

The variable φ within the relaxation function can be defined by either the velocity field \mathbf{u} , or the VOF surface tracking field γ . On the other hand, the variation in the spatial weighting factor, $\alpha_R(\chi_R)$, is identical to the exponential weight distribution found in research by Fuhrman et al. [2006], which is expressed in Equation 45.

$$\alpha_R(\chi_R) = 1 - \frac{\exp(\chi_R^{3.5}) - 1}{\exp(1) - 1} \quad \text{for } \chi_R \in [0; 1] \quad [45]$$

The use of the relaxation function can be explained as the transition from a targeted value for the CFD computation, of either the velocity or surface tracking fields, to a fully computed output from OpenFOAM or vice versa; this transition is based on how α_R and χ_R vary in both the wave inlet and wave outlet regions [Fuhrman et al. 2006].

A visualization of what a common computational domain looks like when using the exponential spatial weighting factor in the waves2Foam toolbox is shown in Figure 3. This figure depicts both the wave inlet and wave outlet relaxation zones, how α_R and χ_R vary within them, and the region where fully non-linear computations are executed. It is important to note that relaxation zones of different shapes are capable of being modeled using the waves2Foam toolbox, including both cylindrical and semi-cylindrical orientations. However the rectangular shape illustrated in Figure 3 was used for this study.

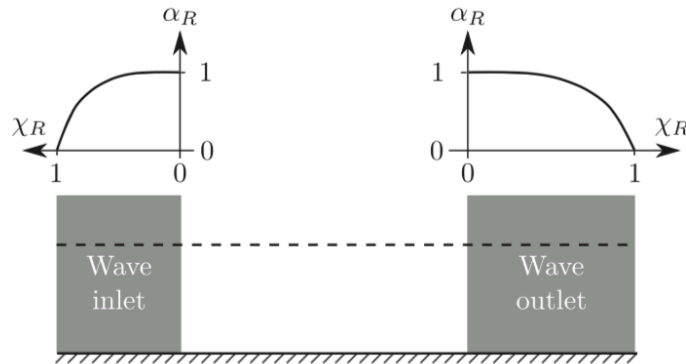


Figure 3: Sketch of the variation of $\alpha_R(\chi_R)$ for both inlet and outlet relaxation zones, as well as a general overview of how a common computational domain is constructed using the waves2Foam toolbox [Jacobsen et al. 2012]

In general, the lengths given to relaxation zones determine how efficient they are, i.e. the longer the relaxation zones, the more effective they are. However, by increasing the length of a relaxation zone, the computational cost of a simulation will also increase [Vyzikas et al. 2017]. This fact introduces a caveat, where an appropriate length for relaxation zones must be determined while at the same time trying to minimize computational costs. The relaxation scheme implemented for the purposes of this study is outlined in Section 4.3.2, detailing the length of each relaxation zone, as well as the discretization scheme employed within it.

3.5 Grid2Grid

In order to truly couple the HOS-NWT software with OpenFOAM, another software known as Grid2Grid had to be utilized. Grid2Grid is a post-processing software that re-structures the outputs of HOS-NWT in a programming language, which is readable by OpenFOAM and other software [Choi et al. 2017].

The capabilities of the Grid2Grid software have been shown and validated within the manual for Grid2Grid [Choi et al. 2017]. One study in particular focused on waves representing the 1000-year return period in the Gulf of Mexico. In this study, waves were generated in physical wave tank experiments [Choi et al. 2017], and the HOS method was then used to model the same sea-state from the

experiments. The results showed good agreement between the outputs of both HOS and OpenFOAM simulations with the physical experiments, indicating that the nonlinear phenomena expected within waves with 1000-year return periods were properly simulated by the HOS method and transferred to OpenFOAM using Grid2Grid [Choi et al. 2017].

The validations conducted by this research, along with others that have been cited previously, indicate that for the purposes of the current study, the use of the Grid2Grid software would provide a dependable way of preparing the outputs of HOS-NWT for use within the OpenFOAM software.

4. Methodology:

4.1 HOS-NWT

4.1.1 Benchmarking:

After compiling the source code for the HOS-NWT model, several tutorials could be found as “Benchmark” scenarios in order for the user to become acclimated with the HOS-NWT model. Five different Benchmarking procedures were available within the source code of the model, which included both regular and irregular wave conditions in both 2 and 3 dimensions, as well as a Sloshing case. Each of these Benchmark scenarios were run to validate the capabilities of HOS-NWT and prepare for the implementation of the model to the data from the MARINTEK facility.

The wave data that was acquired from MARINTEK consisted of a time series of surface elevations. As mentioned previously, the surface elevation data involved long crested waves; because of this, an assumption could be made that the HOS-NWT model only needed to be run for a two dimensional case. Due to this simplification, special attention was given to the Benchmarking scenarios where 2D conditions were implemented. Figures 4 and 5 represent the Benchmarking scenarios for 2D Regular and 2D Irregular wave conditions, respectively. Each figure shows great agreement between the reference data and the results from HOS-NWT.

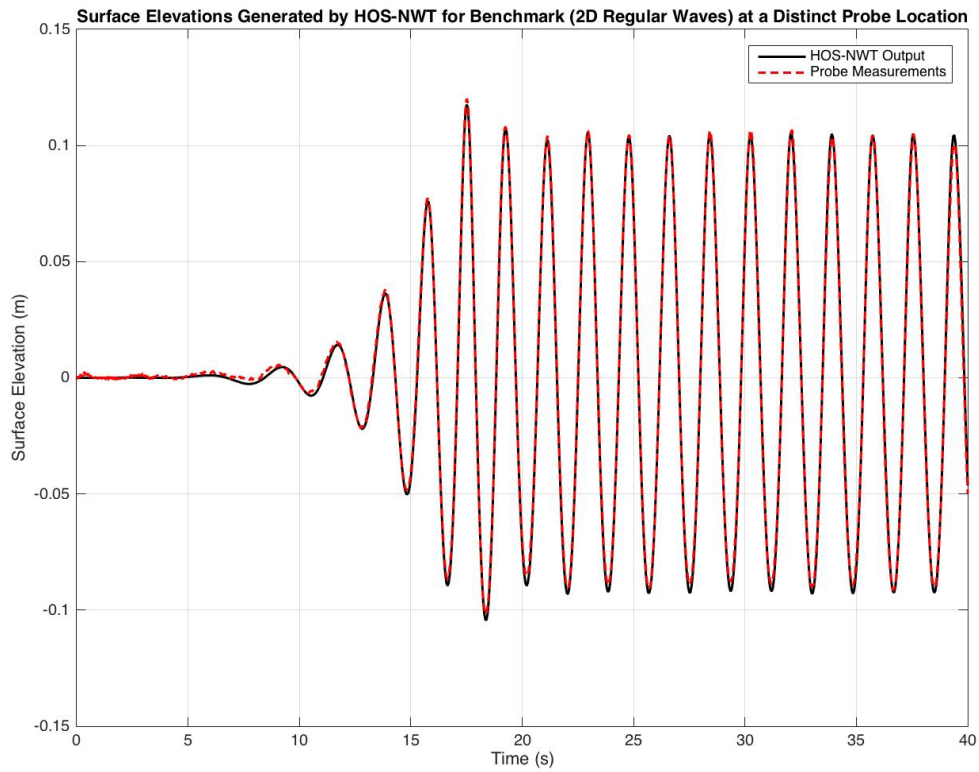


Figure 4: 2D Regular Wave Benchmark Result showing very close agreement between the experimental data and the HOS-NWT output

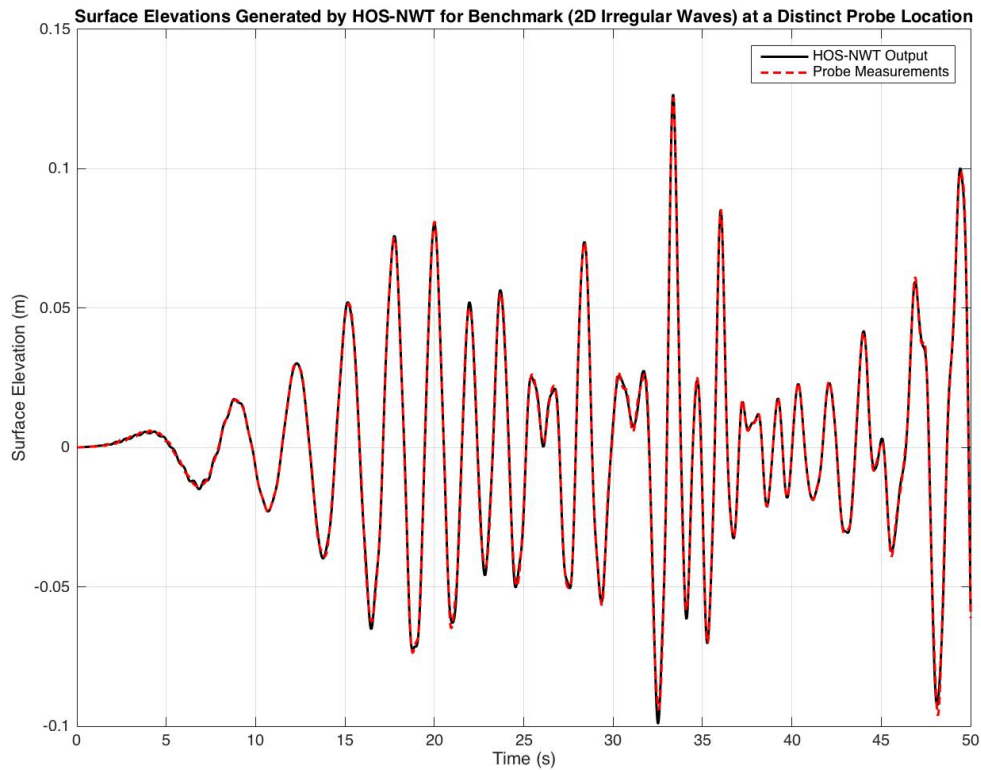


Figure 5: 2D Irregular Wave Benchmark Result showing very close agreement between the experimental data and the HOS-NWT output

After running each of the Benchmark conditions, a clear understanding of the process of how to initialize the inputs for running the HOS-NWT numerical model was gained. With this knowledge, it was then possible to implement the numerical model using the data from the MARINTEK facility.

4.1.2 HOS-NWT Setup

A general understanding of the necessary steps that needed to be taken to initialize HOS-NWT simulations was gained through the completion of the Benchmark tutorials. Prior to running HOS-NWT, a file containing all of the necessary information regarding the inputs to the model had to be tailored to the parameters that explained the conditions present at MARINTEK. A snapshot of the contents of the input file is represented in Figure 6.

```

----- Tank dimensions -----
Length(m) of the wavetank  :: xlen          :: 30.0d0
Beam(m) of the wavetank   :: ylen          :: 80.0d0
Depth(m) of the wavetank  :: h             :: 6.0d0
----- Select case -----
Choice of computed case   :: icase         :: 3
----- Sloshing case (icase = 1) -----
Number of the natural mode :: islosh        :: 3
Amplitude (m) of the mode  :: aslosh        :: 0.2d0
----- Monochromatic case (icase = 2) -----
Amplitude (m) of wave train :: amp_mono      :: 0.1d0
Frequency (Hz) of wave train :: nu_mono       :: 0.5588d0
Angle (deg) from x-axis    :: theta_mono    :: 0.d0
Phasis (rad) of wave train  :: ph_mono       :: 0.d0
Directional wmk type       :: ibat          :: 2
Wave target distance (ibat=3):: xd_mono       :: 18.d0
----- File case (icase = 3) -----
Name of frequency file     :: file_name     :: Hs0.245_Tp1.82
Frequency cut-off          :: i_cut         :: 0
Low cut_off frequency (Hz) :: nuc_low       :: 0.0d0
High cut_off frequency (Hz) :: nuc_high      :: 10.0d0
----- Irregular wave (icase=4) -----
Significant wave height (m) :: Hs            :: 0.05d0
Peak period (s)            :: Tp            :: 1.d0
Shape factor (Jonswap)     :: gamma         :: 3.3d0
Seed number for random numb. :: izeed        :: 513
----- Wavemaker definition -----
Nonlinear order of wavemaker :: i_wmk        :: 2
Type (1: piston, 2: hinged) :: igeom        :: 2
Rotation axis distance     :: d_hinge      :: 4.98d0
Time ramp                  :: iramp        :: 1
Time ramp duration (s)     :: Tramp        :: 12.0d0
----- Numerical beach -----
Absorption numerical beach  :: iabsnb       :: 1
Beginning front num. beach  :: xabsf        :: 0.8d0
Absorption strength front   :: coeffabsf    :: 0.95d0
----- Elevation/Velocity-Pressure probes -----
Use of probes              :: iprobes      :: 1
Filename of probe positions :: pro_file     :: prob.inp
----- Time-integration -----
Duration of the simulation  :: T_stop       :: 1300.0
Time tolerance: RK 4(5)    :: toler        :: 1.e-4
Output frequency           :: f_out        :: 10.0d0
----- Output -----
Output: 1-dim. ; 0-nondim.  :: idim         :: 1
free surface plot          :: i3d          :: 0
modes plot                 :: imodes       :: 0
wavemaker motion plot     :: iwmk         :: 0
Swense output 1='yes',0='no' :: i_sw         :: 1
  
```

Figure 6: Representation of the input file utilized fro running the HOS-NWT model throughout the course of this study

First and foremost, right at the beginning of the input file, the dimensions of the wave tank had to be defined to allow for the propagation of waves over a region where the numerical simulation from HOS-NWT could be compared with the experimental data from MARINTEK. The dimensions of the tank included a water depth of 6 meters, a length of 30 meters, and a breadth of 80 meters, which was overlooked by the software due to the two dimensional nature of the model runs. After defining the domain, a number of different cases could be selected based upon what kind of waves were being modeled using the software. These cases included a Sloshing Case, Monochromatic Case, File Case, and Irregular Wave Case; for the purposes of this study, a File Case was selected where data defining the waves measured during experimentation was compiled within a file with the name shown in Figure 6.

The contents of the file, necessary for the initialization of the HOS-NWT model, represented the frequency descriptions of linear wave components being generated by the motion of the wave paddle [Ducrozet et al. 2012]. These descriptions could be found by multiplying the wave paddle motion by an appropriate transfer function to determine the time series of free surface elevation at the paddle; then implementing an FFT to collect the frequency, amplitude, and phase of each wave component. However, in this study, the paddle location was shifted to the WAVE3 wave gauge located 5 meters upstream from the location of interest, and 20 meters downstream from the physical paddle. This was due to the fact there was an inability to obtain the transfer function for the paddle. The surface elevations at the WAVE3 gauge could be transformed into the frequency domain without the implementation of a transfer function, and then used as inputs to the HOS-NWT model. The frequency description of the waves at the WAVE3 gauge, obtained from the implementation of an FFT, is shown in Figure 7 along with the JONSWAP spectrum that characterized the experimental sea-state, where $H_s = 0.245$ m and $T_p = 1.82$ s. The extraction of the amplitude and phase of each frequency component from the FFT analysis was used to create the file, for the proper case, to run the HOS-NWT code.

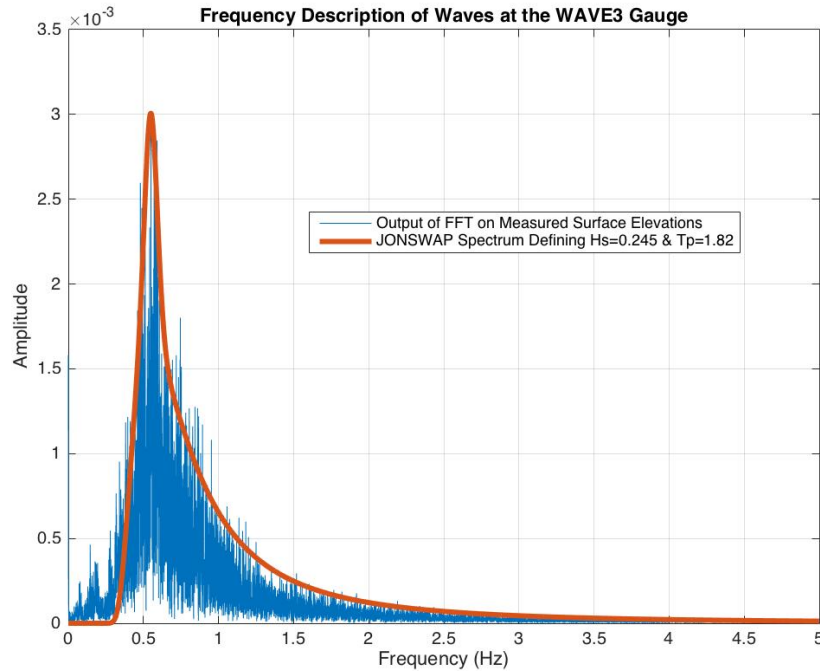


Figure 7: Comparison between the frequency content of the waves at the WAVE3 gauge and the JONSWAP Spectrum defining the sea-state

After selecting the proper case required for wave generation, definitions of the properties of the wavemaker were inserted into the input file. Properties included the non-linearity order of the wavemaker, the type of wavemaker, the rotation axis distance, and whether or not a time ramp was to be used in the numerical simulation. These parameters were complemented by an additional file describing the configuration of the wave maker, where crucial parameters were set, with some redundancies, such as: the type of wave maker (for this study, a single-hinged paddle was used), the clock rate of the wavemaker motion, the water depth of the numerical wave tank, and the distance of the rotation axis of the wavemaker from the free surface. The rotation axis distance is representative of the distance from the still water elevation in which the hinge for a single-hinged wave maker is located. A schematic showing the physical description of the wave maker used in this study is shown in Figure 8.

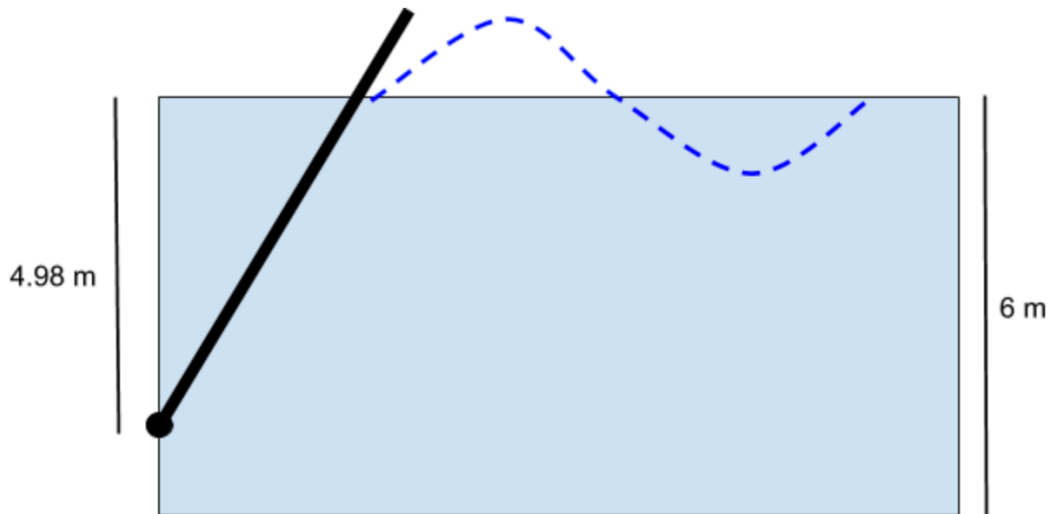


Figure 8: 2D Schematic showing the orientation of the single-hinged wave maker used for wave generation, where the water depth is 6 m and the rotation axis distance from the still water surface is 4.98 m

The last few sections within the input file related primarily towards the configuration of the outputs that could be generated by the HOS-NWT model. The section labeled Elevation/Velocity-Pressure Probes, in Figure 6, coupled with an additional file, titled *prob.inp*, allowed the HOS-NWT model to export simulated surface elevations, as well as velocity and pressure data from probes projected at specific locations in the computational domain. For the purposes of this study, probes were generated at the locations of the 23 wave gauges so that analyses could be conducted on the results from the HOS-NWT model with appropriate reference data from the model tests.

The Time-integration section of the input file follows the section where the probe locations are determined. This part of the file is where the duration of the entire simulation is defined, the time tolerance is determined based on the Runge-Kutta Scheme, as outlined in Section 3.1.1, and the frequency at which the outputs of the HOS-NWT model will be reported. The reporting of output parameters was chosen to occur at a frequency of 10 Hz; therefore, data recorded by the numerical

wave probes was reported every 0.1 seconds, as well as data from additional output measures that could be selected in the final section of the input file.

Based on section titled Outputs, depicted in Figure 6, it can be seen that outputs with dimensional properties were chosen, and only the SWENSE Output was selected for the purposes of this study. The SWENSE (Spectral Wave Explicit Navier-Stokes Equations) approach is a method used for studying wave-body interactions using viscous flow theory [Luquet et al. 2007]. The outputs from this approach were necessary in this study in order to couple the HOS-NWT model with OpenFOAM. Without the SWENSE data, not enough information about the sea-surface processes modeled by HOS-NWT would be available to properly model simulations within OpenFOAM.

After defining all of the necessary parameters in the input file in Figure 6, and acquiring the additional files related to the frequency descriptions of linear wave components, the configuration of the wavemaker, and the location of each probe in the wave gauge array, the HOS-NWT model was prepared to be run.

4.2 Wave Breaking Criteria

The application of the four breaking criteria, outlined in earlier in this report (Sub-Sections 3.3.1, 3.3.2, and 3.3.3), were applied to the outputs of the HOS-NWT model for each of the 23 wave gauges in the array. While the objective of this study was to identify extreme and breaking wave events at the 12th wave gauge, time was invested to see if the process of breaking was taking place at the 12th wave gauge, even if breaking onset had occurred before reaching it.

In addition to the experimental data, 8 high-speed video clips were provided to visualize instances of breaking waves over the array of wave gauges. This proved to be a very valuable tool in assessing whether breaking events were correctly measured by each of the different criteria at the times shown in each video.

Each of the four breaking criteria were analyzed individually for accuracy, and then compared with one another in an effort to come to a conclusion on which was most suitable to select breaking events to be modeled using OpenFOAM.

4.3 OpenFOAM:

After reaching a conclusion on the most suitable breaking criterion, different breaking events identified by that criterion were selected, in space and time, and were modeled using OpenFOAM. In order to accomplish this, numerous steps were taken to couple the HOS-NWT model with OpenFOAM. This effort was undertaken to give the option of simulating particular events in a CFD domain where breaking could be modeled and analyzed, without the constraint of the potential flow assumptions within the HOS-NWT model.

Initially, the outputs of the HOS-NWT model had to be prepared for use within OpenFOAM. This was undertaken by applying the Grid2Grid software to the SWENSE output file. However, prior to utilizing the software, modifications were made to the dictionaries within Grid2Grid's code to allow for the creation of grids with suitable discretization schemes, in addition to selecting proper locations and times from the HOS-NWT outputs where breaking events were identified. As previously mentioned in Section 3.5, Grid2Grid is a post-processing software that re-structures the outputs of HOS-NWT in a programming language that is readable by OpenFOAM [Choi et al. 2017]. The Grid2Grid software generates HOS wave fields of wave elevation time series, prepped for 3D visualization; the outputs of the Grid2Grid software come in the form of Visualization Toolkit (VTK) file formats, that are compatible with ParaView, the visualization software OpenFOAM utilizes. After acquiring the VTK files, they must be inserted, along with the SWENSE output file, into a case folder in the Waves2Foam toolbox where the linkage between OpenFOAM and HOS-NWT can be executed.

The contents of the case folder, for the model runs conducted in this study, had several files and directories that adhered to procedures that would ensure OpenFOAM ran properly. Instead of arduously explaining the purpose and structure of each file/directory, the following sections (4.3.1-4.3.3) are geared toward the description of the main components of the model's structure, that exist due to the presence of each file/directory in the case.

4.3.1 Computational Mesh

The format of the computational mesh, used for the OpenFOAM simulations in this study, was determined based on some of the parameters that were set within the Grid2Grid software. The parameters that influenced the computational mesh schematic were the dimensions of the computational domain, as well as the discretization schemes selected for the x and z directions. Due to the fact that this study focused on long crested 2D waves, the computational cells within the mesh were not discretized in the y-direction.

In order to reduce the computational time necessary for the simulation of different breaking wave events, the computational domain was selected so that it would focus primarily on the array of 23 wave gauges that covered a range of 3.3 meters in the x-direction. In addition to having the computational mesh cover that range, it was determined that additional space was to be included on either side of the array to allow for the proper growth and decay of wave heights both entering and exiting the domain through specified relaxation zones (See Section 4.3.2); overall, a distance of 15 meters in the x-direction was chosen.

In terms of the configuration of the computational mesh in the z-direction, it was important to include room for both the air and water phases needed within the OpenFOAM simulation. Referring back to Section 4.1.2, a water depth of 6 meters had to be included within the computational mesh. In addition to this, due to the fact that the wave climates involved in this study possessed significant wave heights of 0.245 m, an additional meter was included within the computational mesh, above the mean water level. With this additional space, the profile of every wave from the HOS-NWT simulation would be able to propagate within an OpenFOAM simulation, with ample room for air-sea interactions to take place. In total, the computational mesh covered 7 meters in the z-direction.

Ten centimeters (0.1 m) of space within the computational mesh was allotted in the y-direction, even though 2D simulations were the focus of this study. This is due to the fact that OpenFOAM is designed for 3-dimensional space, and defines all meshes as such. However, 2-dimensional problems can be simulated in OpenFOAM

by generating meshes in 3 dimensions and applying special boundary conditions in different locations within the mesh [Greenshields 2018], explained further in Section 4.3.3.

Overall, the dimensions of the entirety of the computational mesh were, $15\text{m} \times 0.1\text{m} \times 7\text{m}$, in the x , y , and z directions, respectively. Different discretization schemes were employed in each direction, for the full extent of the computational domain, thus reducing every cell into identical 3-dimensional cubes. In the x -direction, it was determined that a total of 500 computational cells would be sufficiently fine enough to visualize the breaking process clearly. For the 7 meters in the z -direction, the computational mesh was discretized into 350 cells. Lastly, as mentioned previously, the computational cells within the mesh were not discretized in the y -direction, meaning a single cell was selected to complete the mesh in the y -direction. By using these discretization schemes, each cell within the computational mesh had the dimensions of $2\text{cm} \times 10\text{cm} \times 2\text{cm}$, in the x , y , and z directions, respectively; Figure 9 depicts a single computational cell from the mesh, with its dimensions labeled, and Figure 10 shows the fully discretized computational domain created within OpenFOAM.

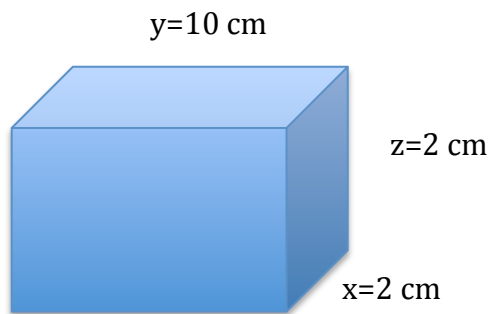


Figure 9: Single computational cell with each of its dimensions labeled for the x , y , and z directions



Figure 10: Full computational mesh, having dimensions of $15\text{m} \times 0.1\text{m} \times 7\text{m}$, in the x, y, and z directions, constructed using the computational cells illustrated in Figure 9

It would have been beneficial to implement different regions within the computational mesh where different discretization schemes could be employed. In this case each region would possess computational cells with varying size, depending on the proximity of that region to where breaking events were expected to occur. In other words, regions where breaking was expected could have had much finer computational cells as to allow for a clearer visualization of the breaking process. However, in order to implement this type of discretization process, significant modifications to the source code of the Grid2Grid software would have been required. Future work could be associated with making these modifications, which in theory, would allow for clearer visualizations of the breaking process and more efficient model runs.

4.3.2 Relaxation Zones

The computational mesh, outlined in the previous section, contained two separate relaxation zones as described in Section 3.4.3. The wave inlet relaxation zone allowed for the smooth generation of waves at the wave inlet that would grow

to match the content of the output of the HOS-NWT model after exiting the inlet relaxation zone. At the same time, the wave outlet relaxation zone induced a procedure where the free surface process would “relax”, or ease its way to reach a state where waves would cease to propagate, thus eliminating reflections from impacting the main computational domain.

As previously discussed, the size of a relaxation zone is directly proportional to its effectiveness. The relaxation zones for the wave inlet and outlet were chosen to be sufficiently large enough to execute their duties effectively, while at the same time being sufficiently small enough to avoid excessive levels of computational effort. In research conducted by Liu et al. [2019], a recommendation was given that relaxation zones should typically be as long as one to two wavelengths of the waves that are being modeled. The peak period of the waves being studied in this thesis was equal to 1.82 seconds, corresponding to a wavelength of approximately 5 meters using linear wave theory approximations for deep-water waves, i.e. $L = \frac{gT^2}{2\pi}$. Unfortunately, due to the position of the WAVE3 Gauge, mentioned in Section 4.1.2, only 3.35 meters upstream of the wave gauge array were viable to be used as the wave inlet relaxation zone; whereas, a full 5 meters were allotted for the wave outlet relaxation zone downstream of the wave gauge array.

4.3.3 Boundary Conditions

Since the computational mesh, used for the OpenFOAM simulations, was constructed in the shape of a rectangular prism, each of the six faces on the rectangle required boundary conditions to be set.

The face at the base of the computational mesh, normal to the $-z$ direction, was chosen to have a *wall* type boundary that would mimic the bottom of a physical wave tank. The faces normal to the y and $-y$ directions were given a special type of boundary condition called an *empty* boundary condition; this *empty* condition instructs the OpenFOAM software that the planes that are normal to the faces (y and $-y$) do not require a solution [Greenshields 2018], effectively simplifying the computational domain into two dimensions. The remaining three faces normal to

the x , $-x$, and z directions were all given the same *patch* boundary type. The *patch* designation was given to each of the remaining boundary faces of the computational domain due to the fact that each face is representative of either an inlet or outlet region, which is standard procedure when using OpenFOAM. It is self explanatory that the wave inlet and outlet faces, normal to the x and $-x$ directions, respectively, are *patch* regions; on the other hand, the region normal to the z -direction can be thought of as a boundary face representing the open atmosphere, where the free flow of air through that boundary face, either into or out of the computational domain, is necessary for accurate simulations.

5. Results & Discussion:

5.1 HOS-NWT Output:

First and foremost, the HOS-NWT model was used to replicate one of the experiments conducted at the MARINTEK facility, which lasted for 1300 s. It is important to remember that the experimental data from this experiment corresponded to a sea-state with relatively high steepness, leading to high levels of nonlinearity in the waves that needed to be generated by the model. Because of this fact, the HOS nonlinearity order M , mentioned in the Section 3.1.1, was set to a value of 8 so that a fully non-linear computation of the sea surface properties could be simulated using the HOS-NWT model.

In Figure 11, a plot shows the initial state of the model, 0-50 seconds, along with the reference data at the projected location of the wave maker, the WAVE3 gauge. There is good agreement between the numerical simulation and the experimental data, with only slight differences in some of the crests and troughs of different wave events.

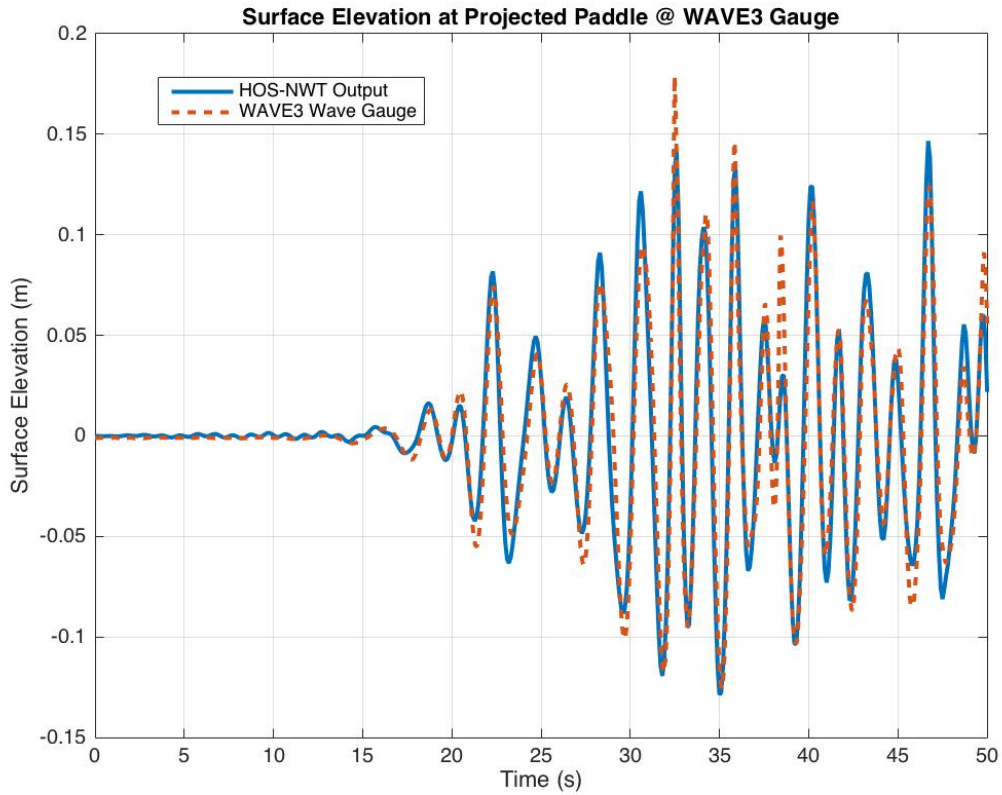


Figure 11: Surface elevations from the HOS-NWT model and the experimental measurements at the WAVE3 gauge/projected wave maker location for the initial 50 seconds of the simulation

Five meters further away, at the location of Wave Gauge 12, good agreement between the HOS-NWT output and the MARINTEK experimental data can be seen over the same time frame. A representation of this window in time is shown in Figure 12.

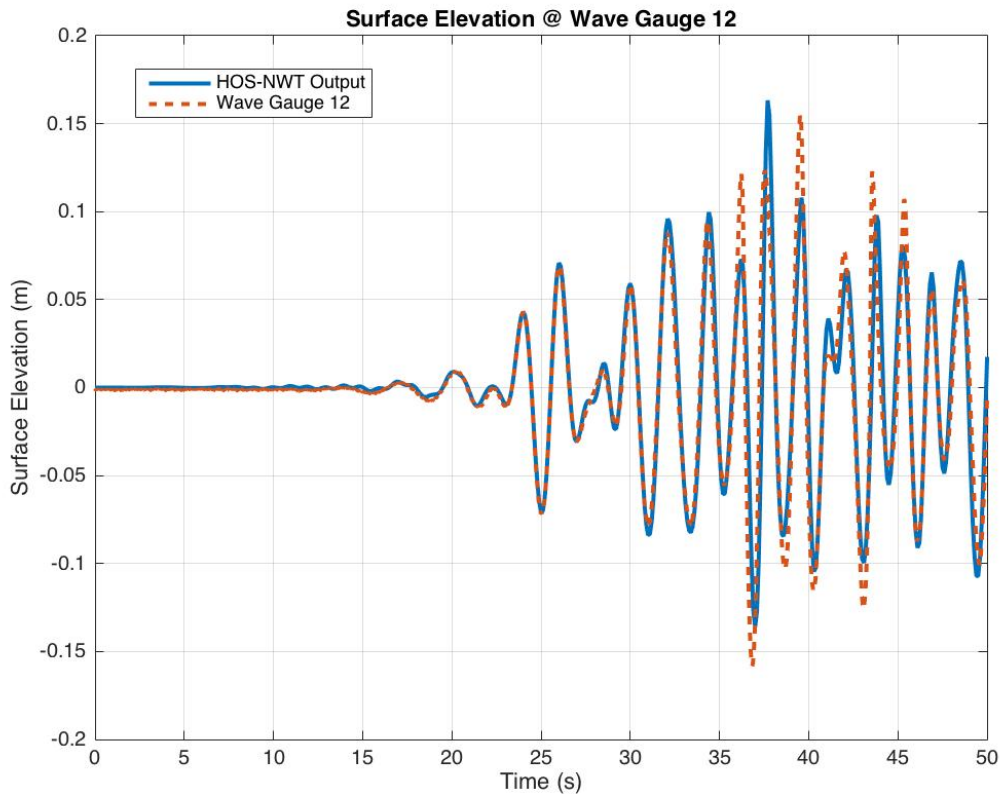


Figure 12: Surface elevations from the HOS-NWT model and the experimental measurements by Wave Gauge 12 at MARINTEK for the initial 50 seconds of the simulation

The agreement between the numerical simulation and the experimental data, at the initial stage of the model, boded well for the simulation of a numerical sea-state matching that of the MARINTEK experiment over a long period of time.

A window in time representing the waves being generated by the model much later in the simulation, between 910 and 970 seconds, was used to show the state of the model after a significant amount of time had passed. Figure 13 shows that the generation of waves at the WAVE3 gauge maintained a similar level of agreement as was shown earlier in Figure 11. This agreement also translated well to Wave Gauge 12, which is illustrated in Figure 14.

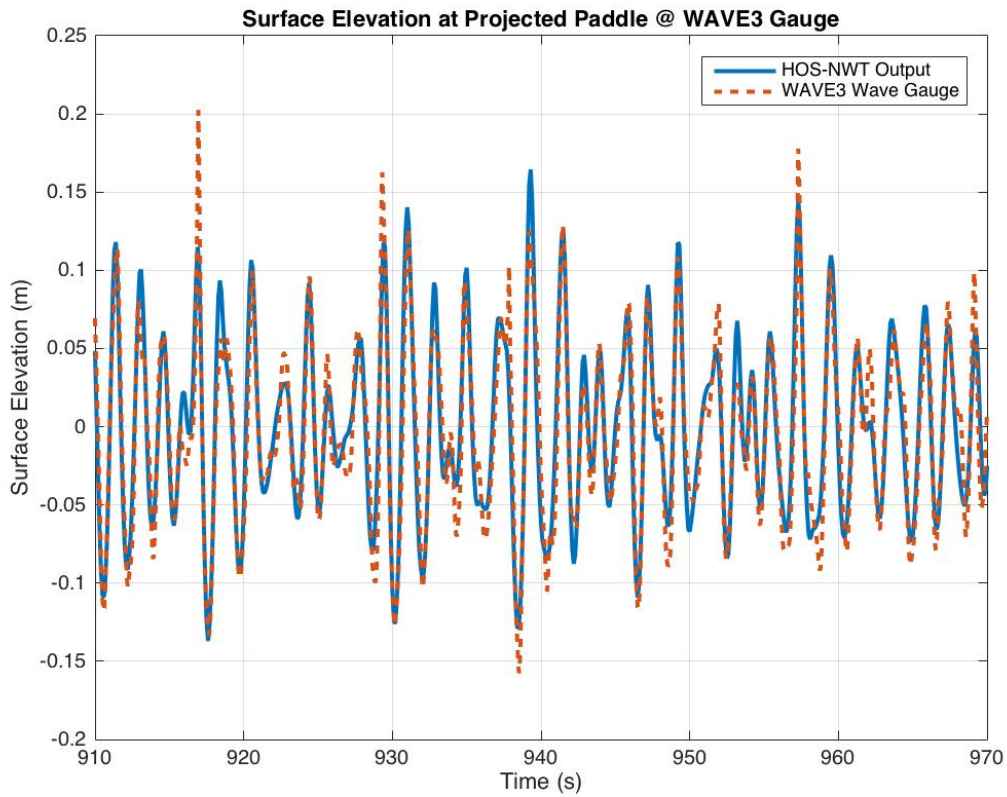


Figure 13: Surface elevations from the HOS-NWT model and the experimental measurements at the WAVE3 gauge/projected wave maker location for the time frame of 910-970s seconds

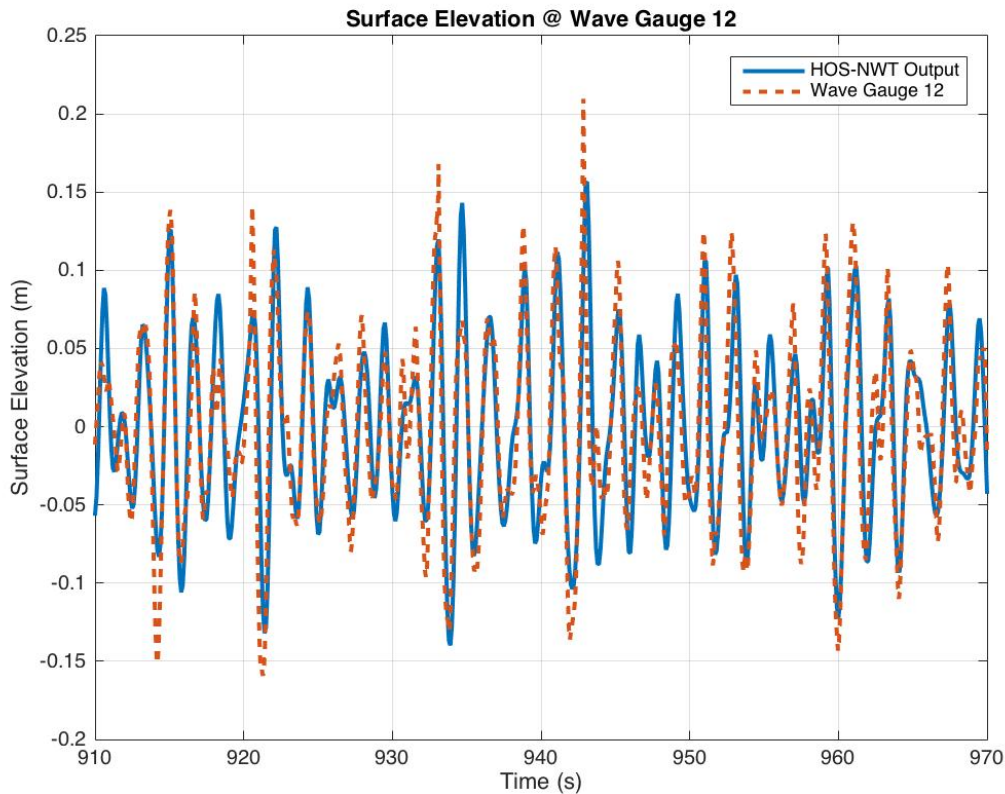


Figure 14: Surface elevations from the HOS-NWT model and the experimental measurements at Wave Gauge 12 for the time frame of 910-970 seconds

A check was conducted to see the level of agreement between the simulated and measured significant wave heights, at both the WAVE3 Gauge and Wave Gauge 12. The significant wave height of each surface process was found in a three-step process. Firstly, the variance of each sea surface process was found, after that the standard deviation of each time series was calculated, and then, after multiplying by 4, each significant wave height was formulated. The resulting values for each significant wave height are outlined in Table 2. The values show that there is a slight underestimation of the significant wave height on behalf of the surface process generated by the HOS-NWT model at Wave Gauge 12, leading to an error of approximately 2.2%. On the other hand, at the location of the WAVE3 gauge, the HOS-NWT model was in exact agreement with the significant wave height from experimentation for that location.

Table 2: Calculated Significant Wave Heights based on measurements by the MARINTEK wave gauges and results from the HOS-NWT simulation

| WAVE3 Gauge | | Wave Gauge 12 | |
|-------------|----------|---------------|----------|
| Experiments | HOS-NWT | Experiments | HOS-NWT |
| 0.2395 m | 0.2395 m | 0.2380 m | 0.2326 m |

The small level of error for the simulated significant wave height at Wave Gauge 12 can be associated with the level of steepness of the waves in the simulation, among other factors. Although the computation executed by the HOS-NWT model was fully non-linear, other studies utilizing the same model have found errors in sea-states with high levels of steepness. The work done by Bonnefoy et al. [2010] showed that while the HOS-NWT model has the capability of computing a fully non-linear sea surface with steepness levels of $\epsilon_c = 3\%$, where $\epsilon_c = \frac{H_s}{T_p} * 100\%$, similar variations between the computed free surface and experimental measurements were experienced. Following the methodology of Bonnefoy et al. [2010], the percentage of steepness associated with the experimental data from MARINTEK, $\epsilon_c = 13.46\%$, is quite large in comparison to their work. At the 12th Wave Gauge, an error of 2.2% between the HOS-NWT output and the experimental data from MARINTEK can be, to some extent, attributed to this high level of steepness among other factors, such as the limitations of the model due to its potential flow assumptions.

To visualize the impact that the wave steepness had on the simulation error of significant wave heights at Wave Gauge 12, another model test from MARINTEK was simulated, this time, with a lower level of steepness. At the 12th Wave Gauge, the measured significant wave height 0.2853 m, corresponding to a steepness level of $\epsilon_c = 11.64\%$, considering the fact that the peak period, T_p , was 2.45 s. The HOS-NWT model was able to generate a simulation with a significant wave height of 0.2808 m at Wave Gauge 12, leading to an error of 1.6%. Although the steepness associated with the second model test was lower than that of the initial model test, a steepness level of $\epsilon_c = 11.64\%$ is quite high in comparison to the $\epsilon_c = 3\%$ seen in

research from Bonnefoy et al. [2010]. If more experimental data from MARINTEK was available for several model tests with lower levels of wave steepness, a proper sensitivity study could have been undertaken to see how the accuracy of the HOS simulations is affected by wave steepness.

The result of a lower level of error with a lower level of steepness suggests that high levels of steepness could make it more difficult for the HOS-NWT model to mirror exactly what was measured during experimentation. However, it is important to note that the HOS-NWT model still managed to simulate results with relatively small levels of error, under these conditions.

5.2 Extreme Wave Validation:

After recognizing that the sea-state simulated using the HOS-NWT model showed good agreement with what was seen experimentally, the simulated waves were analyzed further. Firstly, an assessment was conducted to see how well the largest waves that were measured experimentally, at Wave Gauge 12, aligned with what was numerically modeled. There was only one wave that met the requirements of being a Rogue wave, equaling at least 2 times that of the significant wave height measured over the course of 1300 seconds of experimental data. Due to this small sample size, waves that were measured to be equal to or larger than 1.5 times the measured significant wave height at Wave Gauge 12 were used for this analysis. There were a total of 10 waves that met this requirement, including the true rogue wave event; the information regarding the points in time in which the crest of each wave occurred, as well as their respective wave heights are shown in Table 3, alongside the wave heights that were numerically generated using the HOS-NWT model. The level of steepness each individual wave possessed, which was found by taking the product of the amplitude of the individual waves and their respective wave numbers, was also included in Table 3 along with the error between the experimental data from the MARINTEK facility and the output of the HOS-NWT simulation. It is important to note that the extreme events at 260.1 and 857.9 seconds both aligned with a breaking wave events that were observed on

high-speed video; breaking waves go beyond the capabilities of the HOS-NWT model, therefore some level of error was expected for each of these events.

Table 3: Time stamps of extreme wave events having wave heights at least 1.5 times that of the significant wave height of the experimental data at the 12th Wave Gauge; the highlighted event represents the only true rogue event within the data

| Time (s) | Experimental Wave Height (m) | HOS-NWT Modeled Wave Height (m) | Experimental Steepness (ak) | Percent Error (%) |
|----------|------------------------------|---------------------------------|-----------------------------|-------------------|
| 207.7 | 0.3653 | 0.3257 | 0.2197 | 10.84 |
| 260.1 | 0.4759 | 0.3768 | 0.2570 | 20.82 |
| 318.9 | 0.4214 | 0.3104 | 0.4366 | 26.34 |
| 582.3 | 0.3853 | 0.3567 | 0.2598 | 7.42 |
| 686.9 | 0.3954 | 0.3255 | 0.3235 | 17.68 |
| 857.9 | 0.3715 | 0.3386 | 0.3177 | 8.85 |
| 1078.4 | 0.3914 | 0.3176 | 0.2856 | 18.85 |
| 1156.8 | 0.3687 | 0.3660 | 0.2867 | 0.74 |
| 1182.2 | 0.3831 | 0.3985 | 0.2061 | 3.88 |
| 1299.0 | 0.4009 | 0.3111 | 0.2348 | 28.85 |

The resulting differences between the experimental and numerically modeled extreme wave events, in Table 3, had an average error of about 14.42%. More often than not, there was an underestimation of the wave heights by the HOS-NWT simulation with one exception for the extreme event at 1182.2 seconds. The suspected cause of the experienced level of error was the steepness of each individual wave, which was included in Table 3. A plot was generated, illustrated in Figure 15, showing the relation between the steepness of each of the individual extreme wave events and the amount of error between the experimental data and the numerical simulation. A slight trend can be seen that for lower levels of wave steepness, the relative error between the HOS-NWT output and the measured data

was less than the extreme wave events with an increased amount of steepness. Figure 15 shows that the amount of error grew up to levels of about 30% for events with high steepness, and a linear trend line drawn through the data shows a slight upward slope indicating that, in general, events with higher steepnesses yielded more error. While there isn't an exact correlation between the value of steepness and the measured level of error, if more waves had exceeded the threshold of being 1.5 times that of the significant wave height of the surface process, more data points would have allowed for a better visualization of a trend.

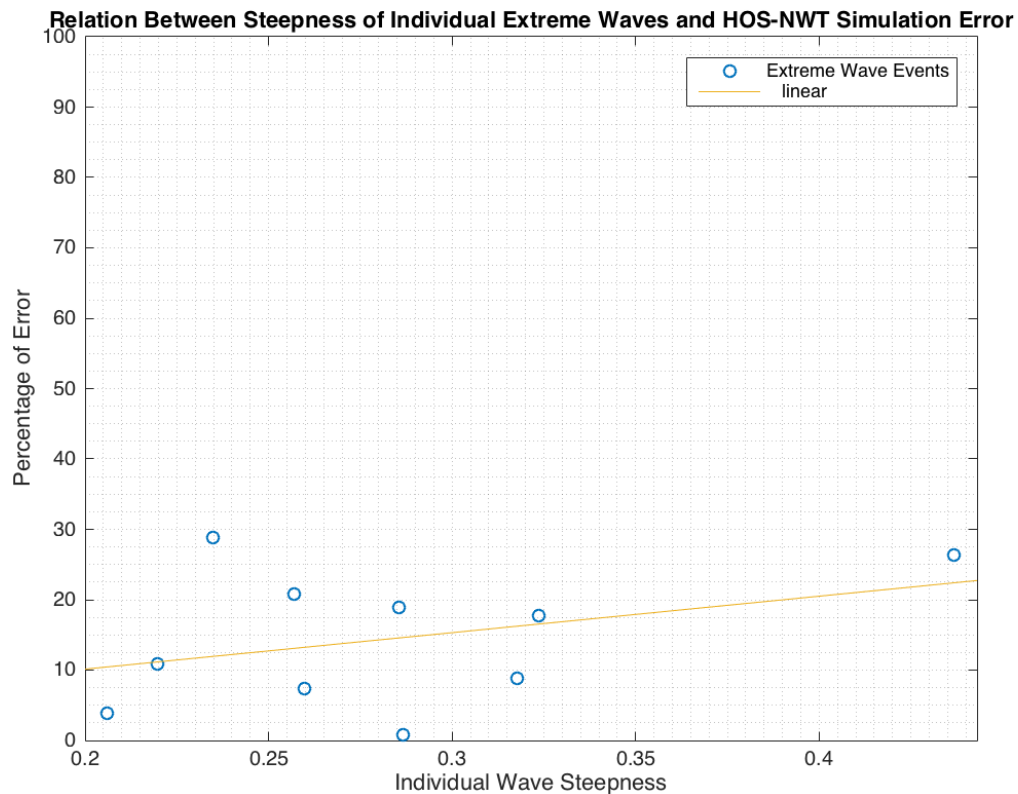


Figure 15: Plot depicting the relation of the individual wave steepness (ak) of extreme wave events and the error calculated between the experimental data and the HOS-NWT simulation results for model run with steepness $\epsilon_c = 13.46\%$

Similar to the analysis that was executed for the overall significant wave height of the simulated sea-surface process, another model test from MARINTEK with a lower level of steepness was employed to see if extreme events would be mapped more accurately in a sea-state with a lower overall level of steepness. The same methodology of using events having a wave 1.5 times that of the significant wave height at the 12th Wave Gauge was utilized and yielded a total of 10 events, with no true rogue events equaling at least 2 times that of H_s at the 12th Wave Gauge. Table 4, in the exact same way as Table 3, represents all of the extreme wave events that met the aforementioned criteria for the model run with a lower level of steepness equal to $\epsilon_c = \frac{H_s}{T_p} * 100\% = 11.64\%$. Additionally, Figure 16 shows the relation of the individual wave steepness for each event and the amount of error between the experimental and simulated results. It is important to note that for the model run with lower overall steepness, none of the extreme wave events corresponded to breaking wave events.

As was the case for the model run with a steepness of $\epsilon_c = 13.46\%$, a slight trend is mapped with a linearly fitted line showing that waves with higher individual steepness levels tended to generate larger errors. Overall, the average amount of error for the extreme wave events for this model run was 12.7%, down from 14.42% in the model run with a higher level of steepness. Although the difference in the resulting levels of error is minimal (1.72%), the result showing a lower level of error with a lower level of steepness for individual extreme wave events is similar to the trend seen for the results for modeled significant wave heights as discussed in Section 5.1.

Table 4: Time stamps of large wave events having wave heights at least 1.5 times that of the significant wave height of the experimental data at the 12th Wave Gauge for the model run with lower steepness

| Time (s) | Experimental Wave Height (m) | HOS-NWT Modeled Wave Height (m) | Experimental Steepness (ak) | Percent Error (%) |
|----------|------------------------------|---------------------------------|-----------------------------|-------------------|
| 330.0 | 0.5458 | 0.4626 | 0.3498 | 17.99 |
| 380.6 | 0.4724 | 0.3761 | 0.3104 | 25.61 |
| 449.4 | 0.4455 | 0.3857 | 0.2809 | 15.50 |
| 560.2 | 0.5451 | 0.5092 | 0.2054 | 7.06 |
| 820.4 | 0.4427 | 0.4510 | 0.1968 | 1.84 |
| 919.4 | 0.4426 | 0.4330 | 0.2158 | 2.21 |
| 954.3 | 0.4726 | 0.4614 | 0.1800 | 2.44 |
| 966.4 | 0.4695 | 0.6976 | 0.2278 | 0.74 |
| 1166.7 | 0.5641 | 0.4843 | 0.1854 | 16.48 |
| 1298.7 | 0.5380 | 0.3902 | 0.2040 | 37.88 |

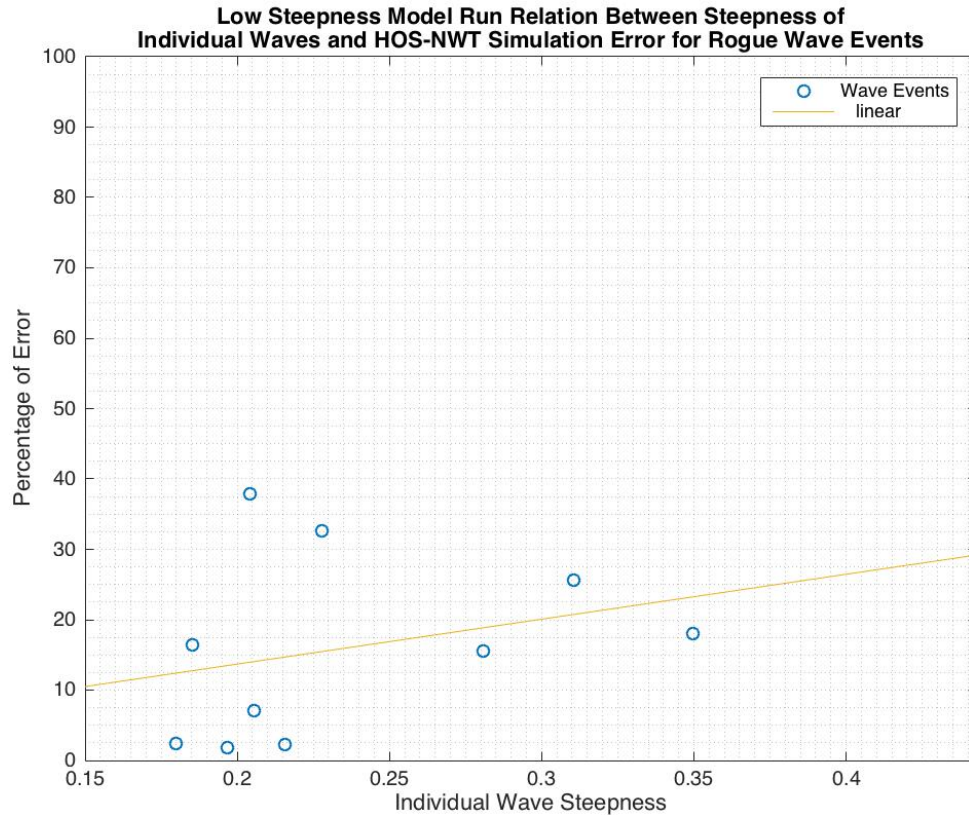


Figure 16: Plot depicting the relation of the individual wave steepness (α_k) of extreme wave events and the error calculated between the experimental data and the HOS-NWT simulation results for model run with steepness $\epsilon_c = 11.64\%$

5.3 Breaking Wave Identification:

After assessing the capabilities of the HOS-NWT model in terms of modeling extreme wave events, the focus of this study pivoted to the identification of breaking wave events using four different breaking criteria.

A total of 8 video clips, provided by MARINTEK, showed the breaking wave events that occurred over the course of 1300 seconds of experimentation, for the model run with a high level of steepness $\epsilon_c = 13.46\%$. It is important to mention that the experiment with a lower overall steepness level, $\epsilon_c = 11.64\%$, did not have any notable breaking events. Table 5 exhibits the times at which the videos witnessed the breaking wave events. Thorough analyses were conducted using each of the studied breaking criteria, and it was determined that the breaking criterion

that most accurately predicted the events from the videos was to be used to select breaking events for modeling using OpenFOAM. A series of figures showing snapshots from each of the breaking events shown in the video clips are present in Appendix A of this study.

Table 5: Time Stamps for breaking wave events that were captured on video for the model run with a higher level of steepness $\epsilon_c = 13.46\%$

| Case Number | Time (s) |
|-------------|----------|
| Event1 | 204.7 |
| Event2 | 259.8 |
| Event3 | 313.0 |
| Event4 | 490.4 |
| Event5 | 551.1 |
| Event6 | 734.4 |
| Event7 | 857.9 |
| Event8 | 999.9 |

In the following sub-sections, each of the four breaking criteria utilized in this study are applied to the data from the HOS-NWT model run with a high level of steepness, $\epsilon_c = 13.46\%$. Comparisons are made between each of the different criteria, focusing primarily on the 12th Wave Gauge and additional wave gauges adjacent to its location. It is important to note that both false positive fulfillments of each criterion as well as true identifications of the events outlined in Table 5 are present in each analysis.

5.3.1 Stokes Limiting Steepness Criterion:

When utilizing the Stokes Limiting Steepness Breaking Criterion [Stokes 1880] [Michell 1893], outlined in Section 3.3.1, individual waves were identified from the output of the HOS-NWT model of having steepnesses larger than

$ak = 0.443$. Special attention was given to wave gauges 9-13, measuring a total distance of 0.6 meters, covering 0.45 meters ahead of Wave Gauge 12, and 0.15 meters after it. Table 6 shows the breaking events witnessed in the video clips, with indications showing if those breaking events fulfilled the Stokes Limiting Steepness Criterion. In addition, false positive realizations of the criterion were inserted, and marked, showing the time stamps where the Stokes Limiting Steepness Criterion was fulfilled, but breaking was not observed in the videos. It is important to make notice of the fact that Wave Gauge 9, situated 0.45 meters away from the 12th Wave Gauge, registered no breaking events over the course of the entire simulation; therefore, no indicators (red or green highlights) are visible.

Table 6: Time stamps of wave breaking events from video clips with green highlights showing when the Stokes Limiting Steepness Breaking Criterion aligned with the events in Table 5 and red highlights showing false positive realizations

| | Wave Gauge 9 | Wave Gauge 10 | Wave Gauge 11 | Wave Gauge 12 | Wave Gauge 13 |
|----------------|--------------|---------------|---------------|---------------|---------------|
| Time Stamp (s) | 204.7 | 204.7 | 204.7 | 204.7 | 204.7 |
| | 259.8 | 259.8 | 259.8 | 259.8 | 259.8 |
| | 313.0 | 313.0 | 313.0 | 313.0 | 313.0 |
| | 490.4 | 490.4 | 326.3 | 406.5 | 316.5 |
| | 551.1 | 551.1 | 490.4 | 490.4 | 424.8 |
| | 734.4 | 597.6 | 551.1 | 551.1 | 490.4 |
| | 857.9 | 657.8 | 734.4 | 695.6 | 551.1 |
| | 999.9 | 734.4 | 857.9 | 734.4 | 734.4 |
| | | 857.9 | 999.9 | 750.4 | 770 |
| | | 999.9 | 1014 | 857.9 | 857.9 |
| | | 1202 | 1146 | 891.3 | 874.7 |
| | | | 1203 | 999.9 | 879.6 |
| | | | | 1137 | 999.9 |
| | | | | 1203 | |

Unfortunately, none of the breaking events that were measured by this criterion over the range covering the 9th to the 13th Wave Gauge matched with any of the events observed in the videos, hence the absence of any green highlights in Table 6. However, the Stokes Limiting Steepness Criterion did manage to make a measurement for Event4 from the videos. The criterion measured this event to have initiated at Wave Gauge 18, and based on the video, there does appear to be a breaking event occurring there. However, the video clip shows that the event originated near the 8th Wave Gauge, and continued to break past Wave Gauge 12, but went unrecognized by the Limiting Steepness Breaking Criterion in that area. Figure 17 shows snapshots of the video for Event4, giving a visual representation of the progression of when the event started at Wave Gauge 8 and how breaking continued past Wave Gauge 12. Due to the very poor agreement between the breaking events that were identified by the Stokes Limiting Steepness Criterion and what was observed in the videos, it was determined that this breaking criterion would not be suitable for use in identifying breaking events that could be used for coupling the HOS-NWT model with OpenFOAM.

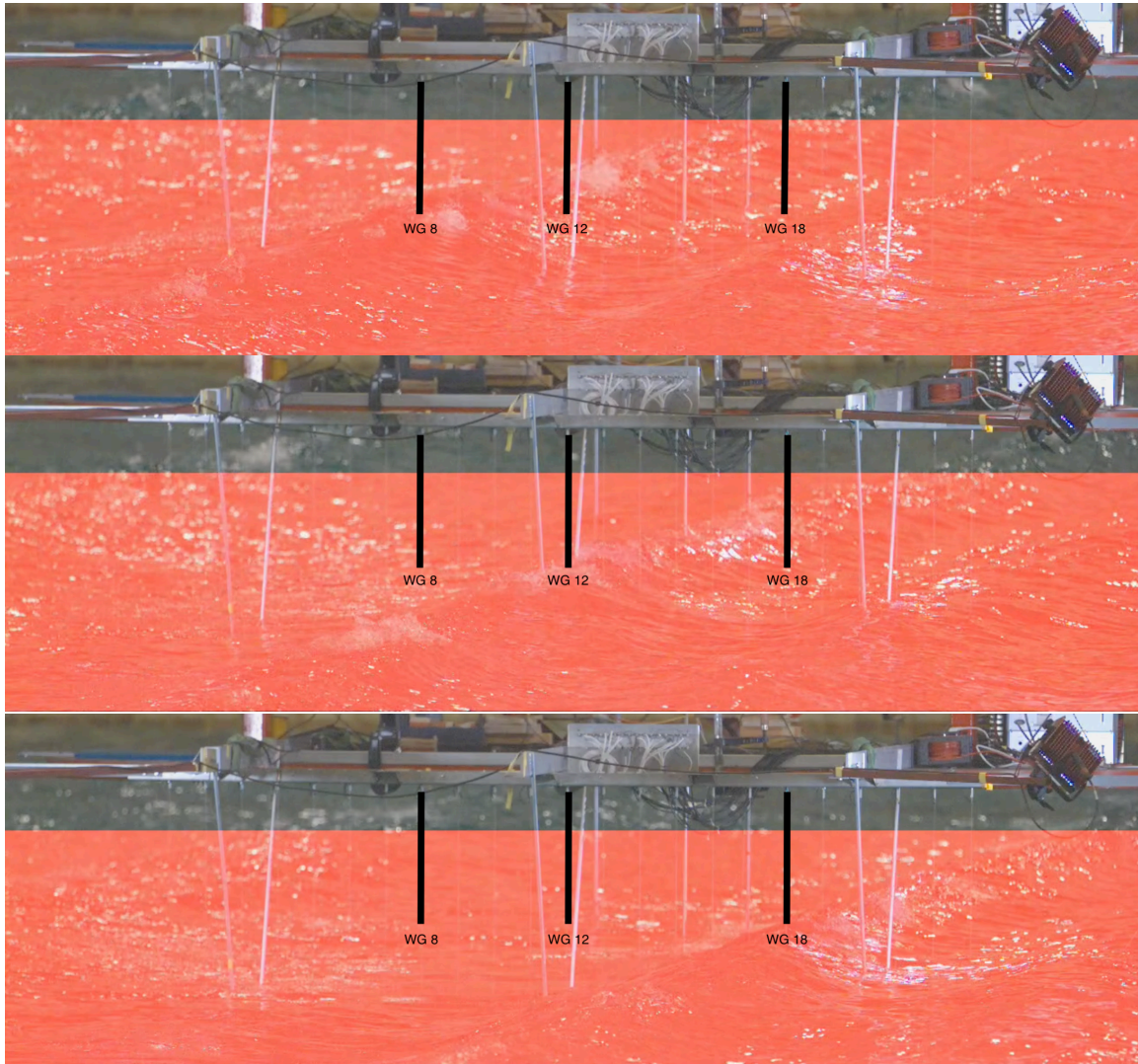


Figure 17: Breaking event (Event4) where onset occurred during experimentation at Wave Gauge 8 and breaking continued past Wave Gauge 12; the Stokes Limiting Steepness Criteria recognized it at Wave Gauge 18

5.3.2 Geometric Ratio Criterion:

The results that were found for the Geometric Ratio Breaking Criterion [Ochi & Tsai 1983], outlined in Section 3.3.1 in Equation 18, yielded very similar results as the Stokes Limiting Steepness Criterion. All of the instances where events were measured by the steepness criterion, from Wave Gauge 9 to 13, were also measured by the geometric ratio criterion. However, additional events were identified by the geometric ratio criterion at times where the steepness criterion went unfulfilled.

The information depicted in Table 7, in the exact same way as Table 6, shows the breaking events witnessed in the video clips, with indicators showing if those breaking events fulfilled the Geometric Ratio Breaking Criterion, and when false positive realizations of the criterion were made at times not represented in the videos.

Table 7: Time stamps of breaking events from video clips with green highlights showing instances where the Geometric Ratio Breaking Criterion aligned with the events in Table 5 and red highlights showing false positive realizations of the criterion

| | Wave Gauge 9 | Wave Gauge 10 | Wave Gauge 11 | Wave Gauge 12 | Wave Gauge 13 |
|----------------|--------------|---------------|---------------|---------------|---------------|
| Time Stamp (s) | 204.7 | 204.7 | 204.7 | 204.7 | 204.7 |
| | 259.8 | 259.8 | 259.8 | 259.8 | 259.8 |
| | 282.8 | 313.0 | 313.0 | 294.6 | 313.0 |
| | 313.0 | 490.4 | 318.8 | 313.0 | 316.5 |
| | 490.4 | 551.1 | 326.3 | 318.9 | 424.8 |
| | 551.1 | 597.6 | 406 | 406 | 490.4 |
| | 734.4 | 657.8 | 490.4 | 490.4 | 551.1 |
| | 857.9 | 734.4 | 551.1 | 551.1 | 734.4 |
| | 999.9 | 857.9 | 734.4 | 695.6 | 770 |
| | 1202 | 999.9 | 845.6 | 734.4 | 857.9 |
| | | 1202 | 857.9 | 750.4 | 874.4 |
| | | | 999.9 | 857.9 | 879.6 |
| | | | 1014 | 891.3 | 999.9 |
| | | | 1146 | 999.9 | 1090 |
| | | 1203 | 1137 | 1203 | |
| | | | 1203 | | |

In an effort to show the comparison between the Stokes Limiting Steepness Breaking Criterion, and the Geometric Ratio Breaking Criterion, Figure 18 was generated to show the fulfillments of each of the criteria over the length of the simulation, specifically at the 12th Wave Gauge. It is clearly shown that the Geometric Ratio Criterion measured each realization of the Stokes Limiting Steepness Criterion, and that an additional two realizations of the Geometric Ratio were measured that did not coordinate with events found by the Stokes Limiting Steepness Criterion. Note that the simulation shown in Figure 18 starts at 180 s rather than from zero; this is due to a recommendation from the MARINTEK facility where they consider the first 180s to be a ramp up time to allow for the wave maker to correctly propagate waves according to the input signal. Therefore, it was unnecessary to measure for breaking waves within that time frame from the HOS-NWT simulation.

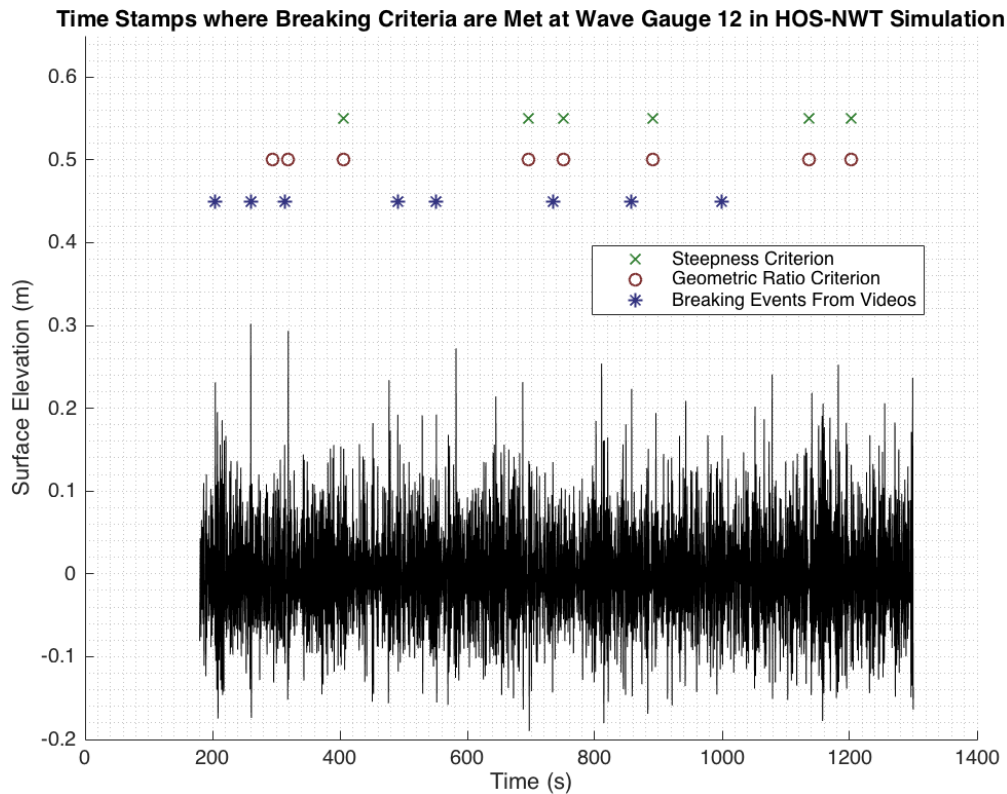


Figure 18: Breaking events measured by both the Stokes Limiting Steepness Criterion and the Geometric Ratio Breaking Criterion, as well as the breaking events observed on video starting from 180 s into the simulation and ending at 1300 s

The relationship shown between the steepness and geometric ratio criteria indicate that both of these criteria were implemented properly and came to similar conclusions for when and where they expected wave breaking to occur. However, as can be seen in Figure 18 and also recognized in Table 7, the Geometric Ratio Breaking Criteria failed to detect the breaking events captured on high-speed video at and adjacent to the 12th Wave Gauge.

5.3.3 Dynamic/Kinematic Criterion:

Another criterion that was applied to the output of the HOS-NWT model was the Dynamic/Kinematic Breaking Onset Criterion, developed in the research by Barthelemy et al. [2018]. This criterion was outlined in Section 3.3.3 using Equations 24, 25, and 26. The breaking ratio associated with this criterion was plotted over time for the locations representative of Wave Gauges 9 to 13, the plot for Wave Gauge 12 is represented in Figure 19, and the subsequent plots are located in Appendix B of this report. As was the case with the other studied breaking criteria, the first 180 seconds of the simulation were excluded from the breaking analysis.

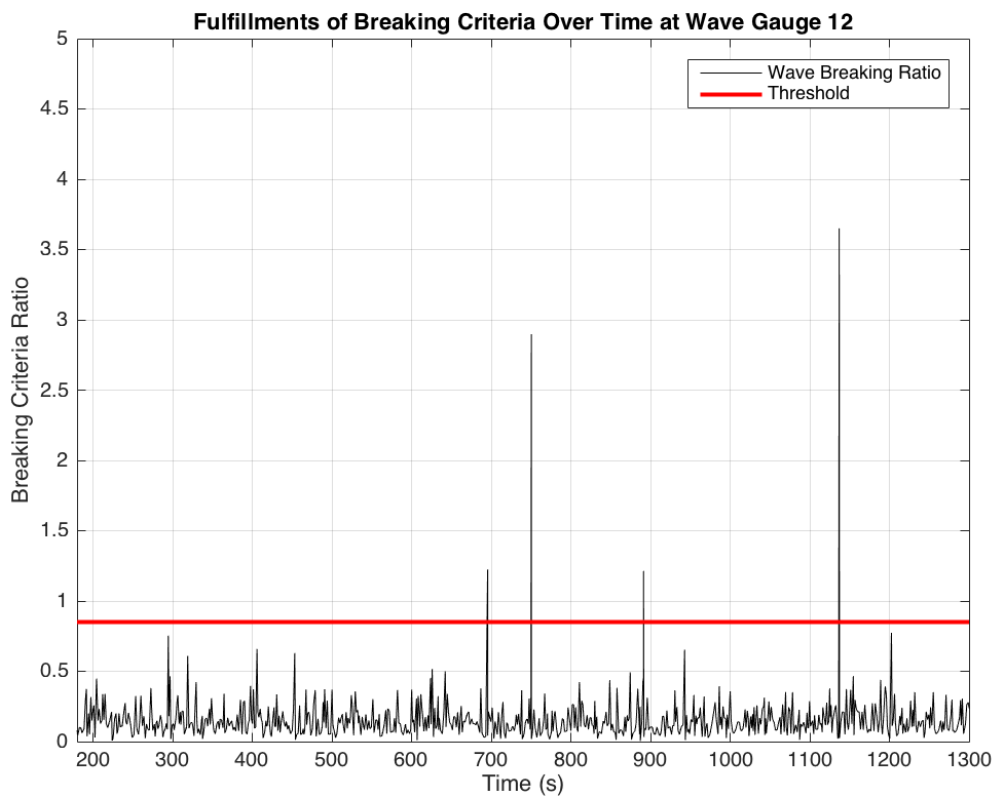


Figure 19: Realizations of the Dynamic/Kinematic Breaking Onset Criterion over the length of the simulation at Wave Gauge 12

According to Figure 19, there were a total of 4 fulfillments of the criterion at the location of the 12th Wave Gauge over the course of 1300 seconds. Table 8 focuses on the wave gauges starting from the 9th and finishing with the 13th; it shows the breaking events witnessed in the video clips, with indicators showing if those breaking events fulfilled the Dynamic/Kinematic Breaking Criterion, and if false positive realizations of the criterion were made at times not represented in the videos.

Table 8: Time stamps of wave breaking events from video clips with green highlights showing instances where the Dynamic/Kinematic Breaking Criterion aligned with the events in Table 5 and red highlights showing false positive realizations of the criterion

| | Wave Gauge 9 | Wave Gauge 10 | Wave Gauge 11 | Wave Gauge 12 | Wave Gauge 13 |
|----------------|--------------|---------------|---------------|---------------|---------------|
| Time Stamp (s) | 204.7 | 204.7 | 204.7 | 204.7 | 204.7 |
| | 259.8 | 259.8 | 259.8 | 259.8 | 259.8 |
| | 313.0 | 313.0 | 313.0 | 313.0 | 313.0 |
| | 490.4 | 490.4 | 326.3 | 490.4 | 316.5 |
| | 551.1 | 551.1 | 490.4 | 551.1 | 424.8 |
| | 734.4 | 657.8 | 551.1 | 695.6 | 490.4 |
| | 857.9 | 734.4 | 734.4 | 734.4 | 551.1 |
| | 999.9 | 857.9 | 857.9 | 750.4 | 734.4 |
| | | 999.9 | 999.9 | 857.9 | 770 |
| | | 1202 | 1014 | 891.3 | 857.9 |
| | | | | 999.9 | 874.7 |
| | | | | 1137 | 879.6 |
| | | | | | 999.9 |

The Dynamic/Kinematic Breaking Onset Criterion predicted the least number of breaking wave events out of the four criteria that were analyzed in this study. The results displayed in Table 8 align quite well with the results that were found when applying the Stokes Limiting Steepness Breaking Criterion and the Geometric Ratio Breaking Criterion to the output of the HOS-NWT model. A comparison of the time stamps when each of these criteria were fulfilled along with the Dynamic/Kinematic Breaking Onset Criterion, and the events captured on video, is illustrated in Figure 20.

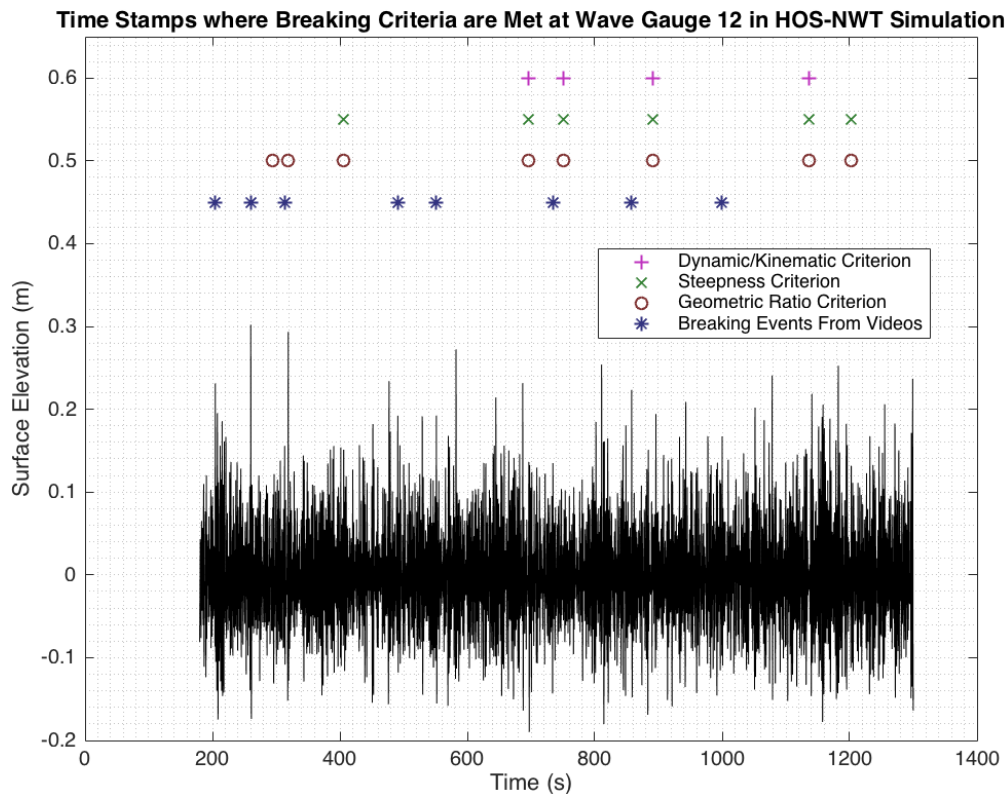


Figure 20: Comparison of the time stamps of breaking events measured by the Limiting Steepness, Geometric Ratio, and Dynamic/Kinematic Breaking Onset Criteria with what was observed on video

It was interesting to see that the Dynamic/Kinematic Breaking Criterion [Barthelemy et al. 2018] had close overlap with the steepness and geometric ratio

criteria developed by Stokes [1880] and Michell [1893], and Ochi & Tsai [1983], respectively. However, at the same time, the Dynamic/Kinematic Breaking Criterion did a poor job of identifying the events that were observed in the video clips.

Due to the fact that there was such a strong agreement between the Dynamic/Kinematic, Geometric Ratio, and Stokes Limiting Steepness Breaking Criteria, further analysis was conducted to see if the instances measured by the all three of these breaking criterion, in the range of Wave Gauge 9 to 13, were in fact breaking events not caught on camera. For example, by plotting the time series of the experimental data for the 12th Wave Gauge, as well as the wave gauges both 30 and 15 cm before it and the wave gauge situated 15 cm after it, a visualization of the growth of the events at the 12th Wave Gauge could be created. This procedure was undertaken to visualize the surface processes taking place when there was full agreement between the Dynamic/Kinematic, Geometric Ratio, and Stokes Limiting Steepness Breaking Criteria.

Figure 21 gives a representation of one of the events, specifically the event measured at the 12th Wave Gauge at 891.3 seconds. The behavior of the sea surface process at this point in time does not mirror what would be expected for a true breaking event. In theory, a breaking event would show a growth in wave height leading up to the time when breaking was believed to occur, and then a rapid decay signifying that the wave was broken. In this case, a wave crest passed the 12th Wave Gauge around 890.5 seconds, and then at 891.3 seconds, some slight irregularity in the trough of the wave is shown. The crest at 890.5 s continually grows after reaching each consecutive wave gauge, signifying that breaking is not in progress due to the absence of a rapid decay of the crest.

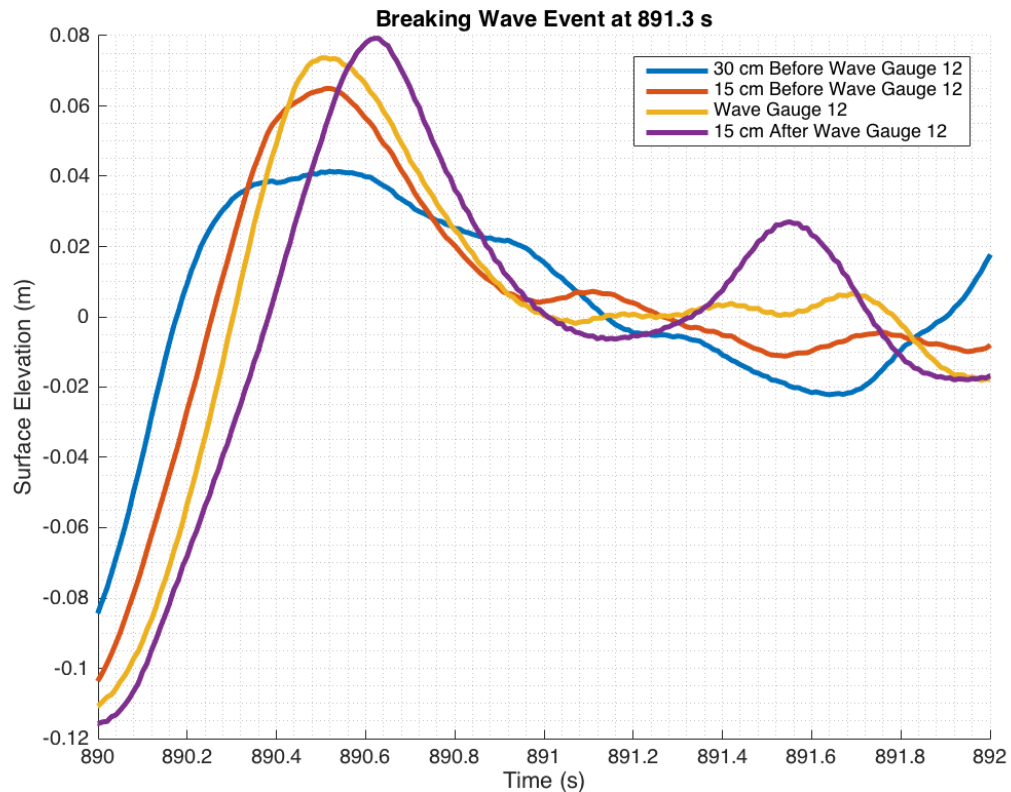


Figure 21: Experimental data showing the breaking wave event measured by the Dynamic/Kinematic, Geometric Ratio, and Stokes Limiting Steepness Breaking Criteria at 891.3 s at the 12th Wave Gauge

While a true breaking event may not have been present at the time exhibited in Figure 21, a confirmation of the nature of the events determined to be false positive realizations of each criterion, would be possible if a video monitoring the whole experiment was accessible.

One of the more interesting waves that was measured as a breaking event by the Dynamic/Kinematic Breaking Criterion was a wave that occurred at the 11th Wave Gauge at 1014 s. A zoomed in representation of the window in time where this wave occurred is illustrated in Figure 22. The importance of this breaking wave can be attributed to the fact that in a two-dimensional case, the applied dynamic breaking criterion reduces to a kinematic breaking criterion, and because of this, breaking is dependent upon the ratio between the water particle velocity and the

phase speed of each individual wave. Referring back to Equation 22, in Section 3.3.2, the traditional kinematic criterion would not have identified the wave at 1014 s due to the fact that the resulting kinematic ratio was less than 1. However, the modifications made in association with the utilized criterion, shown in Equation 24 [Barthelemy et al. 2018], allowed for the identification of this particular event, since the threshold for the breaking ratio was lowered to a value of 0.86. While this event was a false positive breaking event that did not correlate to one of the events captured on video, it still establishes the relation between the traditional kinematic breaking criterion, and the adjusted Dynamic/Kinematic Breaking Criterion.

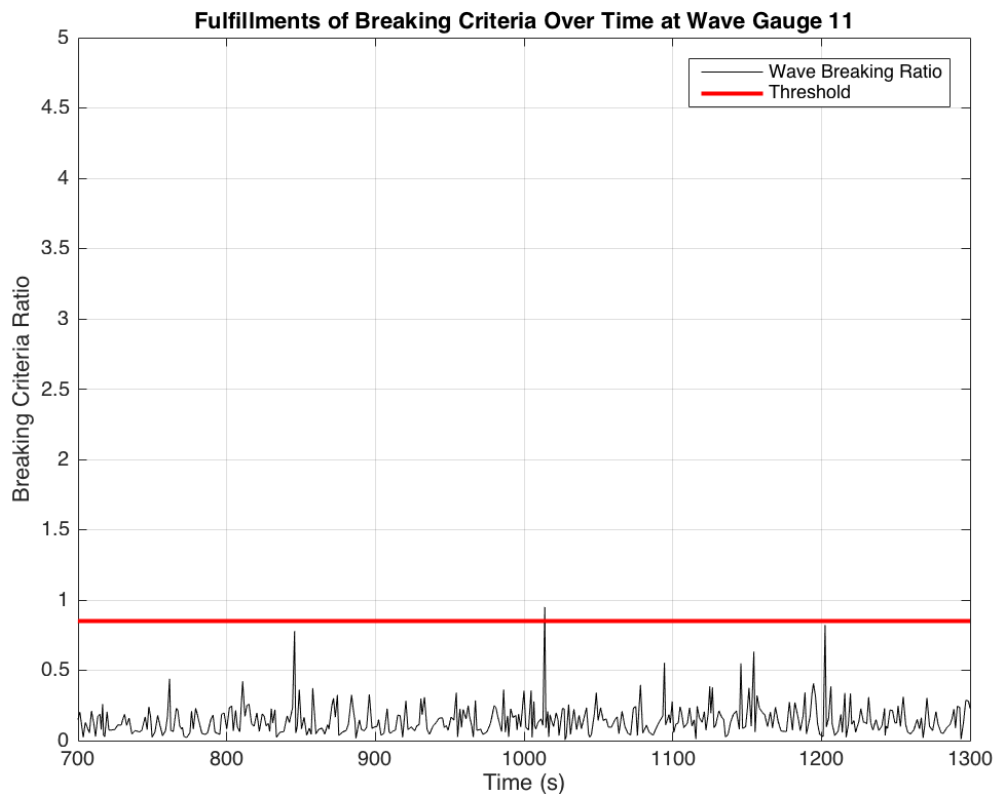


Figure 22: Zoomed in representation of the resulting dynamic breaking criterion ratio over time, with special attention given to the time window from 700-1300 s

Another important aspect of Figure 22 are two particular points in time where the value for the breaking criteria ratio grows to a relatively high value, but

does not surpass the breaking threshold. These instances occurred during the times of 845.6 s and 1202 s, aligning with two instances where the Geometric Ratio Breaking Criterion [Ochi & Tsai 1983], and the Stokes Limiting Steepness Criterion agreed, but the Dynamic/Kinematic Breaking Onset Criterion did not. This shows that the Dynamic/Kinematic Breaking Onset Criterion [Barthelemy et al. 2018] recognized that these two particular events were believed to be closer to becoming breaking waves than most, but evidently did not fulfill the condition.

Referring back to Figure 19, and the events occurring at the 12th Wave Gauge, the three highest formulations of the breaking ratio that did not surpass the breaking threshold coordinated with events at 294.6 s, 406 s, and 1202 s. Each of these events fulfilled the Stokes Limiting Steepness Breaking Criterion, the Geometric Ratio Breaking Criterion, or both, but not the Dynamic/Kinematic Breaking Criterion. This shows that the Dynamic/Kinematic Breaking Onset Criterion acknowledged the instability of these events, but did not go as far as to consider them as breaking events.

Plots representing the same characteristics as Figure 21 were generated to investigate if these events were breaking, as the limiting steepness and geometric ratio criteria showed, or if the events were non-breaking, as was perceived by the dynamic/kinematic criterion. Figure 23 displays the event measured at 406 s, where it shows the free surface appearing to be intact, and not exhibiting a rapid decay in wave height around the time where breaking was thought to have occurred. Similar characteristics were seen in the other two events that were analyzed, indicating that dynamic/kinematic criterion was able to weed out some of the false positive breaking event realizations found by the Stokes Limiting Steepness and Geometric Ratio Breaking Criteria. While the Dynamic/Kinematic Breaking Criterion eliminated some false positive realizations of the Stokes Limiting Steepness and Geometric Breaking Criteria, the inability of the Dynamic/Kinematic Criterion to recognize the events realized in the videos from MARINTEK made it unsuitable for use when selecting breaking events to be simulated in OpenFOAM.

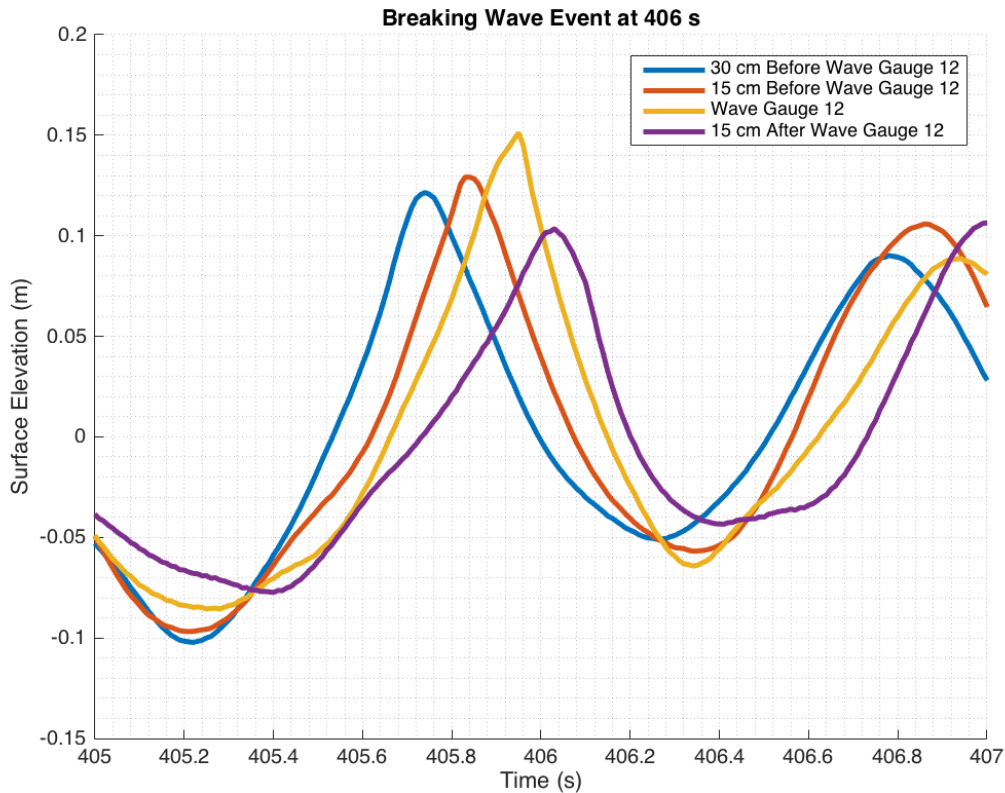


Figure 23: Experimental data showing the breaking wave event measured by the Stokes Limiting Steepness and Geometric Ratio Breaking Criteria, but not by the Dynamic/Kinematic Hybrid-Breaking Onset Criterion at 406 s at the 12th Wave Gauge

5.3.4 Limiting Slope Criterion:

The application of the breaking criterion related to the limiting slope of individual waves, detailed in Section 3.3.1 in Equations 19, 20, and 21, was unique in comparison to the other breaking criteria that were studied. As was previously mentioned, an opposing perspective of the capabilities of the limiting slope criterion, set forth in Babanin [2011], stated that the criterion was better suited as a tool to measure different properties and statistics of breaking waves in progress rather than as a predictive breaking onset criterion. This point of view was true in the sense that the criterion measured waves that were in the process of breaking.

However, this proved to be a strength of the criterion based on the fact that the location and time of breaking onset could be deduced from the criterion's findings. Table 9 shows the times when the Limiting Slope Breaking Criterion measured breaking with different indicators showing when fulfillments of the criterion matched what was caught on video and when false positive realizations occurred.

Table 9: Time stamps of wave breaking events from video clips with green highlights showing when the Limiting Slope Breaking Criterion aligned with the events in Table 5 and red highlights showing false positive realizations

| | Wave Gauge 9 | Wave Gauge 10 | Wave Gauge 11 | Wave Gauge 12 | Wave Gauge 13 |
|----------------|--------------|---------------|---------------|---------------|---------------|
| Time Stamp (s) | 186.1 | 204.7 | 204.7 | 204.7 | 204.7 |
| | 204.7 | 259.8 | 259.8 | 259.8 | 259.8 |
| | 259.8 | 313.0 | 313.0 | 313.0 | 313.0 |
| | 272.5 | 430.6 | 318.8 | 318.8 | 344.1 |
| | 313.0 | 490.4 | 430.7 | 430.8 | 424.8 |
| | 318.7 | 551.1 | 490.4 | 490.4 | 490.4 |
| | 430.5 | 597.6 | 551.1 | 551.1 | 551.1 |
| | 467.2 | 734.4 | 582.3 | 582.3 | 582.4 |
| | 490.4 | 857.9 | 600 | 600.1 | 644.9 |
| | 551.1 | 977.7 | 734.4 | 640.5 | 734.4 |
| | 686.7 | 999.9 | 848.8 | 644.8 | 857.9 |
| | 734.4 | 1066 | 857.9 | 687 | 977.6 |
| | 857.9 | 1078 | 933 | 734.4 | 999.9 |
| | 932.9 | 1292 | 977.4 | 750.8 | |
| | 999.9 | | 999.9 | 857.9 | |
| | 1066 | | | 977.5 | |
| | 1079 | | | 999.9 | |
| | | | | 1292 | |

Out of the 8 videos supplied by MARINTEK, the Limiting Slope Criterion was able to identify all 8 of the breaking events. It is important to note that Table 9 shows that the events at 734.4 and 999.9 seconds (Event6 & Event8) did not fulfill the criterion near the 12th Wave Gauge; however, these events fulfilled the Limiting Slope Breaking Criterion outside the range of wave gauges in Table 9. The videos confirmed that Event6 and Event8 occurred after the wave had already passed Wave Gauge 13, meaning the Limiting Slope Breaking Criterion was able to recognize this behavior. However, at the same time, several false positive realizations of this criterion also occurred, as is shown in Table 9.

Every event that was measured by the Limiting Slope Breaking Criterion along with the events measured by the other 3 criteria, at the 12th Wave Gauge, were plotted alongside the events that were captured on video in Figure 24. With all of the criteria being represented in one plot, a great comparison was made as to which breaking criterion best agreed with what was caught on the high-speed video feed.

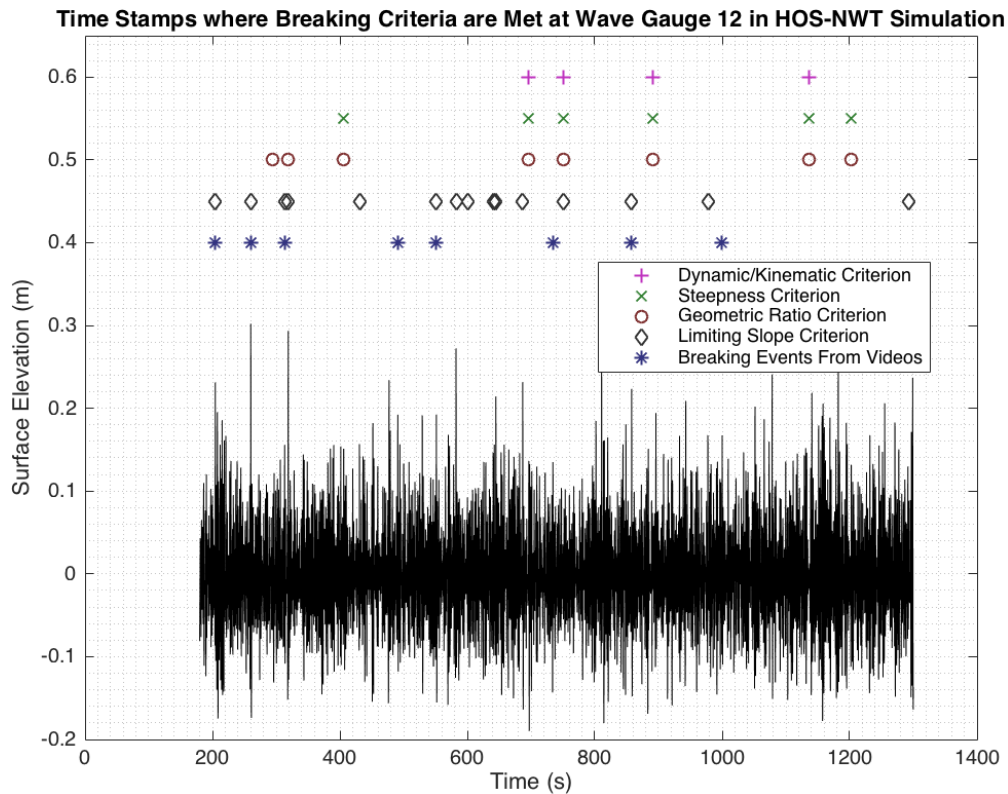


Figure 24: Comparison of breaking events measured during the HOS-NWT simulation by the all of the studied Breaking Criteria with what was observed on video

While several false positive realizations of the Limiting Slope Breaking Criterion can be seen in Figure 24, at the same time, many fulfillments of the criterion correlate to the breaking events that were captured on video. In comparison with the other criteria, the Limiting Slope Breaking Criterion was able to identify true breaking events that were physically observed at and around the 12th Wave Gauge, while the other breaking criteria were unable to do so. Five out of the eight breaking events seen in the videos were identified to be breaking by the Limiting Slope Breaking Criterion at the 12th Wave Gauge, while the remaining 3 events broke at different wave gauges.

To give an idea of the behavior of all 8 of the true breaking events, Figure 25 was created to show which wave gauges recognized the fulfillment of the Limiting

Slope Breaking Criterion while breaking was in progress. The figure itself shows the array of 23 wave gauges and the incident wave direction, from left to right, as well as blocked off areas, beneath designated wave gauges, signifying which gauges identified the breaking events from the videos in accordance with the Limiting Slope Breaking Criterion. The onset of each breaking event was determined to be located at the first wave gauge that fulfilled the Limiting Slope Breaking Criterion, for example breaking onset for Event7, at 857.9 seconds, occurred at the 12th Wave Gauge.

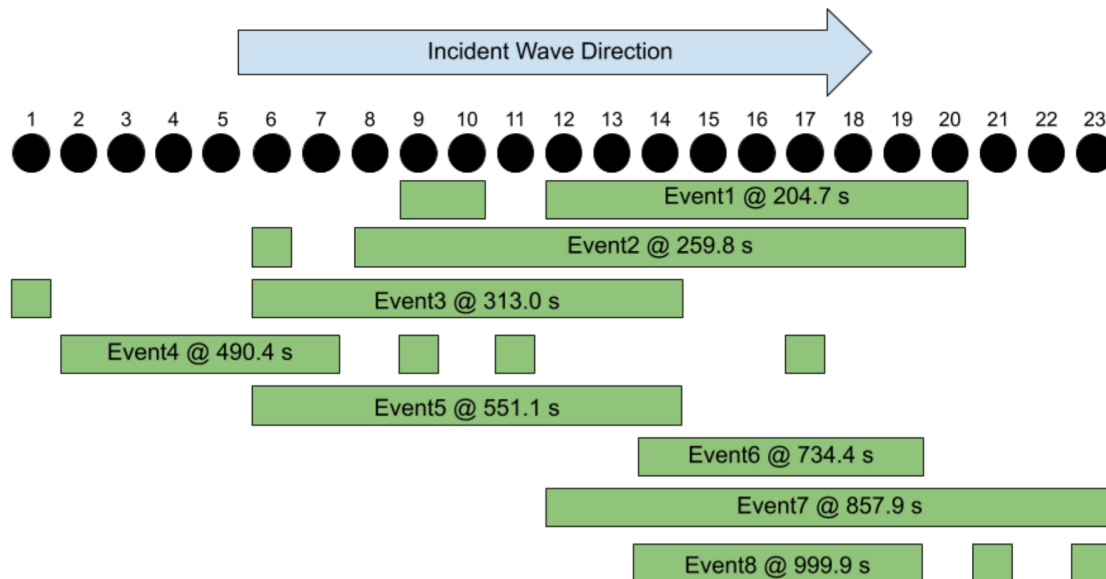


Figure 25: Breaking wave events found from video observations and the wave gauges that measured when the limiting slope breaking criterion was fulfilled

As is shown in Figure 25, 5 of the 8 events from the videos were measured to be breaking at the 12th Wave Gauge. Further analysis was conducted on each of the events caught on video to monitor whether the breaking events measured by the criterion were following what was observed in each of the videos. Overall, the breaking events matched what was measured by the criterion extremely well. Two examples are shown in Figures 26 and 27, where the progression of Event2 and Event7 (259.8 s and 857.9 s) are depicted. Markings on each of the snapshots are

made to show the locations of the wave gauges where breaking onset was believed to occur, where the each breaking event ended, as well as a marking for Wave Gauge 12.

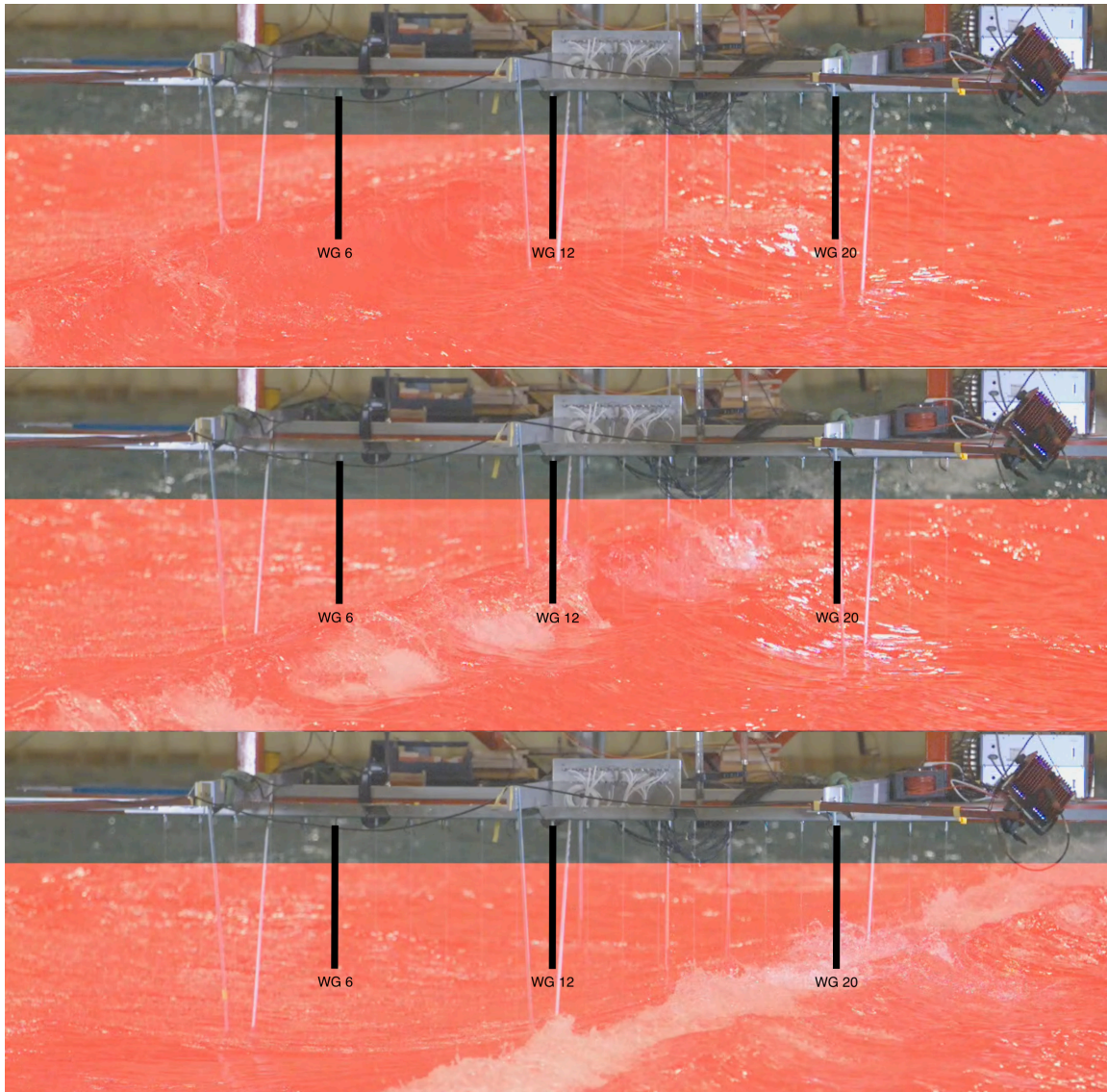


Figure 26: Progression of Event2 at 259.8 s showing breaking onset at Wave Gauge 6 and breaking process continuing past Wave Gauge 12 and ending at Wave Gauge 20

Event7 was a very important scenario that was studied; breaking onset, for this event, was believed to have occurred exactly at the 12th Wave Gauge. The

importance of this behavior is due to the fact that if breaking onset occurs at the location of a structure or vessel, signified by the location of the 12th Wave Gauge, large slamming forces have the potential to impact these objects, which can pose significant problems if unaccounted for [Chella et al. 2012].

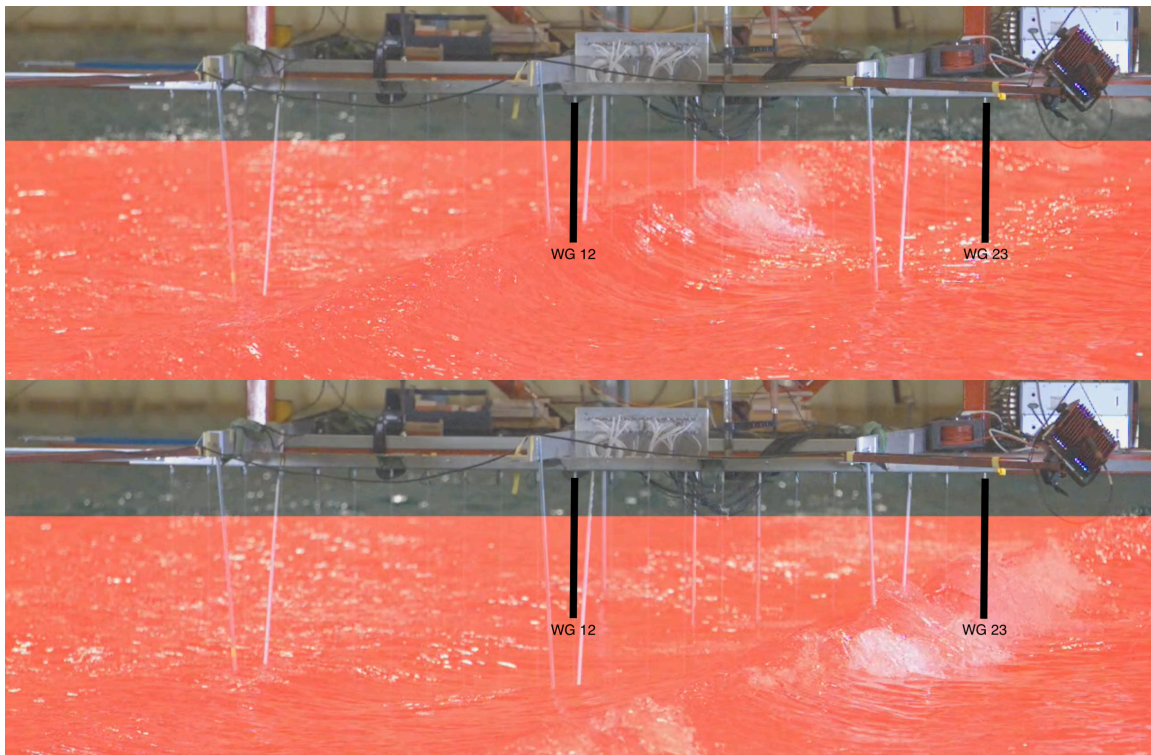


Figure 27: Progression of Event7 at 857.9 s showing breaking onset at Wave Gauge 12 and breaking process continuing past Wave Gauge 23

Ideally, a video feed monitoring the entirety of the experimentation that took place in the wave tank at MARINTEK would have allowed for a more robust assessment of the Limiting Slope Breaking Criterion, as well as all of the other breaking criteria. In that case, all of the events, both true and false positive realizations measured by each of the criteria, could have been observed using high-speed video, rather than only the true breaking events. This would have allowed for a better understanding of the accuracy of each of the criteria by having video evidence of the behavior of each event, rather than assessing false positive events with the characteristics of Figure 21 and 23.

5.3.5 Breaking Criteria Selection

After conducting thorough analyses on each of the four different breaking criteria researched in this study, it was determined that the most effective breaking criterion was the Limiting Slope Breaking Criterion [Longuet-Higgins & Fox 1977] [Longuet-Higgins & Smith 1983]. This criterion was able to measure all 8 of the breaking events recognized in the high-speed video clips at the appropriate locations and times. There were also a number of false positive realizations with the Limiting Slope Breaking Criterion that were tolerated due the poor performance of the other 3 breaking criteria and their inability to identify any of the breaking events caught on camera at the 12th Wave Gauge.

5.4 OpenFOAM

OpenFOAM simulations were conducted on 6 of the 8 true breaking events that were observed by both the high-speed video feed and the Limiting Slope Breaking Criterion. The two events that were excluded from this analysis included Event6 and Event8, both of which were observed to have breaking onset begin after Wave Gauge 13.

An important thing to note is that the end of the wave inlet relaxation zone coincided with the 1st Wave Gauge in the array. In order to ensure that the correct wave surface elevations were being modeled in each OpenFOAM simulation, the sea-surface process being simulated in OpenFOAM was compared with the HOS-NWT output at that location. It was found for all six of the simulated cases that there was exact agreement between the modeled surface elevations in OpenFOAM and the surface elevations output by the HOS-NWT model at the 1st Wave Gauge. Figure 28 shows the overlap of the surface elevations modeled using OpenFOAM and the HOS-NWT model for the time span involving Event1, indicating that the HOS-NWT model was successfully coupled with the OpenFOAM CFD software.

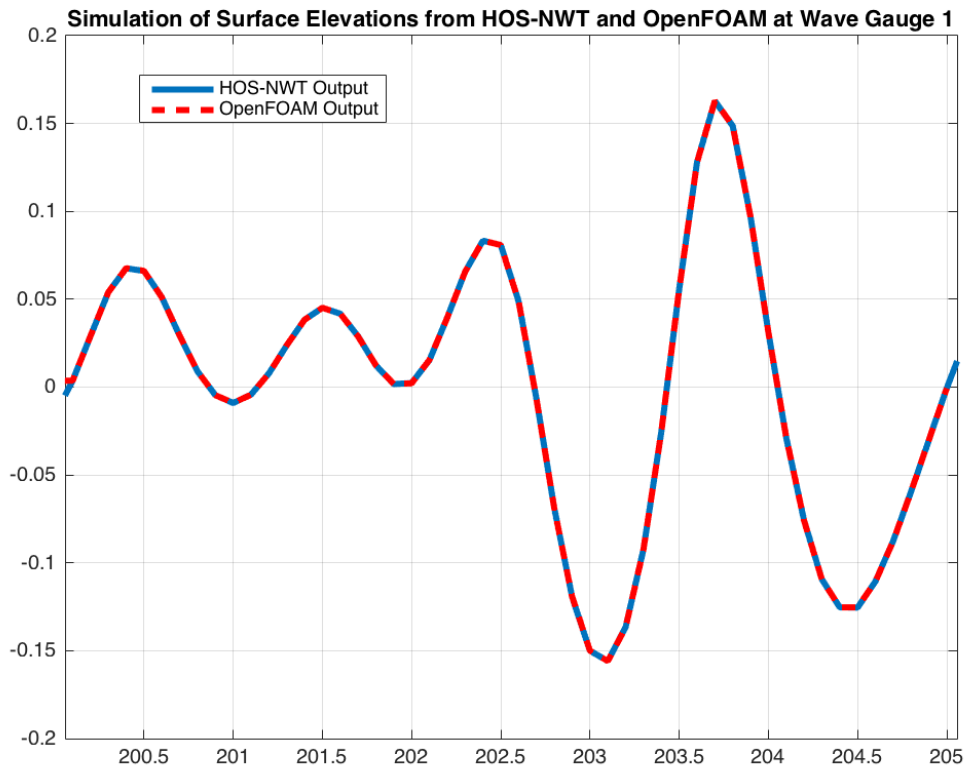


Figure 28: Comparison of the surface elevations of the OpenFOAM simulation and the HOS-NWT model at the 1st Wave Gauge for the time involving Event1

While the coupling of the HOS-NWT model and OpenFOAM was successful, it is important to recall from the extreme wave event analysis in Section 5.2 that, at times, errors were found between what was simulated by HOS-NWT and what was observed during model testing for some individual waves. Two events in particular, which experienced underestimations of their respective wave heights by the HOS-NWT model, were identified at 260.1 and 857.9 seconds at the 12th Wave Gauge, coinciding with the breaking events denominated as Event2 and Event7.

Similar to what is shown in Figure 28, a comparison of the surface elevations that were modeled for Event7, using HOS-NWT and OpenFOAM, are shown in Figure 29; however, within Figure 29, the comparison is shown for the 12th Wave Gauge, rather than the 1st, and includes the surface elevations observed during experimentation for that time as well.

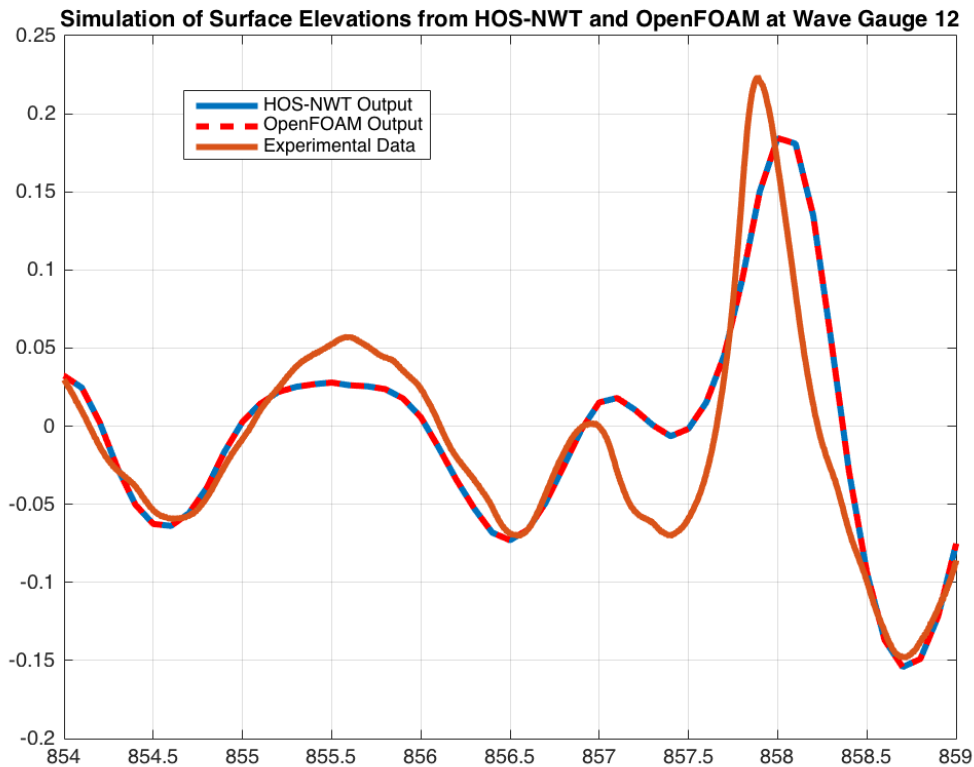


Figure 29: Comparison of the surface elevations of the OpenFOAM simulation, the output from the HOS-NWT model, and measurements made during model testing at the 12th Wave Gauge for the time involving the wave crest of Event7

The underestimation of the Event7's wave crest near 857.9 seconds, indicated by the HOS-NWT model, was replicated by OpenFOAM, and thus caused a misrepresentation of the sea-surface process within Event7's CFD simulation, in comparison to what was observed during model testing. Table 10 was compiled in an effort to show the errors that the HOS-NWT model experienced at the 12th Wave Gauge during each of the breaking events that were modeled using OpenFOAM.

Table 10: Errors between the wave crests from the HOS-NWT model output and experimental data, at Wave Gauge 12, for the breaking events identified by the Limiting Slope Breaking Criterion

| Event Number | Experimental Surface Elevation (m) | HOS-NWT Modeled Surface Elevation (m) | % Error |
|--------------|------------------------------------|---------------------------------------|---------|
| Event1 | 0.2313 | 0.1502 | 35.1 % |
| Event2 | 0.3021 | 0.1698 | 43.8 % |
| Event3 | 0.1558 | 0.0777 | 50.1 % |
| Event4 | 0.1923 | 0.0934 | 51.4 % |
| Event5 | 0.1924 | 0.1323 | 31.2 % |
| Event7 | 0.2234 | 0.1844 | 17.4 % |

The errors seen between the wave crests simulated by HOS-NWT and the model tests were simultaneously experienced within the SWENSE data that characterizes the parameters needed within the Navier-Stokes Equations (Equations 29-31) that govern all OpenFOAM simulations. On average the errors for the breaking wave events shown in Table 10 were approximately 38%.

In future work, adjustments could be made to the HOS-NWT model in an effort to reduce the experienced levels of error; this could be executed in a number of different ways, one of which would be to increase the non-linearity order M , as explained in Section 3.1, to a value greater than 8. Research by Ducroz et al. [2006] has studied HOS simulations that have been undertaken in numerical wave tank environments with orders of nonlinearity of up to $M=10$, with good results.

It must also be stated that an updated version of the HOS-NWT model, which has yet to be publicly released, has been linked with an appropriate energy dissipation model, which increases the robustness of the model in terms of being able to model breaking wave events [Seiffert et al. 2017]. The use of this model, upon its release, would likely improve the accuracy of the events represented in Table 10.

The lowest level of error, shown in Table 10, was experienced for Event7; a series of images, covering the time period where breaking was expected to occur, was generated to show the surface elevation and the particle velocities of this particular event.

5.4.1 Event7

In order to circumvent the potential flow assumptions, imbedded in the inputs from HOS-NWT, when breaking events were expected, the OpenFOAM simulation of each event was effectively decoupled from the HOS-NWT model immediately before breaking was expected to occur. By doing this, OpenFOAM could simulate the growth of each event in accordance with what was modeled in HOS-NWT, and then allow for the computation of highly non-linear turbulent processes for the breaking event. If the coupling between OpenFOAM and HOS-NWT was maintained throughout the time when breaking was expected, the OpenFOAM simulation would have strictly adhered to what was modeled in HOS-NWT, and the potential flow assumptions would inhibit the formation of breaking waves, resulting in a completely undisturbed sea-surface process.

Figure 30 contains the images depicting the sea surface elevations modeled within OpenFOAM for Event7; the red area is representative of the water phase, the blue indicates the air phase, and the white represents computational cells containing both the air and water phase within the simulation. The bounds of each sub-plot within Figure 30 are restricted to only show the stretch of the wave tank that contained the wave gauge array. It is also important to recognize that within each sub-plot, a time stamp is present indicating the state of the model at the appropriate times.

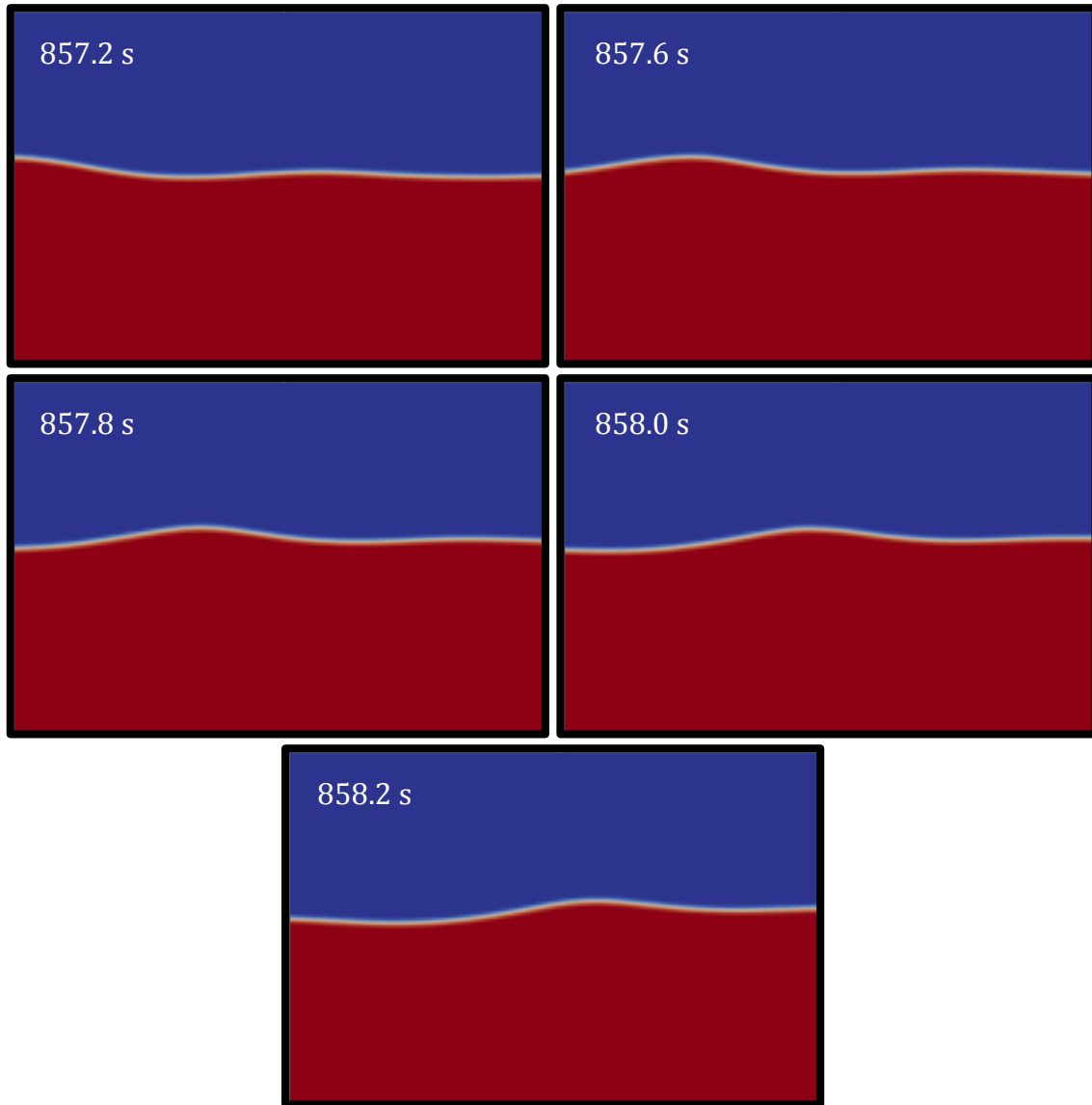


Figure 30: Sub-plots of surface elevations generated by the OpenFOAM simulation for Event7

The Limiting Slope Breaking Criterion and the video corresponding to Event7, showed that breaking occurred near the 12th Wave Gauge for this particular event. However, the simulation of a breaking wave event is clearly absent in Figure 30 due to the fact that there is no disruption of the sea-surface during this time. The absence of a breaking event being simulated in OpenFOAM could be attributed to a number of different factors, including the errors associated between the wave crest

input to OpenFOAM and what was observed in model tests, and the fact that the efficiency of the VOF method, employed by OpenFOAM, drops for waves with steepnesses greater than $s = \frac{H}{L} > 0.05$ yielding results that are less accurate [Afshar 2010] [Khalid 2016].

In an effort to gain more of an understanding of what was simulated within OpenFOAM, the particle velocities of both the air and water phases were also investigated. Sub-plots representing the particle velocities, specifically in the direction of wave propagation, for the same points in time that are represented in Figure 30 are depicted in Figure 32. The color scheme for the sub-plots in Figure 32, followed the scale illustrated in Figure 31; the units of the scale are in m/s, and show that particle velocities in the positive x-direction (left to right) are designated in darker shades of red with increasing magnitude, and that particle velocities in the negative x-direction (right to left) are designated in darker shades of blue with increasing magnitude.

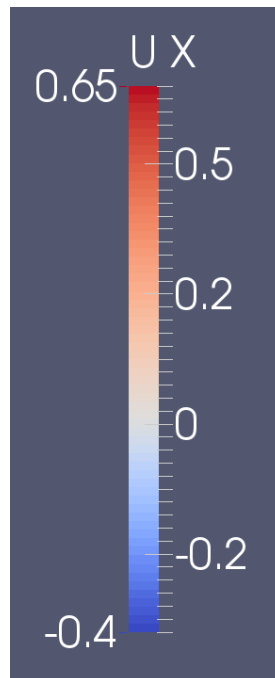


Figure 31: Scale employed for the visualization of the particle velocities, in the direction of wave propagation, of both the air and water phases for Event7 in Figure 32; units are in m/s

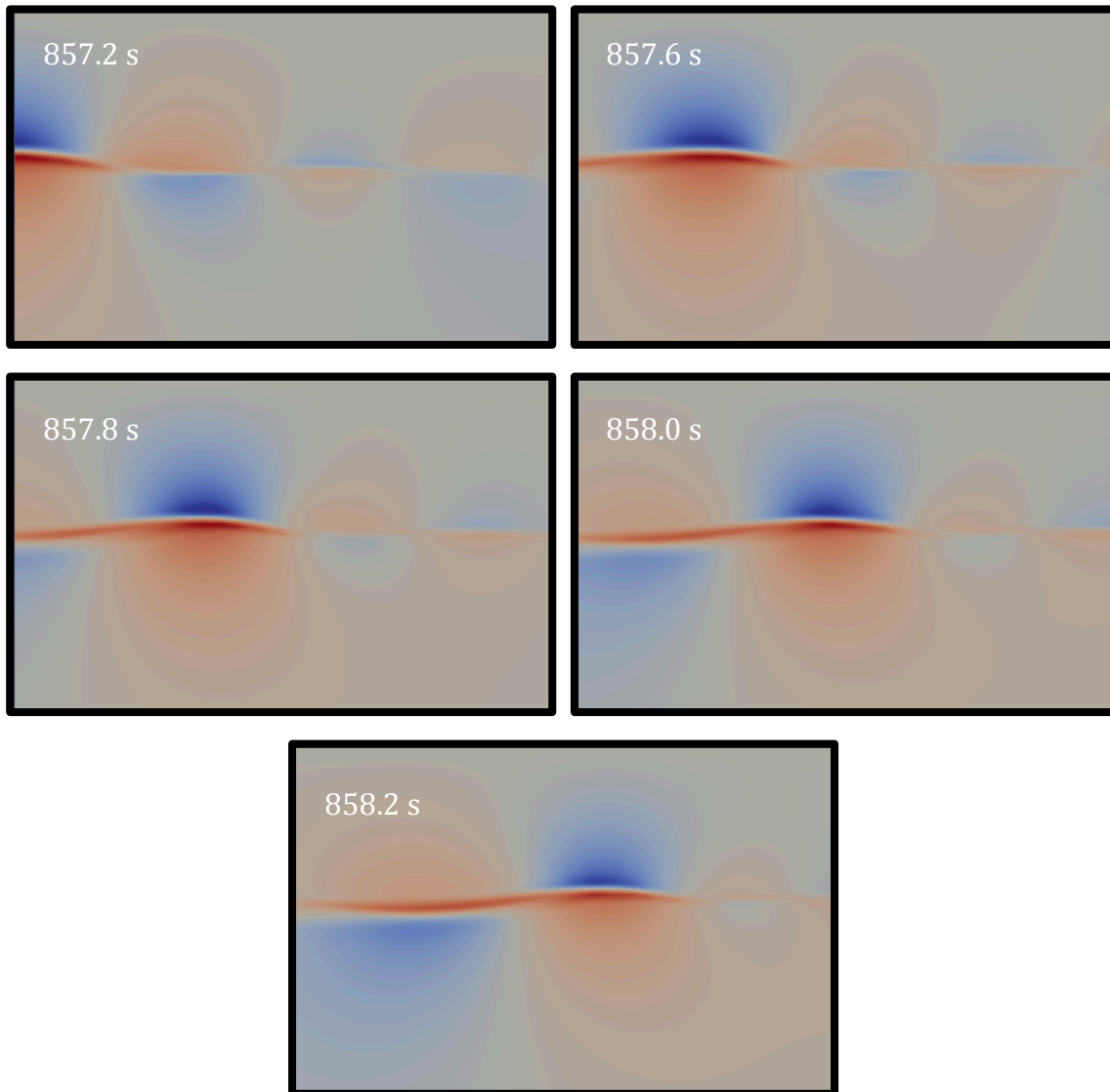


Figure 32: Sub-plots of particle velocities of both the air and water phases, in the direction of wave propagation, generated by the OpenFOAM simulation for Event7

As is shown in the sub-plots illustrated in Figure 32, particle velocities for the water phase in the crest of the wave that was expected to break are relatively high, in fact much higher than any of the other waves that were not expected to break in the simulation involving Event7. However, even with this increased amount of particle velocity, a visualization of the breaking that was observed during model testing was unable to be recreated in OpenFOAM. This behavior along with the

behavior illustrated in Figure 31, was observed for all of the OpenFOAM simulations for each of the six events that were modeled.

In addition to the large particle velocities of the water phase in the crest of the wave shown in Figure 32, large particle velocities in the negative x-direction are simultaneously shown in the air phase near the wave crest. These high velocities in the negative x-direction may have also contributed to the absence of the breaking processes being shown in the CFD simulation. Studies by Vukčević et al. [2017] and Li [2018] have investigated spurious air velocities near the air-water interface when using the VOF method. It has been determined that the relationship of both dynamic pressure and density gradients in Equation 32 in Section 3.4.1.1 can cause temporal changes in velocity that are in fact non-physical [Vukčević et al. 2017]. This compounded with the fact that the density of air is much less than that of water, causes a much greater change in velocity in the air phase, resulting in a spurious air velocity effect. The influence that these spurious air velocities may have within OpenFOAM has been shown by Afshar [2010], in some cases, to cause instances of premature breaking in deep-water breaking waves.

In a study by Liu et al. [2018], significant research was conducted on appropriate turbulence models for the simulation of breaking waves. The present study prioritized the use of the $k-\omega$ SST Turbulence Model (Section 3.4.1.1.1) due to its compatibility with the version of OpenFOAM used in this study. The findings of Liu et al. [2018] support the use of a modified Free Surface $k-\omega$ SST Turbulence Model, different from that of the original $k-\omega$ SST Turbulence Model that was used in this study. Liu et al. [2018] concluded that the original $k-\omega$ SST model caused a relatively large amount of turbulent kinetic energy in the area of the free surface, which allowed for greater dissipation and diffusion effects and led to non-breaking behavior in some instances. This effect may have also contributed to the absence of the breaking process for the events modeled in OpenFOAM for this study. Figures with the same characteristics as Figure 30 and 32 for the remaining 5 events that were simulated within OpenFOAM are visible in Appendix C.

6. Conclusion:

In this study, the open-source HOS-NWT model was utilized to numerically model a specific 3D model test that was performed at the MARINTEK facility, in an effort to investigate extreme and deep-water wave breaking events. The model test was executed using a single-hinged wave maker that produced a long-crested irregular wave field, which was reproduced in a 2D numerical simulation generated by the HOS-NWT model. The resulting simulation showed excellent agreement between significant wave height measurements at different gauges situated within the MARINTEK wave tank. Specific attention was given to the location of Wave Gauge 12, located in the center of the tank, where the calibration of the sea-surface process was being performed. The error between the experimental measurements and the numerical simulation at the 12th Wave Gauge showed only a 2.2% difference between the simulated and experimental significant wave heights.

The data from the model test was also used as a reference to validate the HOS-NWT model under extreme waves in deep water on a flat seabed. There was only one wave over the course of the 1300-second simulation that could be classified as a Rogue wave, where the height of the individual wave was more than twice that of the characteristic significant wave of the sea-state. Because of this, the extreme wave analysis was conducted on all waves that possessed a wave height greater than or equal to 1.5 times the significant wave height, of which there were a total of 10 events. The resulting analysis yielded high levels of error between some of the extreme events' wave heights that were simulated by HOS-NWT and what was seen during experimentation. However, 4 out of the 10 extreme waves had errors less than 10%. On average, an error of 14.42% was found for the 10 events. A slight trend was recognized that for growing levels of individual wave steepness, more error was found in the HOS-NWT simulation.

The results of the HOS-NWT model were also analyzed with a total of 4 breaking onset criteria, in an effort to identify breaking wave events in deep-water on a flat seabed. In total, 8 breaking wave events were known to have been present at different times during experimentation, as a result of observations made by high-

speed video clips provided by MARINTEK. The four criteria that were studied included a criterion involving the Stokes limiting steepness [Stokes 1880] [Michell 1893], a geometric ratio criterion [Ochi & Tsai 1983], a dynamic/kinematic criterion [Barthelemy et al. 2018], and a limiting slope criterion [Longuet-Higgins & Fox 1977] [Longuet-Higgins & Smith 1983]. The Dynamic/Kinematic, Geometric Ratio, and Stokes Limiting Steepness criteria, had excellent agreement between each other, but poor agreement with what was observed on video.

The breaking criterion that was ultimately selected to identify breaking events to be simulated in OpenFOAM was the Limiting Slope Breaking Criterion. This decision was made due to the fact that all 8 of the breaking events, identified in the video clips, were simultaneously measured by this criterion at the proper locations and times. However, there were a number of false positive realizations of the Limiting Slope Breaking Criterion that did not align with the events caught on video. These false positive realizations were tolerated due to the criterion's ability to measure all 8 of the true breaking events, in addition to the poor performance of the other 3 breaking criteria. It was determined that the superior performance of the Limiting Slope Breaking Criterion, in relation to the alternative criteria, was due to the fact that different assumptions were made for each of the criteria, which may have weakened their performances. For example, an assumption was made in this study allowing for the evaluation of the Dynamic/Kinematic Breaking Criterion at each individual wave, as opposed to being evaluated at every point within the domain of the HOS-NWT simulation [Seiffert et al. 2017].

After analyzing the outputs of the HOS-NWT model, with respect to breaking waves, steps were taken to couple HOS-NWT with the CFD software OpenFOAM. This effort was undertaken to give the option of simulating particular events in a CFD domain where breaking could be modeled and analyzed, without the constraint of the potential flow assumptions within HOS-NWT. The coupling of the two models proved to be successful, where the outputs of HOS-NWT were replicated within different OpenFOAM simulations. However, based in part on the errors in the outputs of the HOS-NWT software, the breaking processes of events that were both

identified by the Limiting Slope Breaking Criterion and caught on camera were unable to be visualized within OpenFOAM simulations. It was concluded that the shortfalls recognized in the OpenFOAM simulations were primarily related to the potential flow assumptions in the HOS-NWT software, which played a role in diminishing the value for the crest heights of the breaking waves by an average of 38%. This, as well as some other sources of error, outlined in Section 5.4 and Sub-Section 5.4.1 of this study, was attributed to the absence of the breaking processes within each of the OpenFOAM simulations conducted in this study.

In future work, a new version of the HOS-NWT model, which has yet to be publicly released, includes appropriate energy dissipation models, which increase the robustness of HOS-NWT in terms of being able to model breaking wave events [Seiffert et al. 2017]. In addition to this, measures could also be taken to improve the OpenFOAM simulations through the implementation of an alternative turbulence model, such as the modified Free Surface $k-\omega$ SST Turbulence Model, suggested by Liu et al. [2018]. Furthermore, the HOS-NWT model could be reconditioned to allow for wave propagation on variable bathymetries such as a sloping seabed. Lastly, the MARINTEK facility also runs 3D model tests utilizing a double-hinged wave maker; the HOS-NWT model could be modified to allow for wave generation from wave makers with this particular geometry.

7. References:

- Afshar, Mostafa Amini. "Numerical wave generation in OpenFOAM®." (2010).
- Agnon, Yehuda, and Harry B. Bingham. "A non-periodic spectral method with application to nonlinear water waves." *European journal of mechanics. B, Fluids* 18.3 (1999): 527-534.
- Babanin, A. V., et al. "Wave breaking in directional fields." *Journal of Physical Oceanography* 41.1 (2011): 145-156.
- Babanin, Alexander. *Breaking and dissipation of ocean surface waves*. Cambridge University Press, 2011.
- Barthelemy, X., et al. "On a unified breaking onset threshold for gravity waves in deep and intermediate depth water." *Journal of Fluid Mechanics* 841 (2018): 463-488.
- Berberović, Edin, et al. "Drop impact onto a liquid layer of finite thickness: Dynamics of the cavity evolution." *Physical Review E* 79.3 (2009): 036306.
- Bingham, Harry B., and Haiwen Zhang. "On the accuracy of finite-difference solutions for nonlinear water waves." *Journal of Engineering Mathematics* 58.1-4 (2007): 211-228.
- Bonnefoy, Félicien, David Le Touzé, and Pierre Ferrant. "A fully-spectral 3D time-domain model for second-order simulation of wavetank experiments. Part A: Formulation, implementation and numerical properties." *Applied Ocean Research* 28.1 (2006): 33-43.
- Bonnefoy, Félicien, et al. "Time domain simulation of nonlinear water waves using spectral methods." *Advances in Numerical Simulation of Nonlinear Water Waves*. 2010. 129-164.
- Brown, S. A., et al. "Evaluation of turbulence closure models under spilling and plunging breakers in the surf zone." *Coastal Engineering* 114 (2016): 177-193.
- Bruinsma, N. "Validation and application of a fully nonlinear numerical wave tank." (2016).

- Cash, Jeff R., and Alan H. Karp. "A variable order Runge-Kutta method for initial value problems with rapidly varying right-hand sides." *ACM Transactions on Mathematical Software (TOMS)* 16.3 (1990): 201-222.
- Chai, Kenric, M. S. Liew, and H. E. Lee. "Numerical wave tank modelling of regular waves propagation using OpenFOAM." *2017 3rd International Conference on Power Generation Systems and Renewable Energy Technologies (PGSRET)*. IEEE, 2017.
- Chella, Mayilvahanan Alagan, Alf Tørum, and Dag Myrhaug. "An overview of wave impact forces on offshore wind turbine substructures." *Energy Procedia* 20 (2012): 217-226.
- Chella, Mayilvahanan Alagan, et al. "Hydrodynamic characteristics and geometric properties of plunging and spilling breakers over impermeable slopes." *Ocean Modelling* 103 (2016): 53-72.
- Choi, YoungMyung, et al. "Grid2Grid: HOS Wrapper Program for CFD solvers." *arXiv preprint arXiv:1801.00026* (2017).
- Devolder, Brecht, Peter Troch, and Pieter Rauwoens. "Performance of a buoyancy-modified $k-\omega$ and $k-\omega$ SST turbulence model for simulating wave breaking under regular waves using OpenFOAM®." *Coastal Engineering* 138 (2018): 49-65.
- Dommermuth, Douglas G., and Dick KP Yue. "A high-order spectral method for the study of nonlinear gravity waves." *Journal of Fluid Mechanics* 184 (1987): 267-288.
- Dommermuth, Douglas G., and Dick KP Yue. "The nonlinear three-dimensional waves generated by a moving surface disturbance." *Proceedings of the 17th Symposium on Naval Hydrodynamics*. National Academy Press, 1988.
- Dommermuth, Douglas. "The initialization of nonlinear waves using an adjustment scheme." *Wave motion* 32.4 (2000): 307-317.
- Ducrozet, G., et al. "Implementation and validation of nonlinear wavemaker models in a HOS numerical wave tank." *International Journal of Offshore and Polar Engineering* 16.03 (2006).

- Ducrozet, Guillaume, Félicien Bonnefoy, and Pierre Ferrant. "Rogue waves in large-scale fully-non-linear High-Order-Spectral simulations." *Proc. 22nd International Workshop on Water Waves and Floating Bodies (IWWWFB), Croatia*. 2007.
- G. Ducrozet, F. Bonnefoy, D. Le Touzé, P. Ferrant. 3-D HOS simulations of extreme waves in open seas. *Natural Hazards and Earth System Science, Copernicus Publications on behalf of the European Geosciences Union*, 2007, 7 (1), pp.109-122. <hal-00330919>
- Ducrozet, Guillaume, et al. "A comparative study of two fast nonlinear free-surface water wave models." *International Journal for Numerical Methods in Fluids* 69.11 (2012): 1818-1834.
- Ducrozet, Guillaume, et al. "A modified high-order spectral method for wavemaker modeling in a numerical wave tank." *European Journal of Mechanics-B/Fluids* 34 (2012): 19-34.
- Ducrozet, Guillaume, et al. "HOS-ocean: Open-source solver for nonlinear waves in open ocean based on High-Order Spectral method." *Computer Physics Communications* 203 (2016): 245-254.
- Ducrozet, Guillaume, Félicien Bonnefoy, and Yves Perignon. "Applicability and limitations of highly non-linear potential flow solvers in the context of water waves." *Ocean Engineering* 142 (2017): 233-244.
- Engsig-Karup, Allan Peter, Harry B. Bingham, and Ole Lindberg. "An efficient flexible-order model for 3D nonlinear water waves." *Journal of computational physics* 228.6 (2009): 2100-2118.
- Fochesato, Christophe, Stéphan Grilli, and Frédéric Dias. "Numerical modeling of extreme rogue waves generated by directional energy focusing." *Wave Motion* 44.5 (2007): 395-416.
- Fuhrman, David R., Per A. Madsen, and Harry B. Bingham. "Numerical simulation of lowest-order short-crested wave instabilities." *Journal of Fluid Mechanics* 563 (2006): 415-441.

- Greaves, Deborah. "A quadtree adaptive method for simulating fluid flows with moving interfaces." *Journal of Computational Physics* 194.1 (2004): 35-56.
- Greenshields, Christopher J. "OpenFOAM: The Open Source CFD Toolbox, User Guide." *OpenFOAM Foundation Ltd* (2018).
- Grilli, Stephan T., J. Skourup, and Ib A. Svendsen. "An efficient boundary element method for nonlinear water waves." *Engineering Analysis with Boundary Elements* 6.2 (1989): 97-107.
- Grilli, Stephan T., Philippe Guyenne, and Frédéric Dias. "A fully non-linear model for three-dimensional overturning waves over an arbitrary bottom." *International Journal for Numerical Methods in Fluids* 35.7 (2001): 829-867.
- Haver, S. and Andersen, O. J. (2000): "Freak waves – Rare Realizations of a Typical Population or Typical Realizations of a Rare Population?", ISOPE'2000, Seattle.
- Haver, Sverre. "A possible freak wave event measured at the Draupner Jacket January 1 1995." *Rogue waves*. Vol. 2004. 2004.
- Higuera, Pablo, Javier L. Lara, and Inigo J. Losada. "Realistic wave generation and active wave absorption for Navier–Stokes models: Application to OpenFOAM®." *Coastal Engineering* 71 (2013): 102-118.
- Hirt, Cyril W., and Billy D. Nichols. "Volume of fluid (VOF) method for the dynamics of free boundaries." *Journal of computational physics* 39.1 (1981): 201-225.
- Jacobsen, Niels G., David R. Fuhrman, and Jørgen Fredsøe. "A wave generation toolbox for the open-source CFD library: OpenFoam®." *International Journal for numerical methods in fluids* 70.9 (2012): 1073-1088.
- Jacobsen, N. "waves2Foam Manual." *Deltares, The Netherlands* (2017).
- Khalid, Muhammad Nouman. *Design Optimization of Snorre A Tension Leg Platform (TLP) for Extreme Wave Event*. MS thesis. University of Stavanger, Norway, 2016.
- Kharif, Christian, and Efim Pelinovsky. "Physical mechanisms of the rogue wave phenomenon." *European Journal of Mechanics-B/Fluids* 22.6 (2003): 603-634.

- Kjeldsen, Søren Peter, and Dag Myrhaug. "Wave-wave interactions, current-wave interactions and resulting extreme waves and breaking waves." *Coastal Engineering* 1980. 1980. 2277-2303.
- Kurnia, Ruddy, and E. Van Groesen. "High order Hamiltonian water wave models with wave-breaking mechanism." *Coastal engineering* 93 (2014): 55-70.
- Li, Zhaobin. *Two-phase spectral wave explicit Navier-Stokes equations method for wave-structure interactions*. Diss. 2018.
- Liu, Yuming, and Dick KP Yue. "On generalized Bragg scattering of surface waves by bottom ripples." *Journal of Fluid Mechanics* 356 (1998): 297-326.
- Liu, Yuming, Douglas G. Dommermuth, and Dick KP Yue. "A high-order spectral method for nonlinear wave-body interactions." *Journal of fluid Mechanics* 245 (1992): 115-136.
- Liu, S., Ong, M.C., Obhrai, C., Gatin, I., Vukčević, V. (2018). Evaluation of free surface jump condition and different $k - \omega$ SST turbulence models in breaking wave modelling. *Ocean Engineering*. (Under review)
- Liu, Shengnan, et al. "Characteristics of higher-harmonic breaking wave forces and secondary load cycles on a single vertical circular cylinder at different Froude numbers." *Marine Structures* 64 (2019): 54-77.
- Longuet-Higgins, Michael S., and M. J. H. Fox. "Theory of the almost-highest wave: the inner solution." *Journal of Fluid Mechanics* 80.4 (1977): 721-741.
- Longuet-Higgins, M. S., and N. D. Smith. "Measurement of breaking waves by a surface jump meter." *Journal of Geophysical Research: Oceans* 88.C14 (1983): 9823-9831.
- Luquet, R., et al. "Applications of the SWENSE Method to seakeeping simulations in irregular waves." *Proc of the 9th Int. Conf. on Num. Ship Hydro*. 2007.
- Mayer, Stefan, Antoine Garapon, and Lars S. Sørensen. "A fractional step method for unsteady free-surface flow with applications to non-linear wave dynamics." *International Journal for Numerical Methods in Fluids* 28.2 (1998): 293-315.

- Mayer, Stefan, and Per A. Madsen. "Simulation of breaking waves in the surf zone using a Navier-Stokes solver." *27th International Conference on Coastal Engineering*. 2000.
- Menter, Florian R. "Two-equation eddy-viscosity turbulence models for engineering applications." *AIAA journal* 32.8 (1994): 1598-1605.
- Menter, Florian R., Martin Kuntz, and Robin Langtry. "Ten years of industrial experience with the SST turbulence model." *Turbulence, heat and mass transfer* 4.1 (2003): 625-632.
- Michell, John H. "XLIV. The highest waves in water." *The London, Edinburgh, and Dublin Philosophical Magazine and Journal of Science* 36.222 (1893): 430-437.
- Mohammadi, Bijan, and Olivier Pironneau. "Analysis of the k-epsilon turbulence model." (1993).
- Ochi, Michel K., and Cheng-Han Tsai. "Prediction of occurrence of breaking waves in deep water." *Journal of Physical Oceanography* 13.11 (1983): 2008-2019.
- "OpenFOAM Foundation, The." *OpenFOAM*, CFD Direct, February 2019, openfoam.org/
- Paulsen, Bo Terp, Henrik Bredmose, and Harry B. Bingham. "An efficient domain decomposition strategy for wave loads on surface piercing circular cylinders." *Coastal Engineering* 86 (2014): 57-76.
- Perlin, Marc, Wooyoung Choi, and Zhigang Tian. "Breaking waves in deep and intermediate waters." *Annual review of fluid mechanics* 45 (2013): 115-145.
- Rienecker, M. M., and J. D. Fenton. "A Fourier approximation method for steady water waves." *Journal of Fluid Mechanics* 104 (1981): 119-137.
- Robertson, E., et al. "Validation of OpenFOAM numerical methods and turbulence models for incompressible bluff body flows." *Computers & Fluids* 123 (2015): 122-145.
- Rusche, Henrik. *Computational fluid dynamics of dispersed two-phase flows at high phase fractions*. Diss. Imperial College London (University of London), 2003.

- Saket, Arvin, et al. "Wave breaking onset of two-dimensional deep-water wave groups in the presence and absence of wind." *arXiv preprint arXiv:1508.07702* (2015).
- Seiffert, Betsy, Ducrozet, Guillaume. Deep water wave-breaking in a High-Order Spectral model. 31th Intl Workshop on Water Waves and Floating Bodies, Apr 2016, Plymouth, United States. 2016. <hal- 01344691>
- Seiffert, Betsy R., Guillaume Ducrozet, Félicien Bonnefoy, Simulation of breaking waves using the High-Order Spectral method with laboratory experiments: Wave-breaking onset, *Ocean Modelling* (2017), doi: [10.1016/j.ocemod.2017.09.006](https://doi.org/10.1016/j.ocemod.2017.09.006)
- Stansell, Paul, and Colin MacFarlane. "Experimental investigation of wave breaking criteria based on wave phase speeds." *Journal of physical oceanography* 32.5 (2002): 1269-1283.
- Stokes, G. G.. "Appendices and supplement to a paper on the theory of oscillatory waves." *Math. Phys. Pap.* 1:219–29 (1880)
- Tian, Zhigang, Marc Perlin, and Wooyoung Choi. "Evaluation of a deep-water wave breaking criterion." *Physics of Fluids* 20.6 (2008): 066604.
- Vukčević, Vuko, Hrvoje Jasak, and Inno Gatin. "Implementation of the Ghost Fluid Method for free surface flows in polyhedral Finite Volume framework." *Computers & Fluids* 153 (2017): 1-19.
- Vyzikas, Thomas, et al. "Integrated numerical modelling system for extreme wave events at the wave hub site." *ICE Conference on Coasts, Marine Structures and Breakwaters*. 2013.
- Vyzikas, Thomas, et al. "Numerical study of fixed Oscillating Water Column with RANS-type two-phase CFD model." *Renewable energy* 102 (2017): 294-305.
- West, Bruce J., et al. "A new numerical method for surface hydrodynamics." *Journal of Geophysical Research: Oceans* 92.C11 (1987): 11803-11824.
- Wilcox, David C. "Reassessment of the scale-determining equation for advanced turbulence models." *AIAA journal* 26.11 (1988): 1299-1310.

- Wilcox, David C. "Formulation of the kw turbulence model revisited." *AIAA journal* 46.11 (2008): 2823-2838.
- Wu, Guangyu. *Direct simulation and deterministic prediction of large-scale nonlinear ocean wave-field*. Diss. Massachusetts Institute of Technology, (2004).
- Xie, Zhihua. "Two-phase flow modelling of spilling and plunging breaking waves." *Applied Mathematical Modelling* 37.6 (2013): 3698-3713.
- V. Zakharov. Stability of periodic waves of finite amplitude on the surface of a deep fluid. *J. Appl. Mech. Tech. Phys.*, pages 190–194, 1968.
- Zhang, Jun, Keyyong Hong, and Dick KP Yue. "Effects of wavelength ratio on wave modeling." *Journal of Fluid Mechanics* 248 (1993): 107-127.
- Zhu, Qiang. *Features of nonlinear wave-wave and wave-body interactions*. Diss. Massachusetts Institute of Technology, 2000.

8. Appendices:

Appendix A:

Event1:

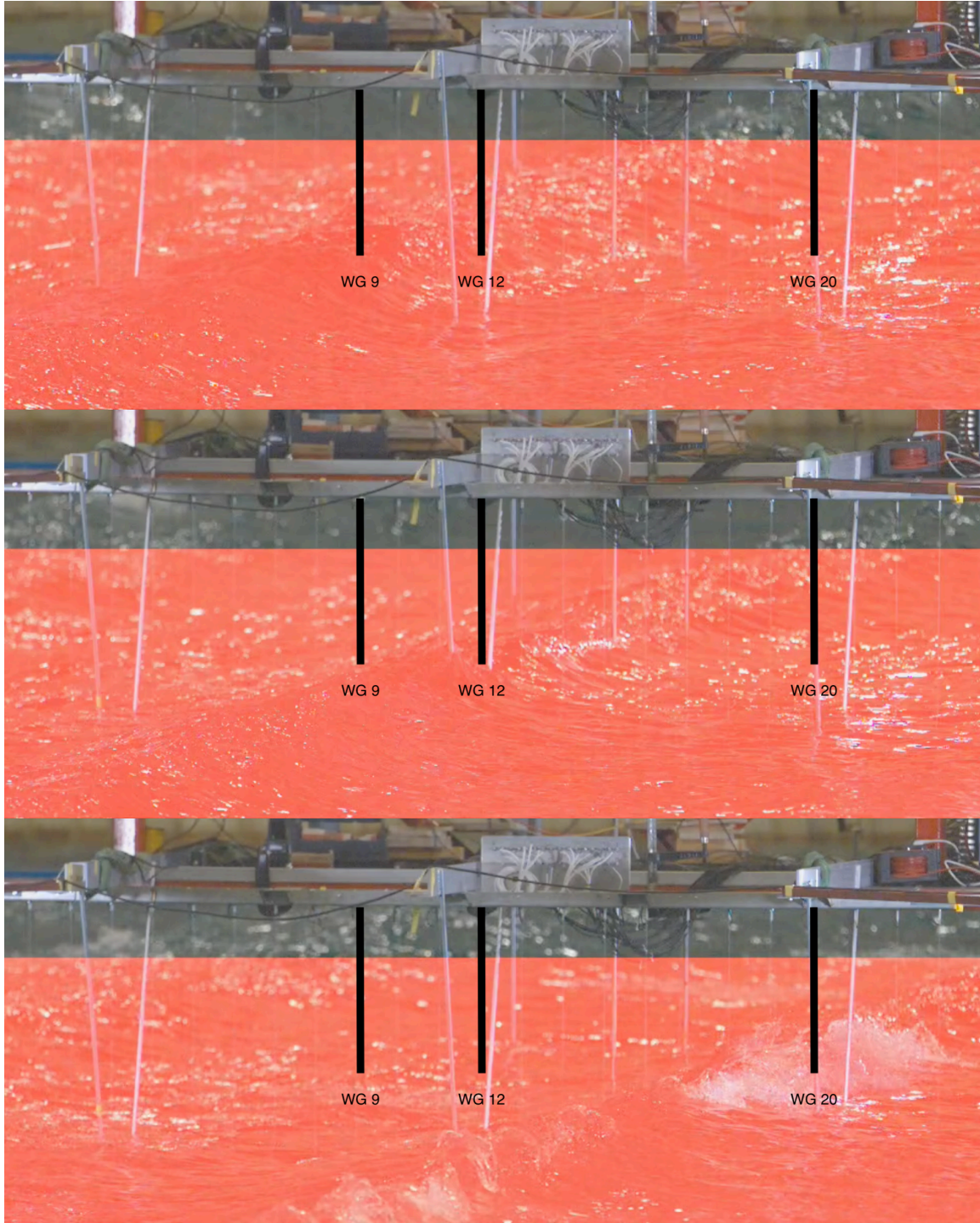


Figure A1: Snapshots from high-speed video clip depicting the breaking process of Event1 in the MARINTEK model test

Event2:

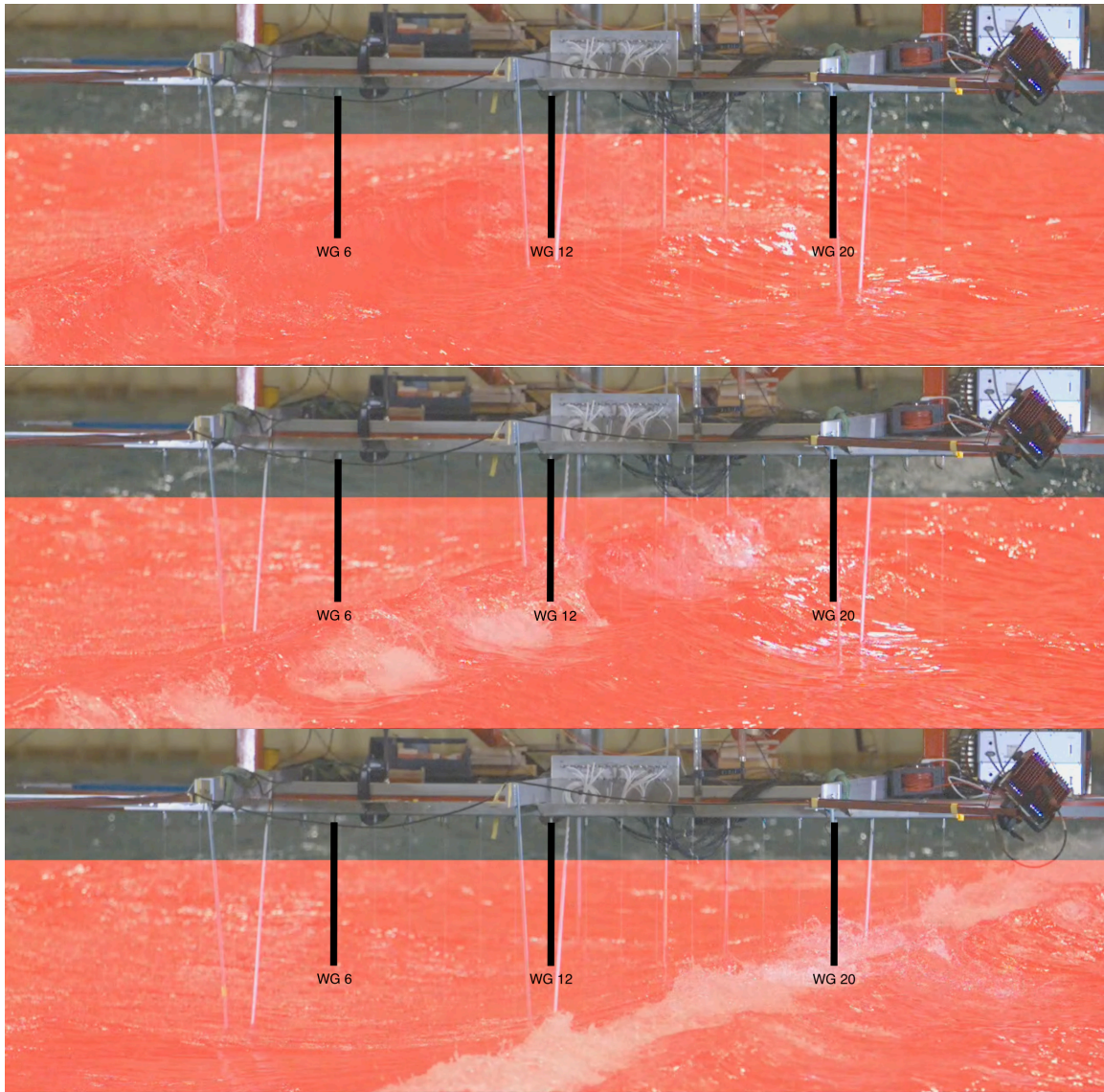


Figure A2: Snapshots from high-speed video clip depicting the breaking process of Event2 in the MARINTEK model test

Event3:

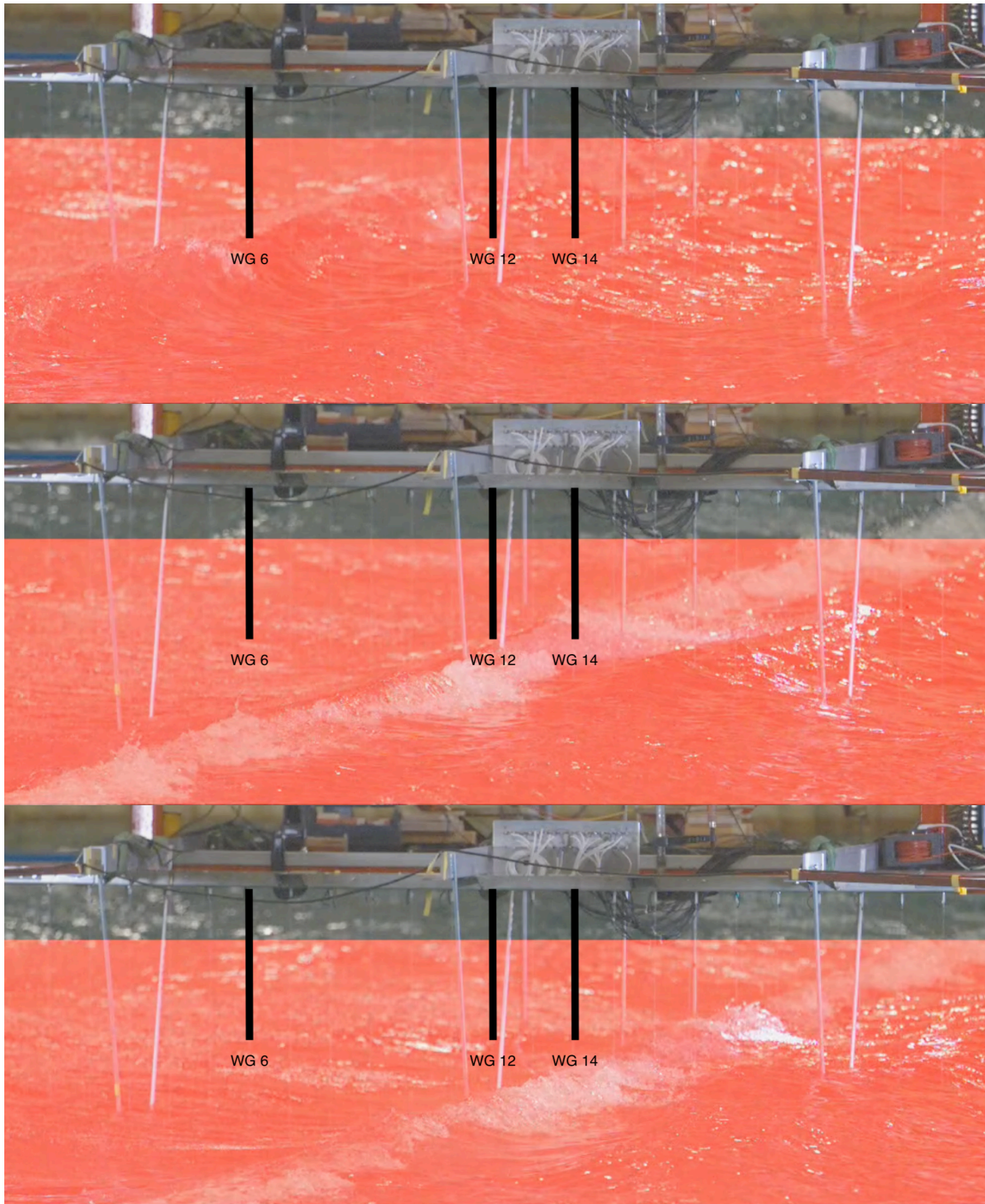


Figure A3: Snapshots from high-speed video clip depicting the breaking process of Event3 in the MARINTEK model test

Event4:

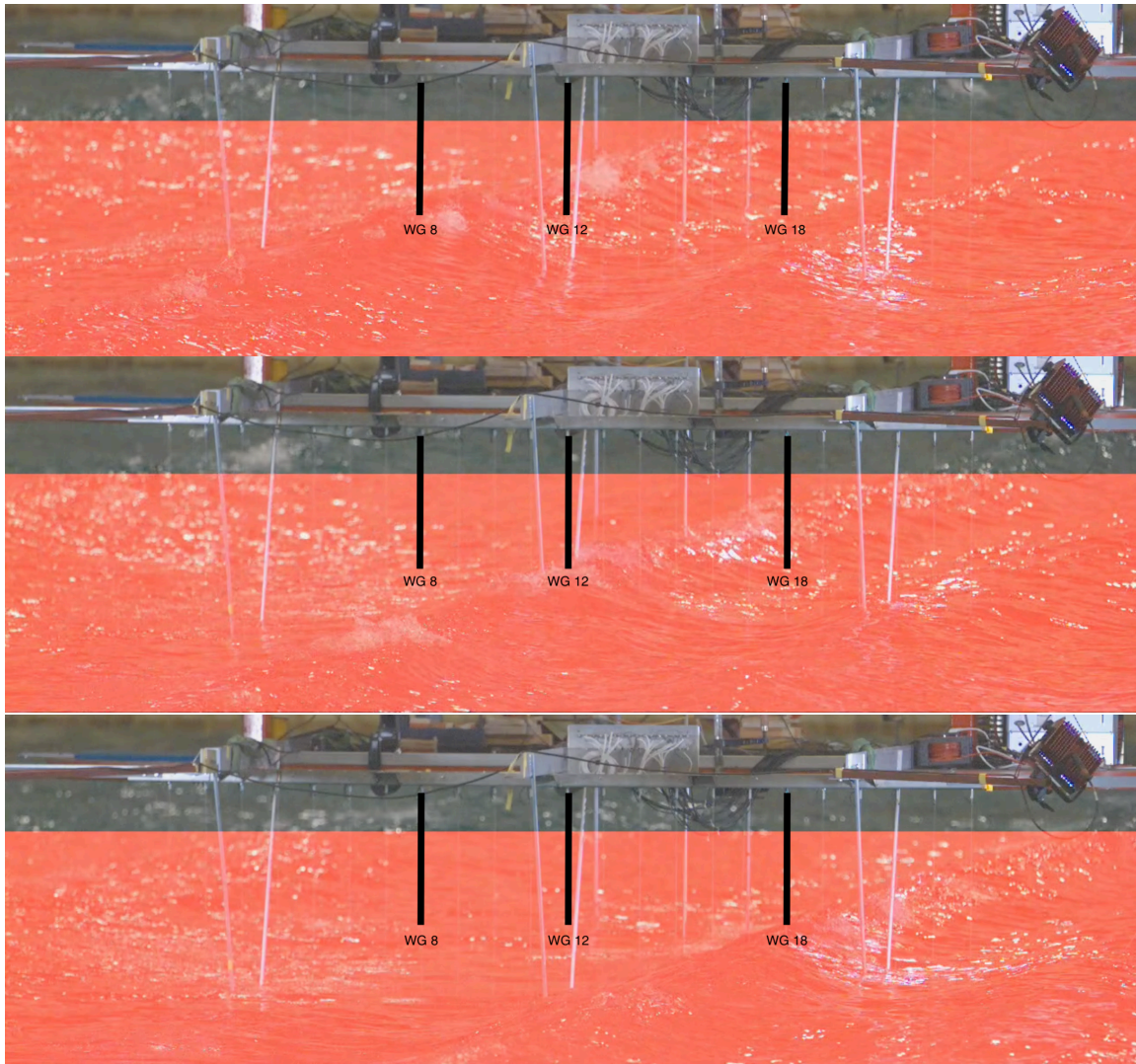


Figure A4: Snapshots from high-speed video clip depicting the breaking process of Event4 in the MARINTEK model test

Event5:

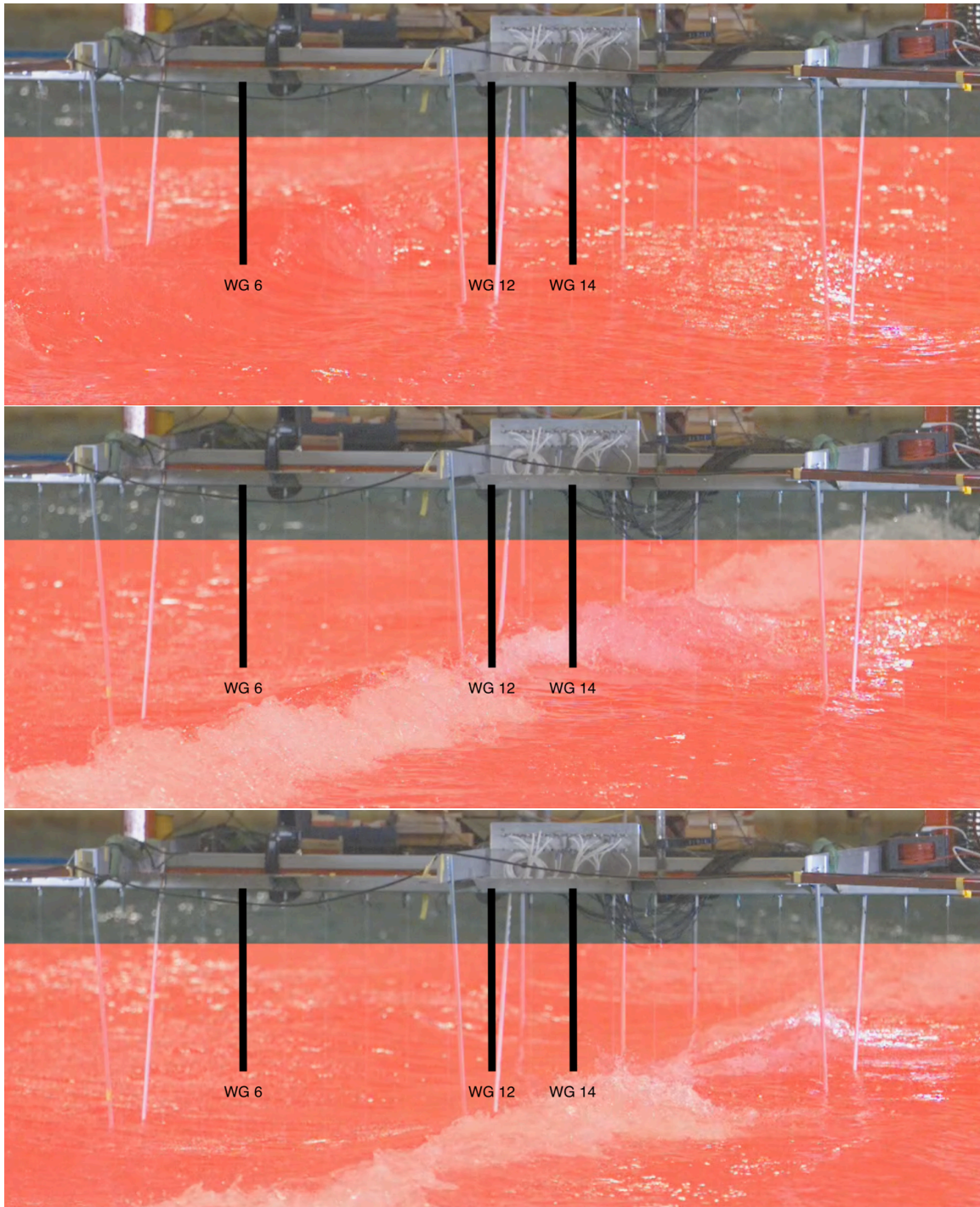


Figure A5: Snapshots from high-speed video clip depicting the breaking process of Event5 in the MARINTEK model test

Event6:

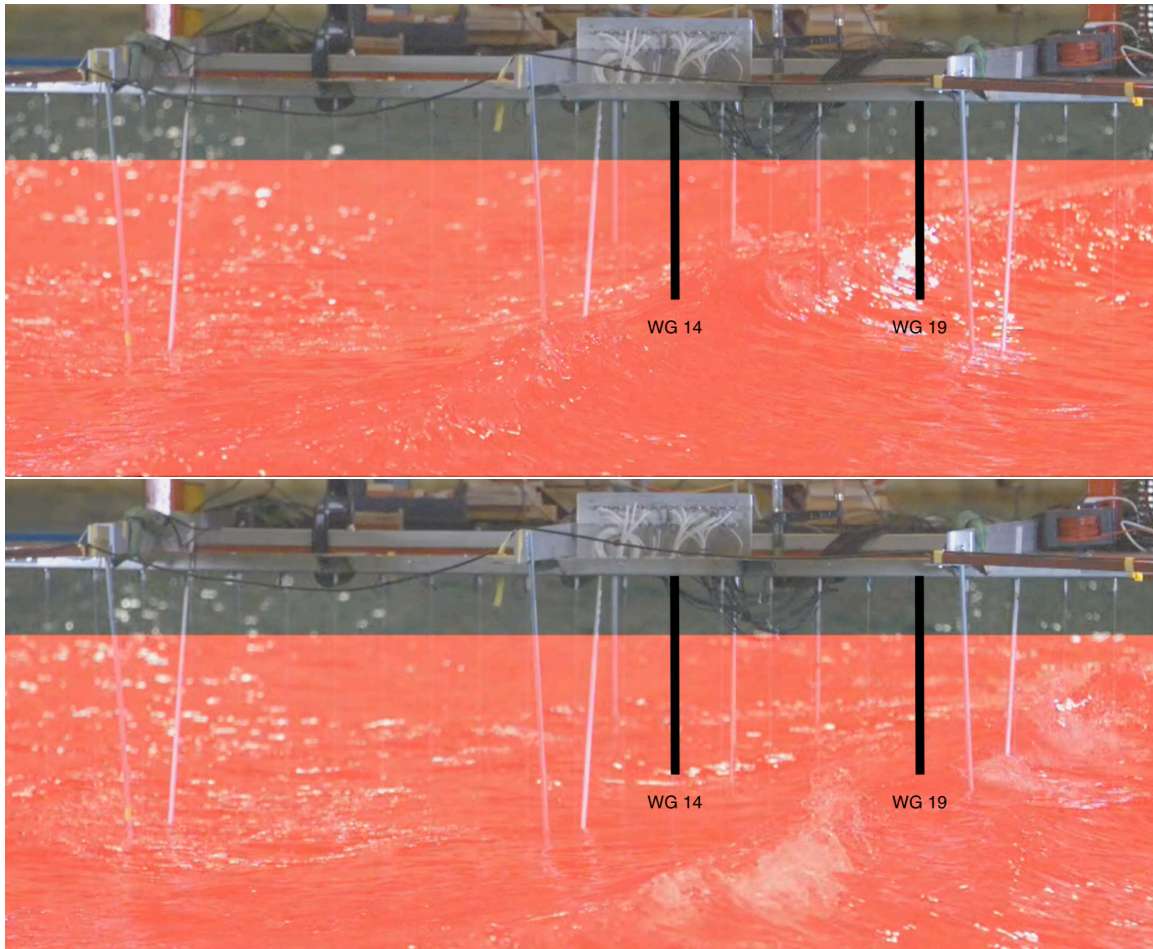


Figure A6: Snapshots from high-speed video clip depicting the breaking process of Event6 in the MARINTEK model test

Event7:

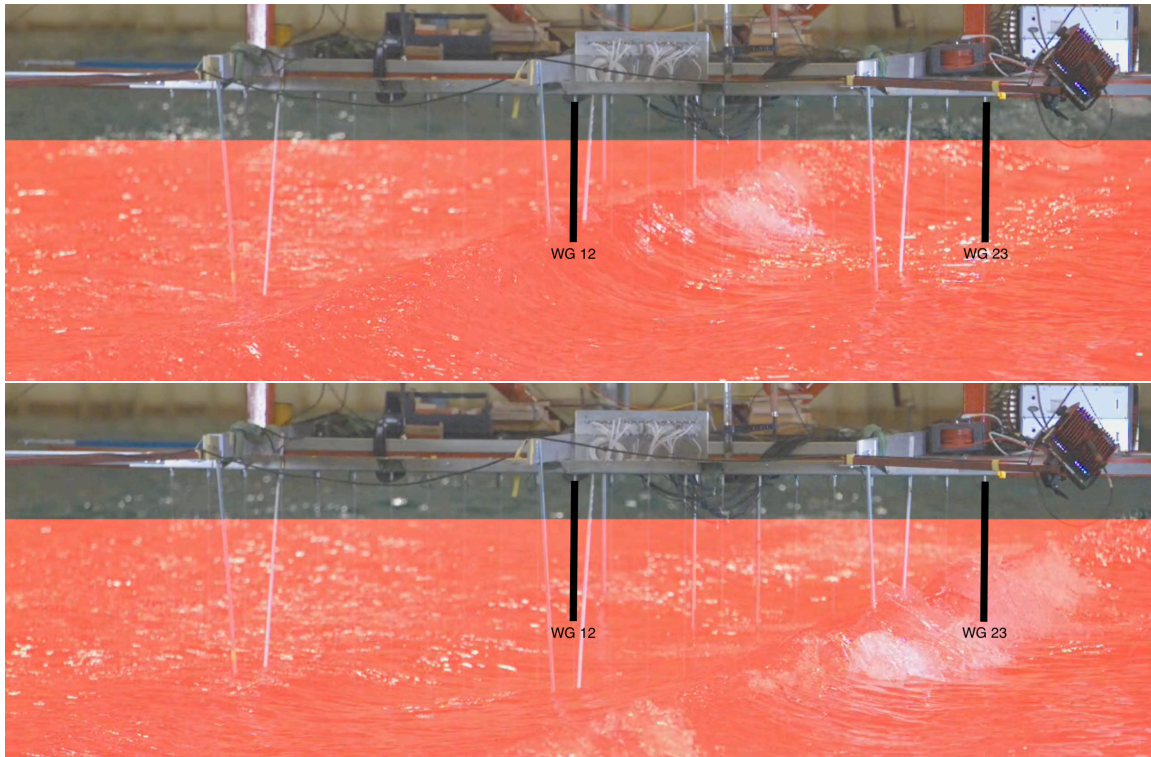


Figure A7: Snapshots from high-speed video clip depicting the breaking process of Event7 in the MARINTEK model test

Event8:

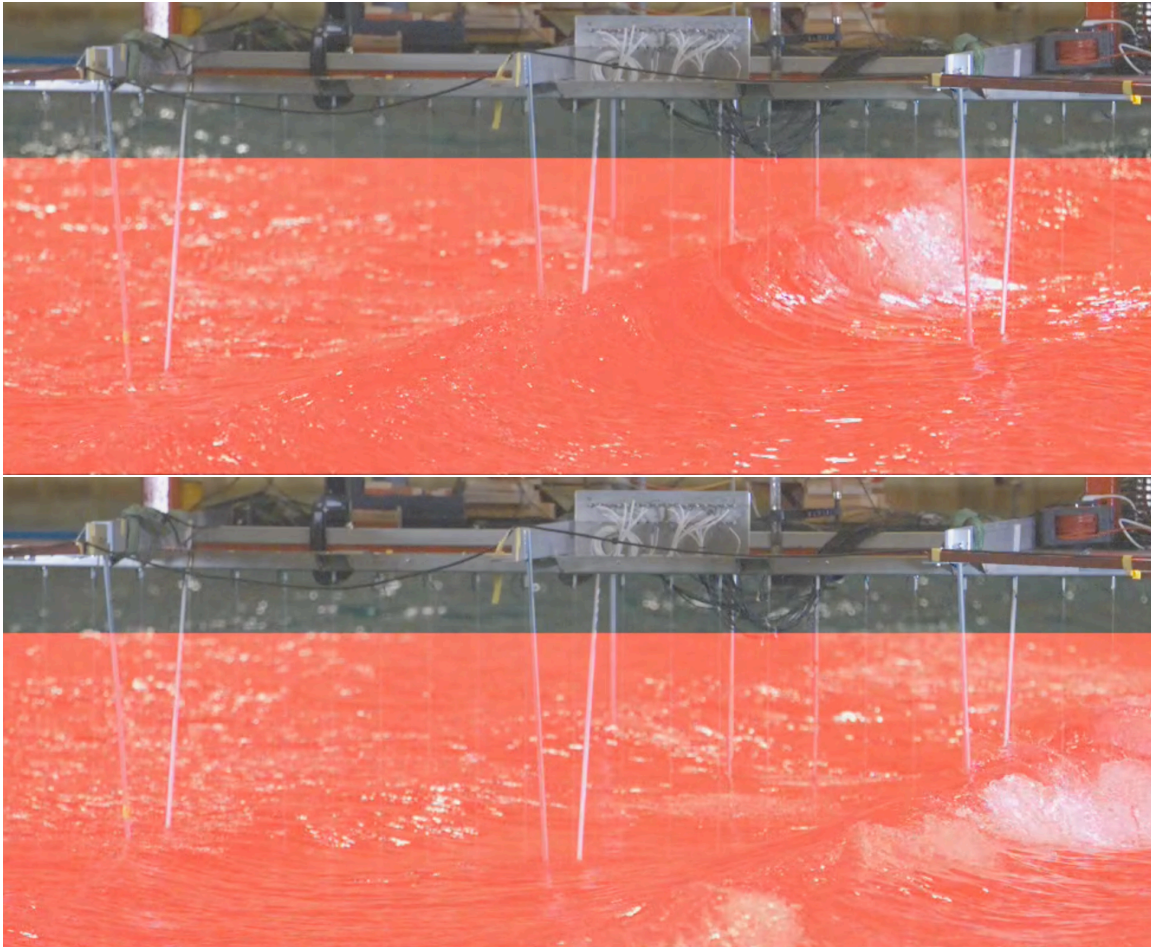


Figure A8: Snapshots from high-speed video clip depicting the breaking process of Event8 in the MARINTEK model test

Appendix B:

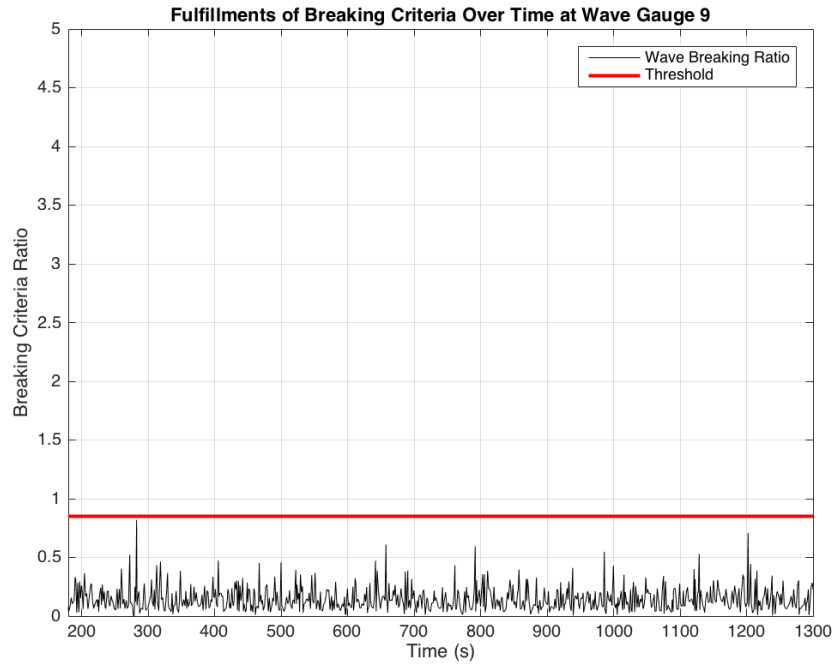


Figure B1: Realizations of the Dynamic/Kinematic Breaking Onset Criterion over the length of the simulation at Wave Gauge 9

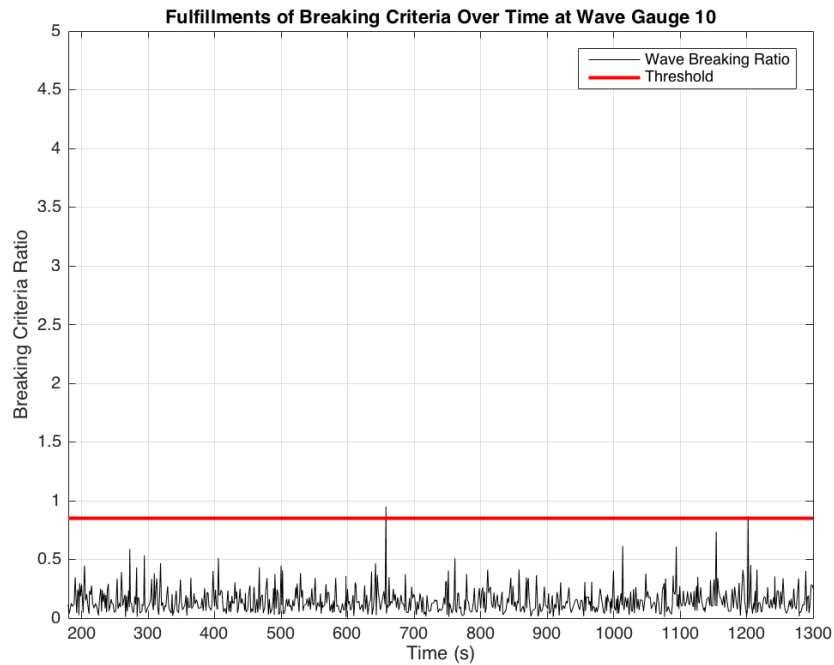


Figure B2: Realizations of the Dynamic/Kinematic Breaking Onset Criterion over the length of the simulation at Wave Gauge 10

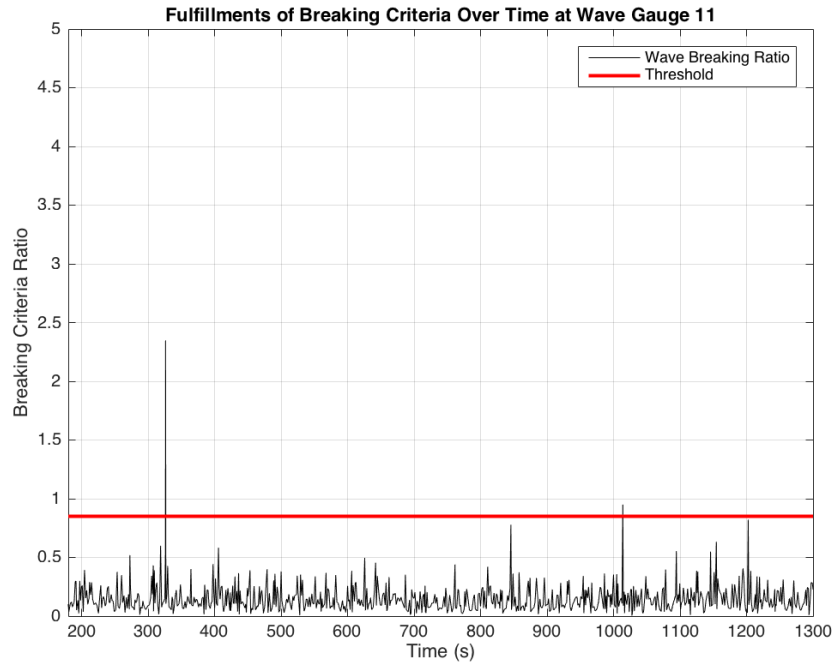


Figure B3: Realizations of the Dynamic/Kinematic Breaking Onset Criterion over the length of the simulation at Wave Gauge 11

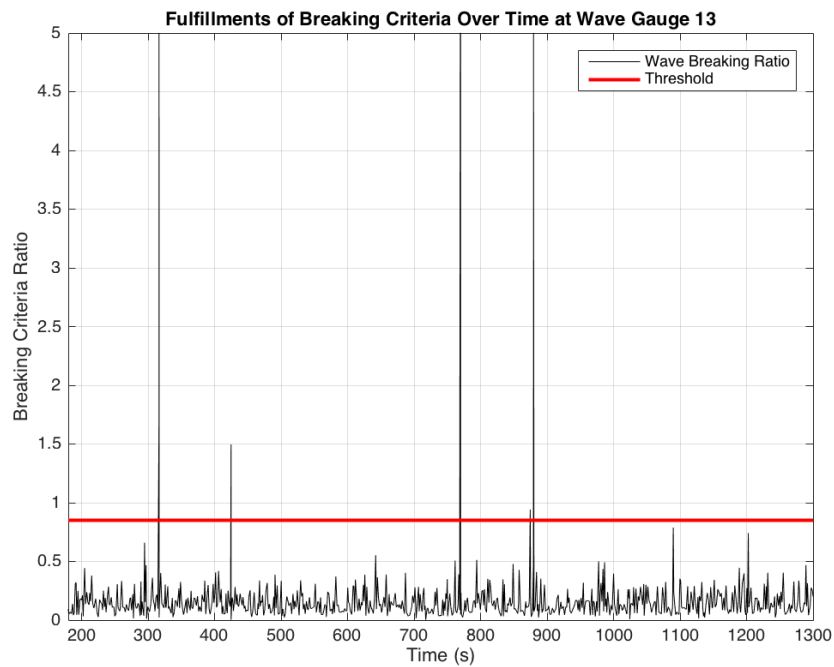


Figure B4: Realizations of the Dynamic/Kinematic Breaking Onset Criterion over the length of the simulation at Wave Gauge 13

Appendix C:

Event1:

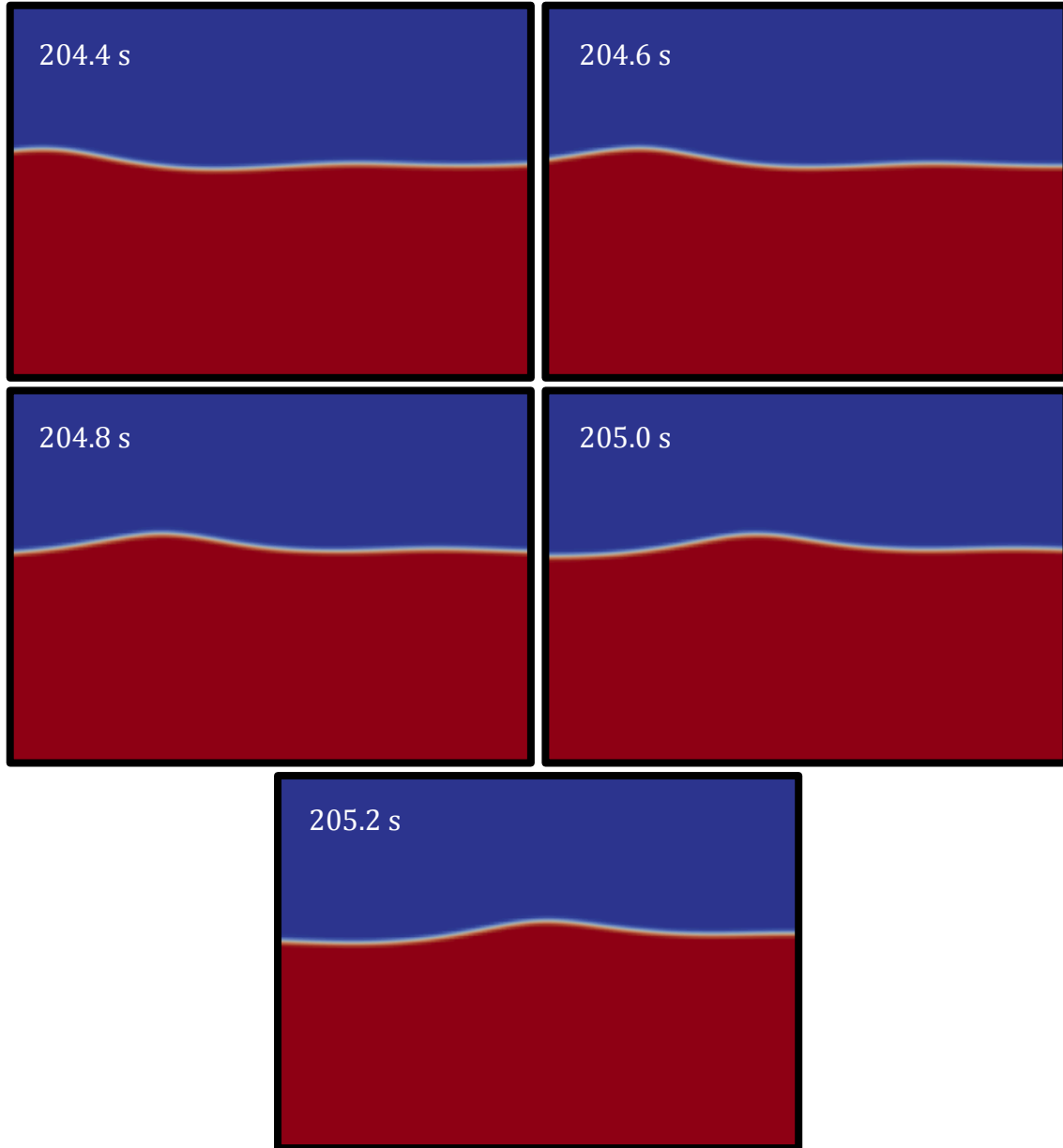


Figure C1: Sub-plots depicting the surface elevations that were modeled in OpenFOAM, for the time stamps indicated in each plot, for Event1

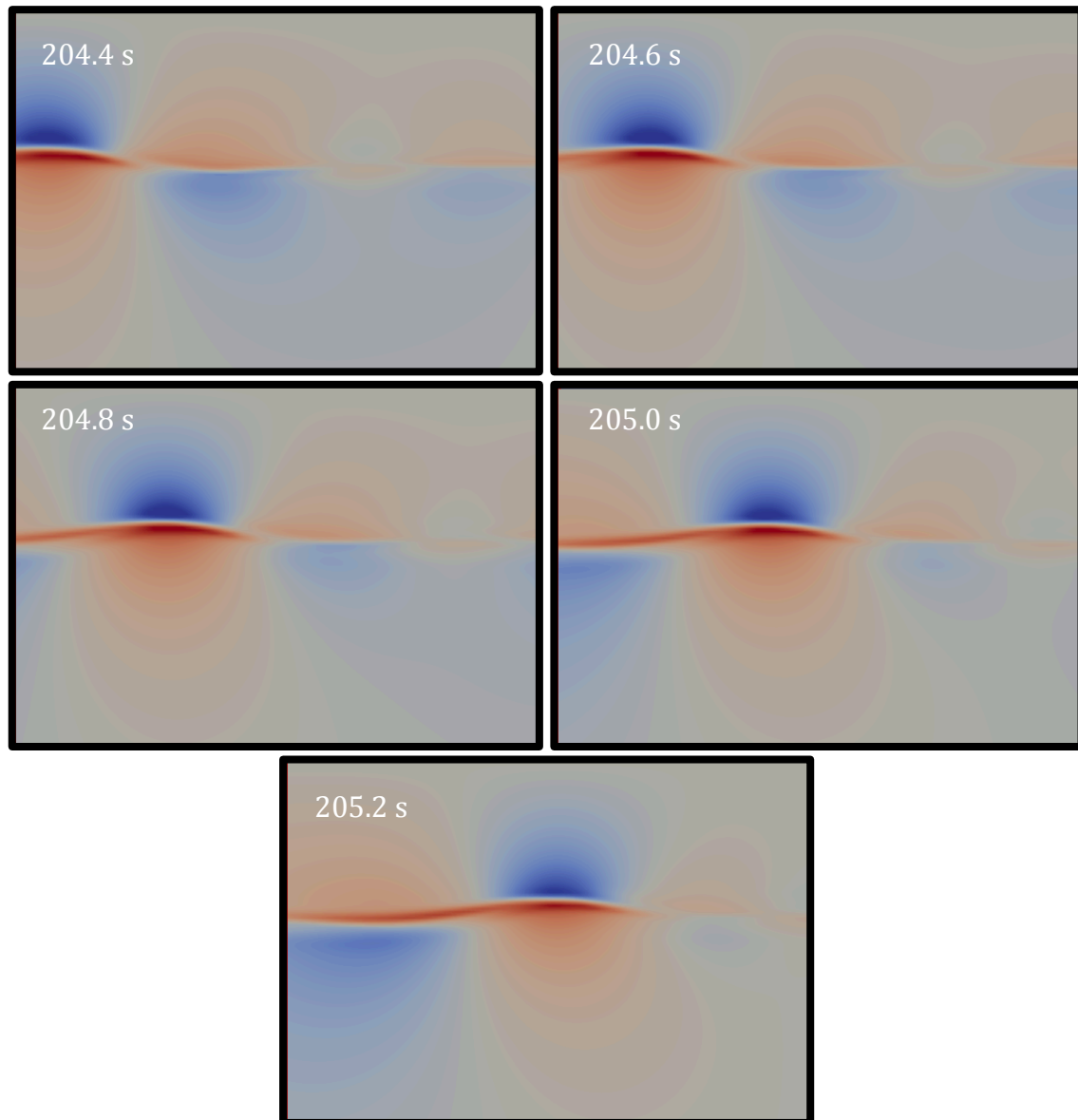


Figure C2: Sub-plots depicting the particle velocities in the direction of wave propagation (U_x) that were modeled in OpenFOAM, for the time stamps indicated in each plot, for Event1; the scale in Figure 31 is applicable to this data

Event2:

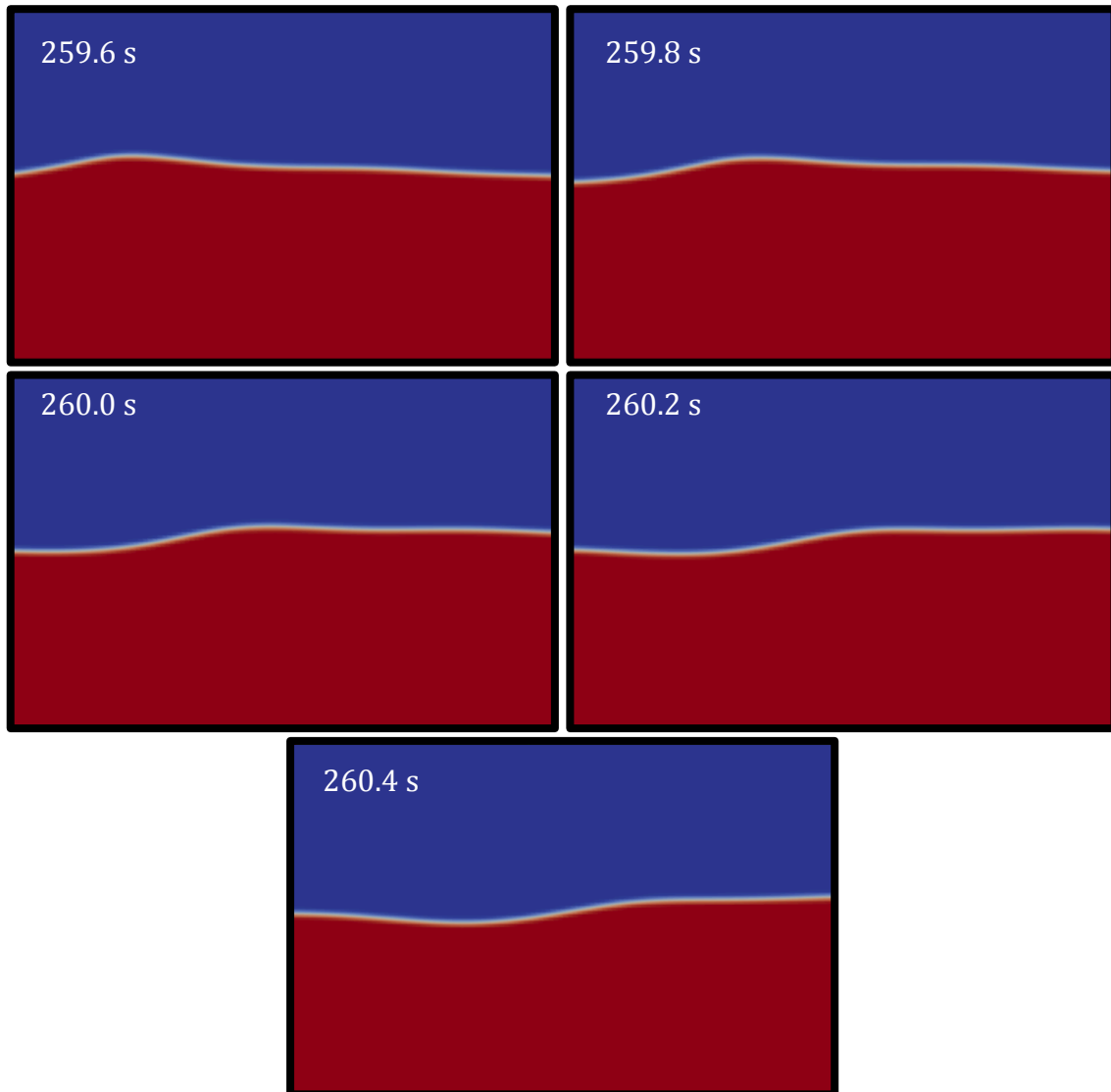


Figure C3: Sub-plots depicting the surface elevations that were modeled in OpenFOAM, for the time stamps indicated in each plot, for Event2

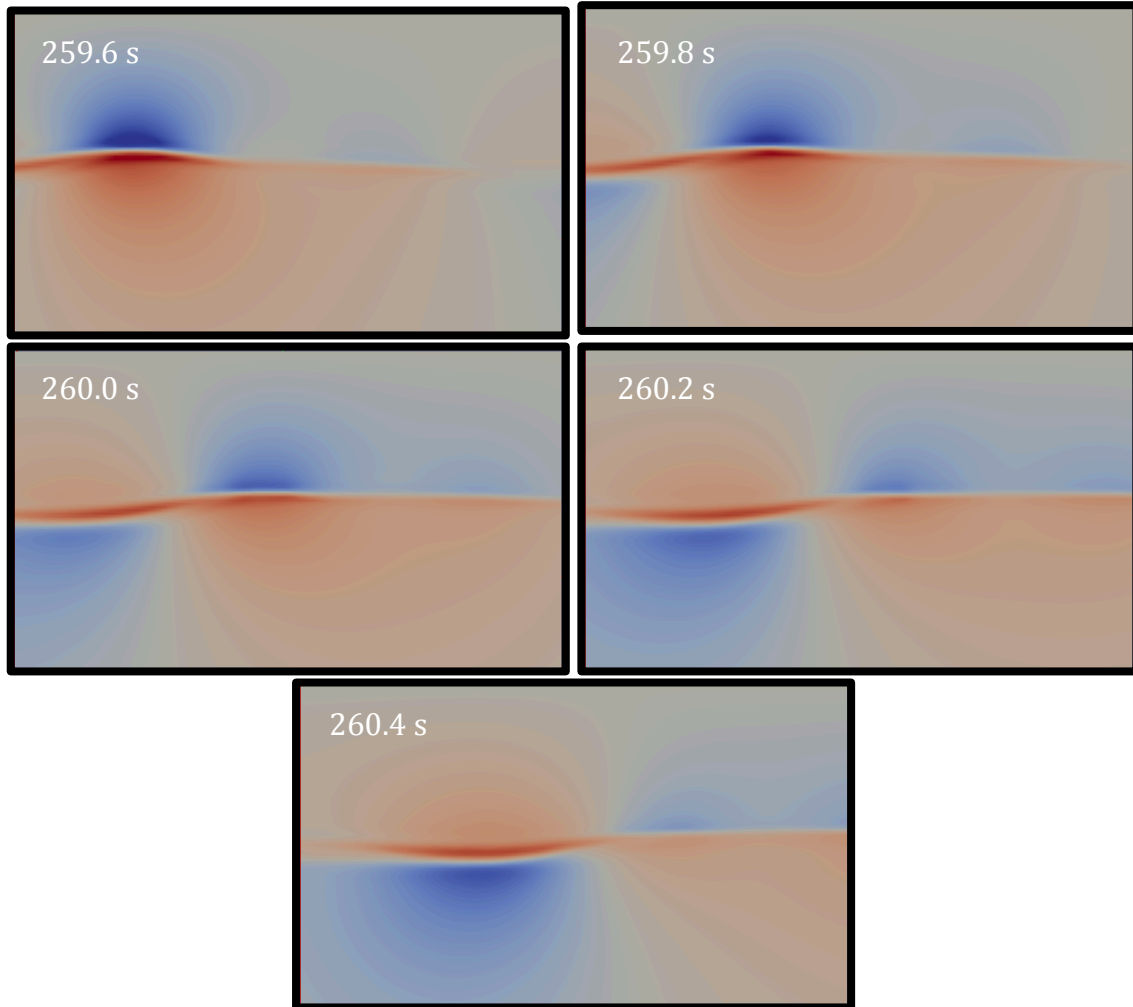


Figure C4: Sub-plots depicting the particle velocities in the direction of wave propagation (U_x) that were modeled in OpenFOAM, for the time stamps indicated in each plot, for Event2; the scale in Figure 31 is applicable to this data

Event3:

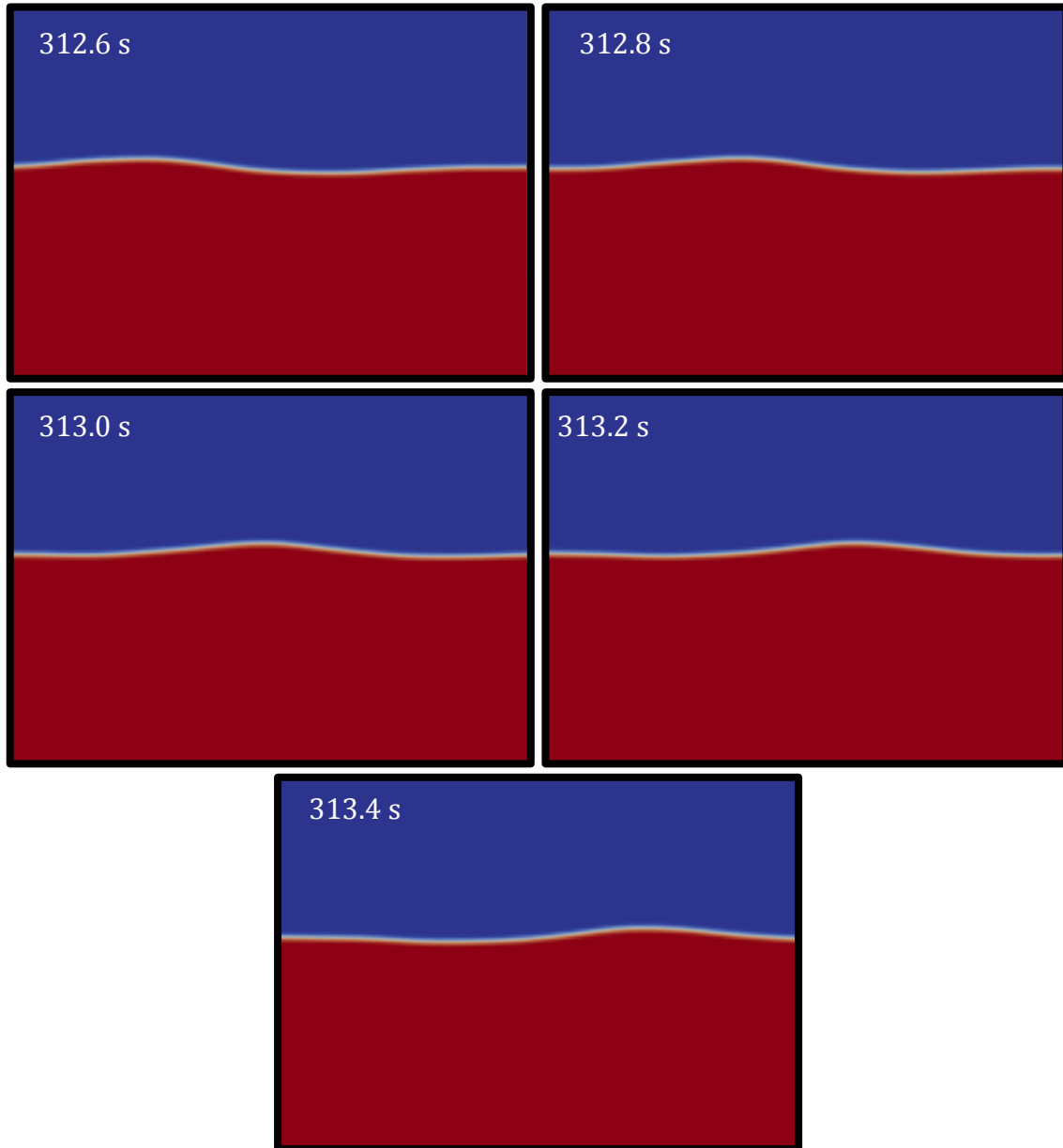


Figure C5: Sub-plots depicting the surface elevations that were modeled in OpenFOAM, for the time stamps indicated in each plot, for Event3

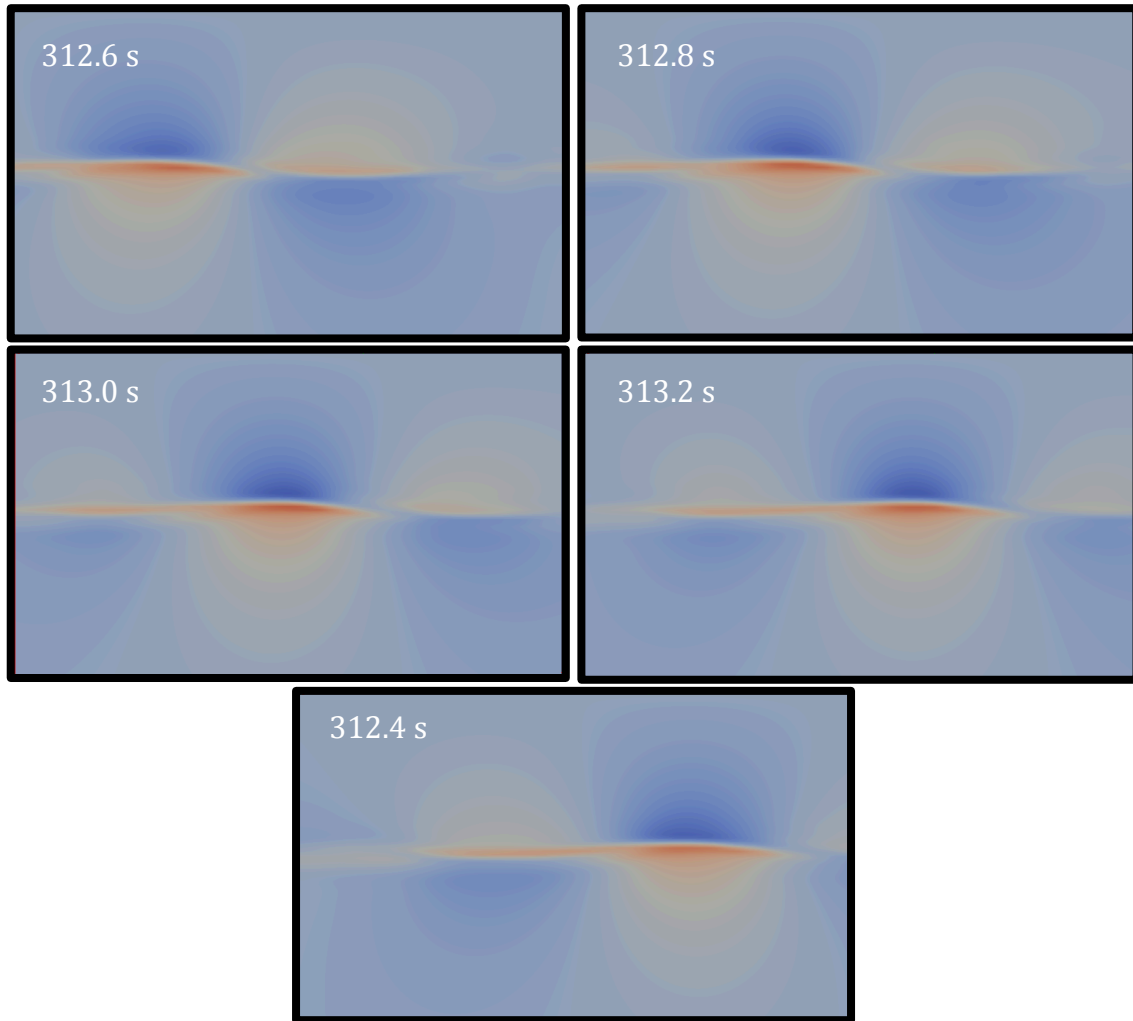


Figure C6: Sub-plots depicting the particle velocities in the direction of wave propagation (U_x) that were modeled in OpenFOAM, for the time stamps indicated in each plot, for Event3; the scale in Figure 31 is applicable to this data

Event4:

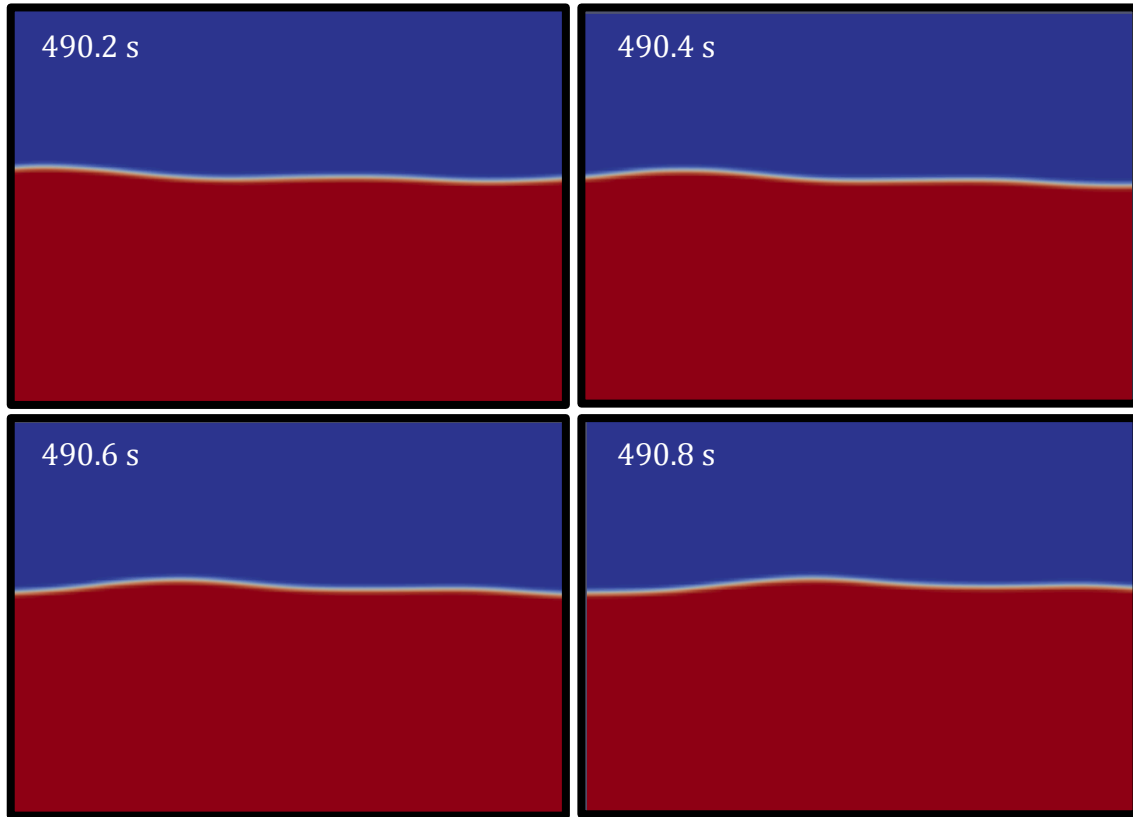


Figure C7: Sub-plots depicting the surface elevations that were modeled in OpenFOAM, for the time stamps indicated in each plot, for Event4

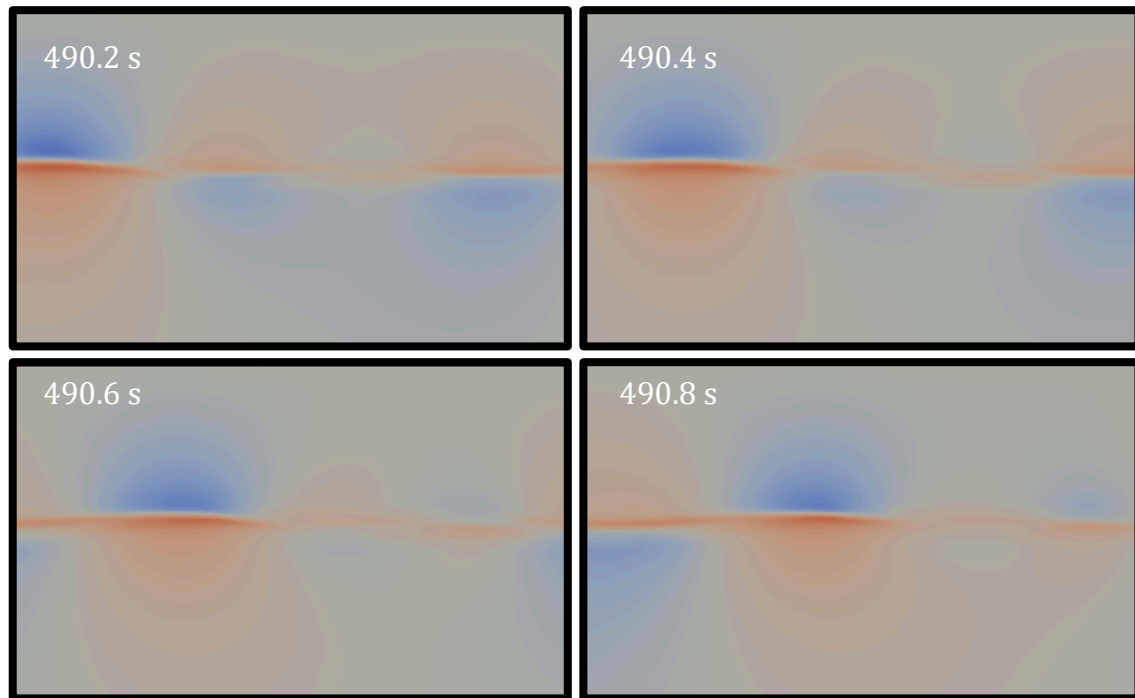


Figure C8: Sub-plots depicting the particle velocities in the direction of wave propagation (U_x) that were modeled in OpenFOAM, for the time stamps indicated in each plot, for Event4; the scale in Figure 31 is applicable to this data

Event5:

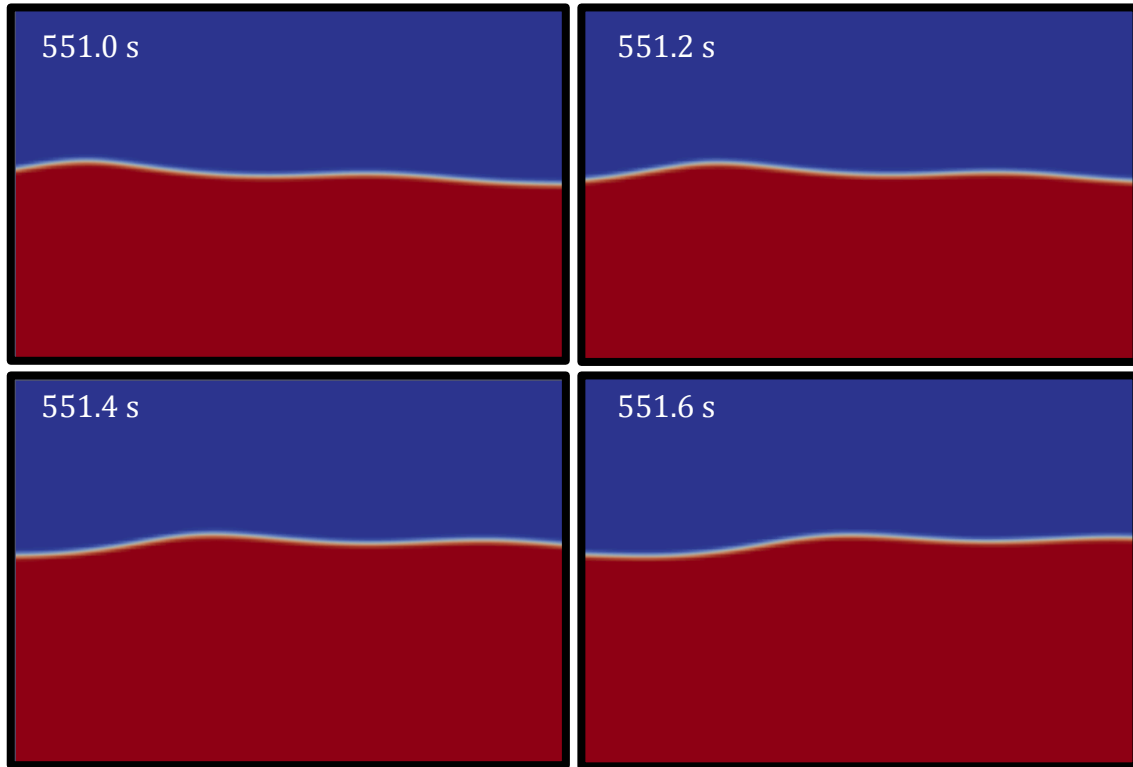


Figure C9: Sub-plots depicting the surface elevations that were modeled in OpenFOAM, for the time stamps indicated in each plot, for Event5

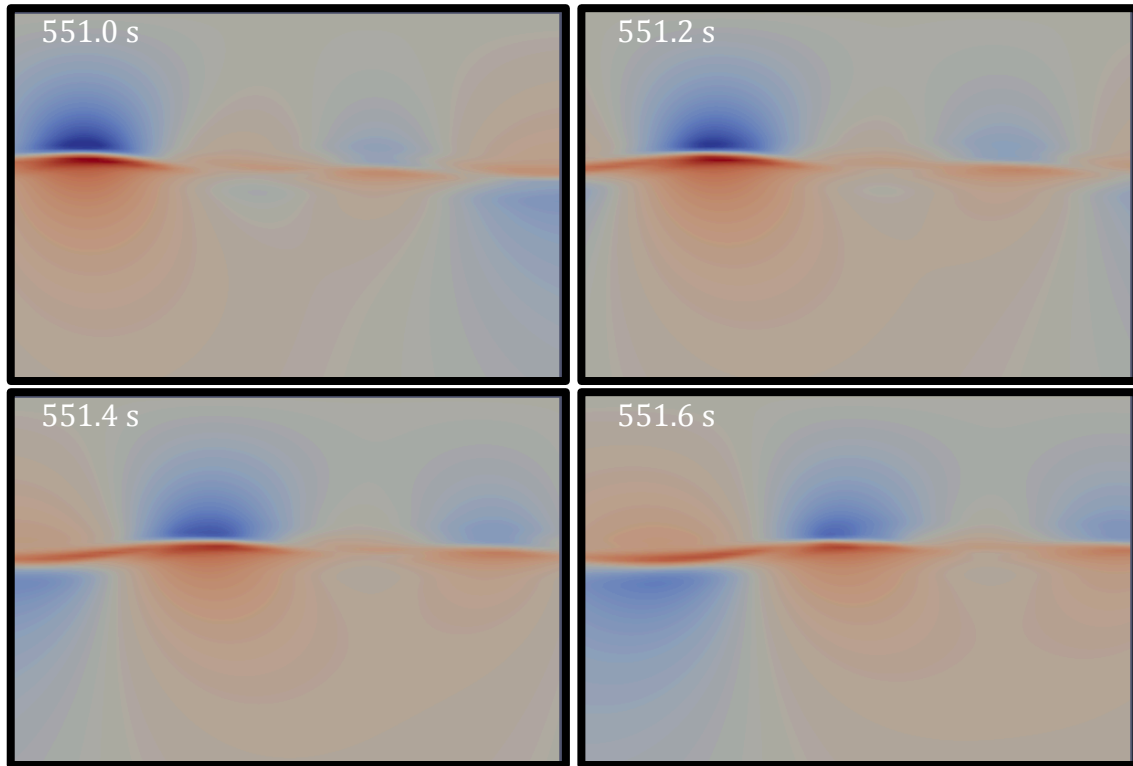


Figure C10: Sub-plots depicting the particle velocities in the direction of wave propagation (U_x) that were modeled in OpenFOAM, for the time stamps indicated in each plot, for Event5; the scale in Figure 31 is applicable to this data